Kenneth Duffaut

Stress sensitivity of elastic wave velocities in granular media

Thesis for the degree of Philosophiae Doctor

Trondheim, January 2011

Norwegian University of Science and Technology
Faculty of Engineering Science and Technology
Department of Petroleum Engineering
and Applied Geophysics

NTNU – Trondheim
Norwegian University of
Science and Technology

Summary

Knowledge of the stress sensitivity of elastic-wave velocities in sedimentary rocks with different consolidation is important for several geophysical applications such as seismic pore pressure prediction, time-lapse seismic analysis and not least in seismic exploration. Since clays or shales are more compactable than sand or sandstones they often experience large plastic deformation causing both clay platelet orientation and porosity reduction of the order of 50% or more. The interplay between stress and porosity effects may mask the stress sensitivity of velocities in clays or shales. The porosity loss occurring in sandstones during mechanical compaction is generally slower and hence the stress-induced velocity changes are better preserved at least prior to the onset of grain cementation. Small amounts of contact cement, 1 to 2% of the total rock volume, can have a dramatic effect on velocities and their corresponding stress dependence. We demonstrate this reduction in stress sensitivity of elastic-wave velocity between sandstones of different consolidation through comparison of rock physics contact model-predictions of compressional to shear velocity ratio (V_p/V_s), with similar estimates obtained from time-lapse seismic amplitude versus offset (AVO) data from two oil producing fields.

Furthermore, modified contact models are proposed to investigate the role of the combined effects of intergrain contact friction, increasing differential stress and stress ratio in relation to the propagation direction of the elastic-waves in granular media. Model-predictions are compared with ultrasonic measurements obtained from experimental compression tests on unconsolidated sands.

Preface

This thesis is submitted in the partial fulfillment for the requirements of the degree Philosophiae Doctor (PhD) at the Norwegian University of Science and Technology. The PhD thesis is carried out at the Department of Petroleum Engineering and Applied Geophysics and at the Statoil Research Center in Trondheim.

I am grateful to my advisor Professor Martin Landrø for sharing his knowledge and experience, and for the many enlightening discussions. I would also like to thank my co-advisor Professor Roger Sollie for supporting my PhD proposal with guidance during my work. I am very impressed of both their abilities to get inside problems and propose solutions.

I thank my employer Statoil for giving me this great learning opportunity in addition to the financial support. In that regard, a special thank to John Reidar Granli, Kari Nesbø, Odd Arve Solheim, Ole Jacob Martinsen, Tage Røsten and Lill-Tove Wetjen Sigernes. I would also like to thank many other colleagues in Statoil for several interesting discussion and caring. A special thank to Eiliv Skomedal, Ivar Brevik, Anne-Kari Furre, Janniche Iren Nordskag, Ole Kristian Søreide, Ørjan Pedersen, Andrew James Carter, Tor Erik Rabben, Lasse Renli, Bård Bostrøm, Helge Løseth, Lars Ole Løseth, Lasse Amundsen, Lars Wensaas, Marita Gading and Lisbeth Stjern for sharing their knowledge with me, fruitful discussions and support with programming, LATEX and supply of articles for my work.

Professor Rune Martin Holt is thanked for giving good and challenging rock physics courses and discussions, and Per Avseth from Odin Petroleum and Torgeir Wiik from the Norwegian University of Science and Technology for fruitful discussions and collaboration. I would also like to thank my former colleague Arne Johannes Kaaijk Jenssen for interesting discussions and Christian Madshus at NGI Oslo for sharing all his knowledge about vibrations in soils on near-surface constructions. Knut Bjørlykke and his group for enlightening and interesting discussions about sediment deposition and compaction. The staff, current and former PhD students at the Department of Petroleum

Engineering and Applied Geophysics for a good facilitation and working environment and not least issuing of all the temporarily parking tickets every week in almost 5 years.

I would like to honor my parents and siblings for all the love and care through my life and encouraging me to start university education. Last but not least, I am grateful for all the love and patience from my fiancée Marit Selboe Bjørlykke and our children: Mathias, Benjamin and Christoffer throughout my work.

Trondheim, January 2011

Kenneth Duffaut

"To move the world we must first move ourselves." Socrates

Contents

Chapter 1

Thesis introduction

This thesis is a contribution towards a better understanding of the role of stress on elastic-wave velocities in granular media such as sand and sandstone. Since these constitute the more abundant types of coarse-grained sediments, much effort has been invested into experimental work towards better understanding the stress sensitivity of their elastic-wave velocities. This is partly driven by the increased use of time-lapse (4D) seismic data for subsurface characterization to improve hydrocarbon recovery rates, but also by seismic exploration through more quantitative interpretation techniques which use seismic velocities and amplitudes for pore pressure prediction, lithology and hydrocarbon identification.

In this chapter, I will briefly explain the role of stress on elastic-wave velocities in a broader sense as burial turns sediments into rocks. At the end a brief summary of the individual papers of this thesis is given.

1.1   Controls on elastic-wave velocities in sediments and rocks

The sedimentation processes lead to deposition of various kinds of unconsolidated sediments in basins. These newly deposited unconsolidated sediments are characterized by loosely packed, uncemented fabrics with high porosity and high water content. As sedimentation continues in subsiding basins, older sediments are progressively buried by younger sediments to increasingly greater depths (z). Burial is accompanied by an interplay of physical and chemical changes that take place in the sediments in response to increasing overburden stress and temperature that causes sediment to compact, converting loose soil-like material slowly into consolidated rocks. Thus unconsolidated sand is lithified into sandstone while siliciclastic clay is hardened into shale. Consequently, the porosity and permeability of the various sediments decrease with depth causing the bulk density and elastic wave velocities to increase with consolidation. The response of the sediment compaction is often seen in many velocity and density logs as an increase in the their low-frequency components with depth, see Figure 1.1. From a seismic processing point of view, it is this low frequency component that normally is estimated though velocity analysis.
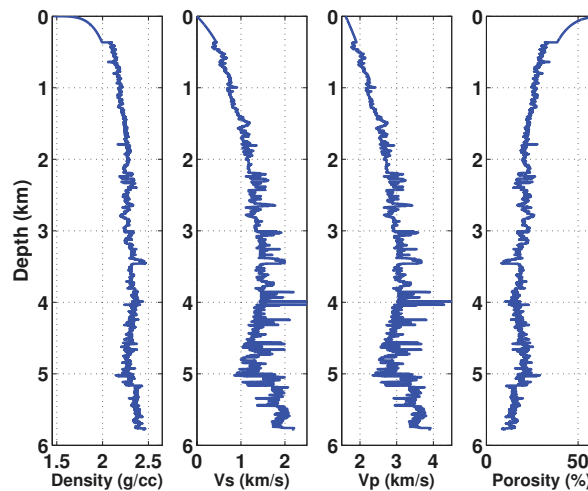

Figure 1.1: Example log suite. Left: Density, S-wave velocity, P-wave velocity and Porosity. Zero depth represents the seadbed.

Often, clays or shales are more compactable than sand or sandstones (Rieke

and Chilingar, 1974; Wolf and Chilingarian, 1975; Allen and Allen, 1990). Contrast in framework explains the difference in porosity loss. Newly deposited clay consists of an open framework of clay platelets of different mineralogy (Hornby, 1994; Sayers, 1999; Wang et al., 2001) which usually collapses and deforms gradually as burial proceeds. For sands, the framework consists of dense, semi-spherical rigid grains, packed together and dominated by durable quartz (Boggs, 1995) that resists mechanical compaction better that clay and shale. Numerous mechanical compaction experiments performed on sands and clays (Rieke and Chilingar, 1974; Magara, 1980; Zimmerman, 1991; Chuhan et al., 2002; Mondol et al., 2007; Zimmer et al., 2007) confirm such difference in porosity loss. This large-scale lithology and porosity variation may cause the low frequency component of some velocity and density logs to exhibit a blocky character (Storvoll et al., 2005).

The changes in petrophysical (porosity, mineralogy, cement) and elastic properties (e.g. velocities) of sediments are complex functions of both mechanical and chemical compaction processes that predominate at different depths as a result of changes in overburden stress, pore pressure and temperature (Athy, 1930; Hedberg, 1936; Johnston, 1987; Graham et al., 2004; Mondol et al., 2007). Mechanical compaction is a function of both rock frame compressibility and differential stresses (overburden stress minus pore pressure) and dominates in the shallow parts of the basin at depths down to about 2-5 km depth depending on the geothermal gradient of approximately 15-30°C/km. Chemical compaction on the other hand involves interactions between porous solids and interstitial fluids, i.e. precipitation of minerals (cementation), that usually dominates in the deeper parts of the basin beyond >75°C where time, temperature and mineralogy are the main controlling compaction components (Bjørlykke et al., 1989; Horbury and Robinson, 1993; Bjørlykke, 1999; Lander and Walderhaug, 1999; Avseth et al., 2008). In case of mechanical compaction where we consider hydrostatic or overburden principal stress conditions ($\sigma_1=\sigma_2=\sigma_3$), water within the pore spaces of the rocks is connected to the sea above. The lithostatic stress ($\sigma_3=\sigma_z$) is due to the weight of the fluid saturated rock (ρ_b) and is given by

$$\sigma_3\left(z\right) = \int_0^h g\left(z\right)\rho_b\left(z\right)dz, \tag{1.1}$$

where $g(z)$ is the acceleration due to gravity, and h is the total depth. Similarly, the pore pressure P_{pore} is the weight of the water column, and is give by

$$P_{\mathrm{pore}}\left(z\right) = \int_0^h g\left(z\right)\rho_f\left(z\right)dz, \tag{1.2}$$

where $\rho_f(z)$ is the pore fluid density as a function of depth. In Figure 1.2 a

schematic lithostatic and pore pressure depth trend is shown. According to Terzaghi's principle (Terzaghi, 1943) the differential stress (σ_3') acting on the rock frame is given as

$$\sigma_3' = \sigma_3 - P_{\text{pore.}} \tag{1.3}$$

Since the bulk density of fluid filled rocks is always greater than the pore fluid density, the differential stress will increase with depth. Velocities in sed-
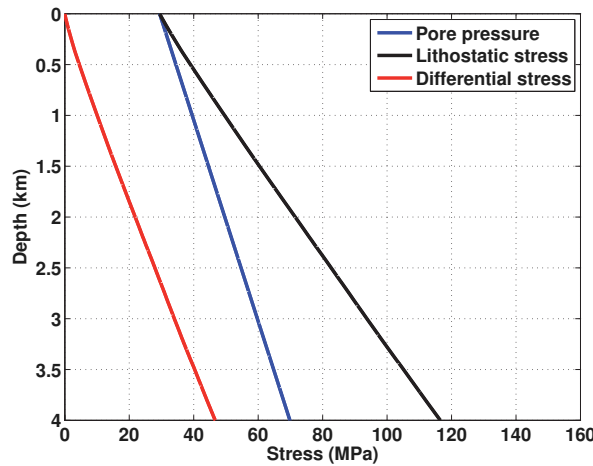
Figure 1.2: Schematic stress and pore pressure depth trends. Zero depth in this figure represents the seadbed where the differential stress equals zero (lithostatic stress = water pressure).

imentary rocks also depend upon the in-situ differential stress (Wyllie et al., 1958; Gueguen and Bouteca, 1999) and hence the increasing differential stress is therefore accompanied by an increasing P-wave and S-wave velocity (Figure 1.1).

1.2 Stress-dependent elastic-wave velocities in granular media

The loss in porosity (ϕ) occurring during burial has a primary effect on the elastic wave velocities of sand when it converts into sandstone. However, the interplay between porosity loss, increasing differential stress and lithification causes velocities in sand and sandstone to increase. Experimentally, it can be difficult to separate out the individual effects but contact theory captures the stress sensitivity of velocities in unconsolidated sands and sandstones since

it assumes constant porosity with increasing differential stress. Figure 1.3 compares P-wave, S-wave velocity and velocity ratio (V_p/V_s) as a function of differential stress obtained from water saturated unconsolidated sand samples (circle symbols), with Walton's contact model (black solid line) assuming near zero contact friction (slip limit) between spherical grains and pores filled with water using Gassmann's relation (Gassmann, 1951). In general, elastic wave
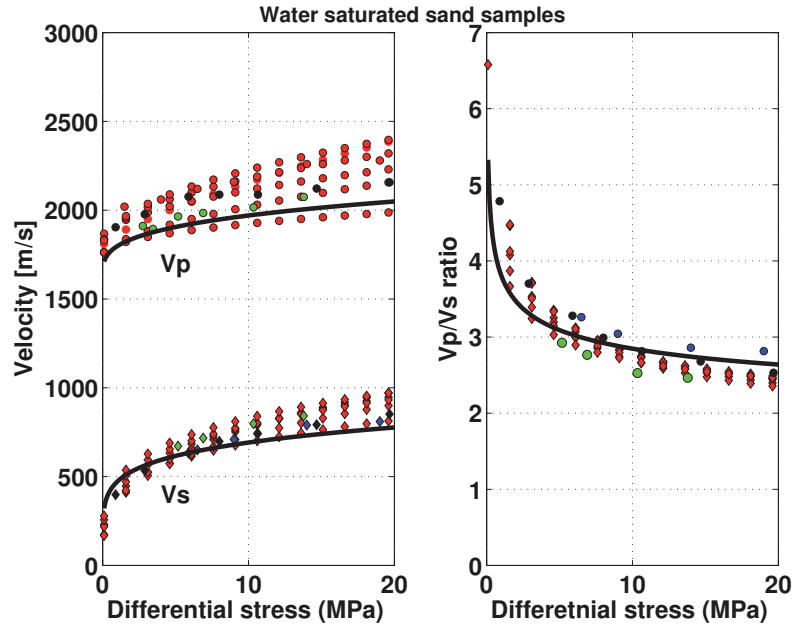
Figure 1.3: P-wave, S-wave velocity and V_p/V_s as a function of isotropic differential stress obtained from ultrasonic measurements on water saturated unconsolidated sands samples. The black solid lines represents model-predictions of water saturated P-wave and S-wave velocities of a spherical grain pack of 36% porosity obtained from combining Walton's slip limit (Walton, 1987) with Gassmann's equation (Gassmann, 1951). The modeling assumes solid quartz grains using moduli and density from Mavko et al. (1998) together with a fluid modulus of 2.20 GPa and density of 1.03 g/cm^3. Data courtesy Domenico (1977); Yin (1992); Prasad (2002); Zimmer (2003).

velocities (V) of granular rocks will increase with increasing differential stress (σ') as seen from Figure 1.3. This is intuitive since compression stiffens and broadens the contacts between the grains. The largest velocity change, in e.g. water saturated unconsolidated sandstones, is observed at low differential stresses where S-wave velocity show stronger stress sensitivity than P-wave

velocity (Figure 1.3).

According to Holt et al. (2005), the stress sensitivity of velocities ($\Delta V/\Delta\sigma'$) can be expressed as

$$\frac{\Delta V}{\Delta\sigma'} = \frac{\Delta V}{\Delta\phi}\frac{\Delta\phi}{\Delta\sigma'}, \tag{1.4}$$

when assuming that porosity is the only parameter controlling wave velocity changes with stress. Experimentally, a constant volume (or constant porosity) compression test can be design to capture the pure stress sensitivity of velocities $(\Delta V/\Delta\sigma')_{\phi=constant}$ for a specific granular material similar to that shown in Figure 1.3. A more comprehensive overview of modeling approaches as function of stress, porosity and cracks are found in Wang and Nur (1992); Mavko et al. (1998); Avseth et al. (2005); Fjær et al. (2008).

Laboratory experiments on granular rocks undergoing monotonic isotropic loading, an increase in velocities as shown above occurs with increasing differential stress in all directions (Holt et al., 2005). However, in case of a uniaxial compression (zero lateral strain) the rates of velocity increase are larger when the wave propagation direction coincides with the largest stress direction (Nur and Simmons, 1969; Yin, 1992; Ruiz, 2003; Sayers, 2005b; Chen et al., 2006; Sherlock et al., 2007). Figure 1.4 shows the change in the Thomsen anisotropy parameters (Thomsen, 1986) derived from multi-directional velocity measurements of Yin (1992) on sandstone as the horizontal-to-vertical stress ratio ($K_0 = \sigma_1/\sigma_3$) decreases. The largest negative anisotropy value is observed for the Thomsen P-wave anisotropy parameter ϵ. This particular observation may be explained by the fact that P-wave velocity depend mainly on the stress component in the direction of wave propagation. S-wave velocity depend about equally on vertical and horizontal compressional stress components in the direction of wave propagation and particle motion (Yin, 1992; Chen et al., 2006). The stress-induced P-wave velocity anisotropy (ϵ) will therefore be greater than the S-wave anisotropy (γ) because the differences of the P-wave velocities in the vertical and horizontal directions are greater than the difference of the SH-wave velocities between vertical and horizontal directions. Hence, ϵ will be greater than γ as observed in Figure 1.4.
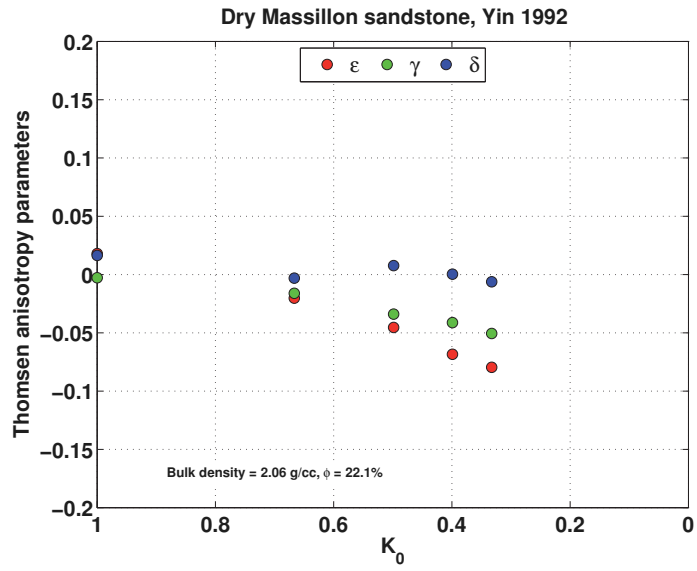
Figure 1.4: Thomsen anisotropy parameters (Thomsen, 1986) as a function of the stress ratio (K_0) for a dry cemented Massillon sandstone of about 22% porosity undergoing axisymmetic compression. Data courtesy Yin (1992).

1.3   Thesis outline

The main part of the thesis consists of three independent papers two of which is already published and one prepared for publication in international geophysical journals. An additional fourth paper included in Appendix A of the thesis is motivated based on analysis and results obtained in chapter 2 by using a different approach to model stress-dependent elastic wave velocities in sandstones. In addition, a short chapter containing concluding remarks is placed in chapter five.

The paper in Chapter 2, **Vp/Vs ratio versus differential stress and rock consolidation - A comparison between rock models and time-lapse AVO data**, presents a simple and straightforward rock physics calibration procedure to assess the stress sensitivity of compressional to shear velocity ratio (V_p/V_s). The objective is model the stress dependence of the velocity ratio as observed from experimental core measurements on sandstones with different degree of consolidation at various differential stresses. By combining a well accepted granular contact model (Hertz-Mindlin model) with the fluid substitution model of Gassmann, we show how to obtain a rock-physics framework including both the differential stress and the degree of rock consolidation. We use the number of grain-to-grain contacts in our model (coordination number) to represent the rock consolidation. For two North Sea field examples (Gullfaks and Statfjord), we calibrate this consolidation parameter to in-situ stress conditions, and compare the V_p/V_s predictions of the overpressured reservoir conditions with those obtained from real seismic time-lapse AVO changes. The calibration exercise gives significant differences in the estimated coordination number for Gullfaks and Statfjord, indicating that the Gullfaks reservoir sandstone is the least consolidated. Hence, the largest AVO-estimated V_p/V_s is obtained for the Gullfaks data. The idea behind the paper is with contributions from both authors. The first author is the main contributor of derivations, graphics, layout and writing of the paper. My co-author's contributions include technical discussions and suggestions, review of text, equations and suggestions towards formulations in the paper.

The paper in Chapter 3, **Using Mindlin theory to model friction-dependent shear modulus in granular media**, we derive based on a well accepted contact model assuming two special contact boundary conditions representing infinite and near zero friction between grains, an explicit expression for the effective shear modulus of a random packing of identical spheres as a function of Mindlin's tangential stiffness based on interparticle contact friction.

Our model predicts a non-linear transition between two special grain contact conditions representing infinite friction and near zero friction. The Mindlin friction term, allowing partial slip across the contact area between pairs of spheres, can be viewed as a parameter accounting for the growing macroscopic intergrain friction in sands or sandstones as burial progresses. The motivation behind our approach is to incorporate the effect of intergrain friction in the prediction of velocities in unconsolidated sands undergoing mechanical compaction. Comparison of elastic properties, e.g. our dynamic shear modulus predictions with experimental data on loose glass bead and sand samples appear to match reasonably well at low confining stress (<5 MPa), but greater deviation is observed with increasing confining stress where both experimental datasets gradually crosses the first few iso-frictional grain contact curves predicted with our model. The sand sample, composed of grains of same size but of higher angularity as compared with the glass beads, has higher dynamic shear modulus and shear velocity which is favorable to explain through grain interlocking. The first author is the main contributor of the idea, derivations, graphics, layout and writing of the paper. My co-authors contributions include technical discussions and suggestions, review of text, equations and suggestions towards formulations in the paper.

The paper in Chapter 4, **Modeling stress- and friction-dependent elastic anisotropy in granular media**, we present a similar approach as that of chapter 3 where new effective moduli expressions of a random dense packing of identical elastic spheres undergoing uniaxial strain loading are derived. Our stating point is a published contact model defined for two special contact boundary conditions representing infinite and near zero grain-to-grain friction. We propose an intermediate model by incorporating the effect of interparticle contact friction through Mindlin's extended tangential contact stiffness. Since the sphere assembly is assumed exposed to uniaxial strain loading, it becomes transversely isotropic with a vertical axis of symmetry (VTI). The effective sphere assembly with frictional contacts is described explicitly either in terms five elastic moduli or by use of the Thomsen notation where all are a function of the Mindlin friction term ($f(\mu)$). Our model predict a decreasing stress-dependent elastic anisotropy with increasing interparticle contact friction and it depends on the net stress ratio ($K_0^{'}$) through $f(\mu)$ and the Poisson's ratio of the solid sphere material. Instantaneous elastic anisotropy is predicted by the model as the grain assembly is exposed to uniaxial strain loading, but it is independent of the applied vertical net stress. The stress-dependent elastic anisotropy is always negative when the applied stress is along the axis of symmetry in the vertical direction. Comparison of P-wave velocity anisotropy

predictions assuming variable interparticle contact friction with experimental data on unconsolidated sand exposed to a uniaxial loading, appear to fit well in between the P-wave velocity anisotropy boundaries representing infinite and near-zero contact friction. This is reasonable since the sand is unconsolidated, without grain cement, and therefore elastically softer with less grain contact friction than that of infinite friction. On the other hand, the sand grains have higher angularity than the smooth sphere model and therefore appear elastically stiffer with higher grain contact friction. The modeling results imply that unconsolidated sands or sandstones under in-situ uniaxial strain loading conditions occurring at shallow depths should appear with quite a large stress-induced elastic anisotropy ($>$-20%) which can complicate seismic imaging and amplitude interpretation. The first author is the main contributor of the idea, derivations, graphics, layout and writing of the paper. My co-authors contributions include technical discussions and suggestions, review of text, equations and suggestions towards formulations in the paper.

The paper in Appendix A, **Stress and fluid sensitivity in two North Sea oil fields - comparing rock physics models with seismic observations**, we apply a different rock physics modeling approach developed by Avseth and Skjei (2011) as to that of Chapter 2 to predict stress sensitivity of elastic wave velocities using the same data as that of Chapter 2. In this case study we assume that the cemented rock will consist of a binary mixture of cemented and uncemented grain contacts, or "patchy cementation". Assuming that the cemented "stiff" grain contacts are stress-insensitive and the unconsolidated "loose" grain contacts are stress-sensitive according to Hertzian contact theory, this hybrid model will allow us to predict the pressure sensitivity in cemented sandstones. The match between rock physics modeling results and seismic observations in terms of Vp/Vs is good. The stress sensitivity of Vp/Vs decreases drastically when sands become cemented, as crack-like porosity at grain contacts are eliminated.

Chapter 2

Vp/Vs ratio versus differential stress and rock consolidation - A comparison between rock models and time-lapse AVO data

V_p/V_s ratio versus differential stress and rock consolidation — A comparison between rock models and time-lapse AVO data

Kenneth Duffaut[1] and Martin Landrø[2]

ABSTRACT

The compressional to shear wave velocity ratio (V_p/V_s) is an important parameter in seismic amplitude versus offset (AVO) analysis, and this parameter plays a key role especially for lithology and fluid prediction methods. The P-wave velocity is a key parameter in traditional pressure prediction methods, because overpressure often results in a velocity reduction. However, for AVO-based pore pressure prediction methods, one expects that the V_p/V_s ratio also is a key parameter. The Hertz-Mindlin geomechanical model predicts a constant V_p/V_s ratio as the differential stress changes in a dry package of identical spheres. Ultrasonic core measurements show increased V_p/V_s ratios as the differential stress decreases, especially for unconsolidated wet sands. Thus, one is likely to assume that the V_p/V_s ratio is dependent on rock consolidation. By combining the Hertz-Mindlin model with the Gassmann model, we show how to obtain a simple rock-physics framework including both the differential stress and the degree of rock consolidation. We use the number of grain-to-grain contacts (coordination number) to represent the rock consolidation. For two field examples, we calibrate this consolidation parameter to in-situ stress conditions, then compare the predicted V_p/V_s ratios for the overpressured reservoir conditions with observed time-lapse AVO changes. The correspondence between modeled and AVO-estimated V_p/V_s ratios is good within the assumed accuracy of the real time-lapse AVO changes. In both cases, we observe an increase in the V_p/V_s ratio as the differential stress decreases. In the first case, a pore pressure increase of 5–7 MPa is measured, whereas the other case shows a pressure increase of approximately 15 MPa. The first reservoir represents a low-to-medium-consolidated sandstone reservoir of 33% porosity on average, whereas the second reservoir is a more consolidated sand with similar porosities (30%).

INTRODUCTION

From various rock-physics studies (Huffman and Castagna, 2001; Prasad, 2002) we know that the compressional to shear wave velocity ratio (V_p/V_s) is increasing with decreasing differential stress (or net stress). However, the reliability of such acoustical core measurements will to some extent be influenced by core damage caused by unloading and reloading, and whether it is feasible to record reliable S-wave energy in the lower differential stress regime, i.e., ≤ 3 to 5 MPa. It is reasonable to assume these effects, among other factors, to be more pronounced at the lower end of the differential stress scale. Hence, less reliable estimates of the V_p/V_s ratio might be the consequence. Therefore, it might be useful to compare ultrasonic core measurements with other types of measurements, as for instance time-lapse seismic or 4D seismic. Time-lapse seismic surveys might be a complementary tool to study how the V_p/V_s ratio varies as a function of differential stress, and this is the focus of this paper.

There is a distinction between effective stress and differential stress (Siggins and Dewhurst, 2003). Differential stress is simply the difference between the stress tensor (σ_{ij}) and the pore pressure (P_{pore}). Effective stress (σ'_{ij}) is defined as (Brandt, 1955)

$$\sigma'_{ij} = \sigma_{ij} - nP_{\text{pore}}\delta_{ij}, \qquad (1)$$

where n is the effective stress coefficient and δ_{ij} represents the Kronecker delta. The pore pressure will only contribute when i = j. The effective stress coefficient can be estimated in various ways (Siggins and Dewhurst, 2003). Siggins and Dewhurst (2003) show measured values of n versus the differential stress. In most cases, $n = 1$ is assumed, but Siggins and Dewhurst have shown that this approxima-

tion might be inaccurate. However, in this paper we will assume that the effective stress coefficient is close to 1, and correspondingly, we will assume that the effective stress is equal to the differential stress. If a relationship between n and differential stress exists, it will be straightforward to correct our method to include this stretching effect. The fact that we actually do not know the effective stress coefficient n is a limiting factor for quantitative use of rock-physics measurements for pore pressure estimation. In a rock-physics experiment, we measure the differential stress, whereas in a reservoir we measure the pore pressure (or fluid pressure).

Siggins and Dewhurst (2003) find a distinct difference between ultrasonic measurements on dry and oil-saturated core samples: The V_p/V_s ratio increases with decreasing differential stress in the oil-saturated case, whereas a decrease is observed for the dry core material. The last observation is in contrast to the core data that we use in this paper, where a slight increase in V_p/V_s ratio also is observed for dry core samples.

Huffman and Castagna (2001) show that the V_p/V_s ratio variation with effective pressure strongly depends on the clay content of the rock sample; the increase is weaker for shaly sandstones compared with clean sandstones. The main effect leading to the strong increase in V_p/V_s ratio for low effective pressures is caused by the shear wave velocity approaching zero.

Prasad (2002) measured shear wave velocities on the order of 300 m/s on fully saturated cores, and a corresponding pressure wave velocity of 1750 m/s. Other measurements performed on both dry and wet samples (Capello De P and Batzle, 1997) show an almost constant V_p/V_s ratio as a function of effective pressure. Figure 1a shows the average V_p/V_s ratio versus differential stress obtained from 29 dry core ultrasonic measurements from the Gullfaks field. The 29 cores represent various formations and therefore also various sandstone porosities.

A similar graph derived from 34 dry core measurements are shown for the Statfjord Field in Figure 1b. We notice a weaker increase in V_p/V_s ratio as the differential stress approaches zero, compared with the results of Huffman and Castagna (2001) for both res-

ervoirs. The degree of cementation of the rock might be one cause for this discrepancy; wet versus dry core measurements is another cause. Damage of the core sample resulting from unloading and reloading is a third possible explanation.

In a specific segment at the Gullfaks field in the North Sea, a significant pore pressure increase caused by water injection was measured. The measured pore pressure (repeated formation testing [RFT] measurement in the well) increased from approximately 32 to 39 MPa between the base and monitor surveys, corresponding to an assumed drop in differential stress of 7 MPa.

An example on how time-lapse AVO analysis can be used to discriminate between pressure and fluid changes in this segment is discussed by Landrø (2001). Another example demonstrating how time-shift analysis can be used to interpret pressure variations with depth is discussed in Landrø et al. (2001).

In a second example from the Statfjord field (Rognø et al., 1999), a pore-pressure increase up to 15 MPa is measured in different wells, and observed on time-lapse seismic data. By studying AVO changes over production time, we will use these two field examples to study how the V_p/V_s ratio varies as the pore pressure increases. Furthermore, the rock-physics observations support the need for a simple model including both pressure variations and rock consolidation degree.

The simplest model for predicting pressure and shear wave velocity changes as a function of differential stress is the Hertz-Mindlin (H-M) model. Although the H-M model is insufficient to describe a real rock sample, we have chosen to use this model in this work. The advantage of the H-M model is primarily because it is simple and includes the basic physical effects (both for pressure and shear forces).

The most obvious disadvantage with the H-M model is the assumption related to identical spherical grains. This is a severe simplification compared with, for instance, thin sections of sands (Figure 7) from the two reservoirs we study. Another shortcoming is that this model assumes a dry rock, and therefore we will combine the H-M model with the Gassmann model to account for saturation effects. A third major shortcoming is related to presence of cement. The H-M model only is valid for unconsolidated granular sediments.

When we compare compressional and shear wave velocities predicted by the H-M model, we find that the H-M model often overestimates the velocity variation with differential stress. However, because the model handles both shear and normal stresses, one might expect that the predicted V_p/V_s ratio might be more accurate than the separate estimates of each velocity.

Our hope is that the H-M model captures the zero-order pressure effect, and that we do the same error for both V_p and V_s for the higher order effects. Furthermore, we will use the number of contact points per grain or coordination number as a rock consolidation parameter. This means that we are adjusting the H-M model to represent a physical property that it was not designed for. However, we think that reinterpretating this parameter is justified by the simplicity, and the fact that when we use this parameter as a fudge factor, we achieve a straightforward way to fit observed time-lapse seismic AVO data to a given reservoir rock.

The rock consolidation degree is probably dependent on several other parameters in addition to the number of contact points per grain, such as the contact area per grain (cement), the shape of each grain, the pore fluid type, and so forth. Bachrach et al. (2000) and Zimmer et al. (2007) discuss the effect of slip free or rotation between adjacent grains. Allowing this to occur, they show that contact models accurately predict the magnitude of the velocities for uncon-
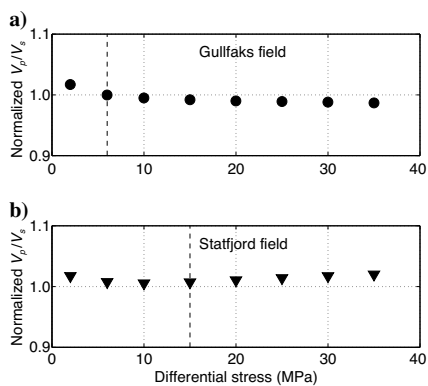

Figure 1. (a) Normalized average V_p/V_s ratio versus differential stress based on ultrasonic core measurements of 29 dry samples from the Gullfaks field. (b) The corresponding core measurements based on averaging 34 dry core measurements of the Statfjord Field. Notice a weak increase in the V_p/V_s ratio as the differential stress approaches zero. The initial differential stress is approximately 6 MPa at Gullfaks but 15 MPa at the Statfjord Field.

solidated sands. From a practical point of view, we have decided to put all these effects into one parameter, and assumed that we can find one consolidation parameter for each type of reservoir rock.

THE COMBINED H-M AND GASSMANN MODEL

Various contact models have been proposed to estimate effective moduli of a granular rock. Mavko et al. (1998) present some of these models in, *The Rock Physics Handbook*. The H-M model (Mindlin, 1949) can be used to describe the properties of precompacted granular sediments before compaction. The effective bulk modulus of a dry random identical sphere packing (porosity $\sim 36\%$) is given by

$$K_{\text{dry}} = \left(\frac{C_p^2 (1 - \phi)^2 G^2 P}{18 \pi^2 (1 - \nu)^2} \right)^{\frac{1}{3}}, \quad (2)$$

and the effective dry shear modulus is given by

$$G_{\text{dry}} = \left(\frac{5 - 4\nu}{5(2 - \nu)} \right) \left(\frac{3 C_p^2 (1 - \phi)^2 G^2 P}{2 \pi^2 (1 - \nu)^2} \right)^{\frac{1}{3}}, \quad (3)$$

where ν and G are the Poisson's ratio and shear modulus of the solid grains, respectively; ϕ is the porosity; C_p is the average number of contacts per grain or coordination number; and P is the differential or net stress (i.e., vertical differential stress, P $= \sigma'_{33}$ or σ'_v). The Mindlin formulas given earlier, assume that there is no slip at the grain contacts or grain rotation.

The velocities for a dry homogeneous isotropic rock are given as

$$V_{P_{\text{dry}}} = \sqrt{ \frac{K_{\text{dry}} + \frac{4}{3} G_{\text{dry}}}{(1 - \phi) \rho_{ma}} } \quad (4)$$

$$V_{s_{\text{dry}}} = \sqrt{ \frac{G_{\text{dry}}}{(1 - \phi) \rho_{ma}} }, \quad (5)$$

where $V_{P_{\text{dry}}}$ and $V_{s_{\text{dry}}}$ represents the P- and S-wave velocity, respectively, and ρ_{ma} is the mineral matrix density. Inserting the effective dry bulk modulus equation 2 and effective dry shear modulus equation 3 into velocity equations 4 and 5 and computing the V_p/V_s ratio yields (assuming ν of quartz equal to 0.07)

$$\left(\frac{V_p}{V_s} \right)_{\text{dry}} = \sqrt{ \frac{(10 - 7\nu)}{(5 - 4\nu)} } \approx \sqrt{2}. \quad (6)$$

This means that according to the simplest granular model (Hertz-Mindlin), the V_p/V_s ratio should be constant as a function of confining stress when assuming dry rock composed of, e.g., quartz grains. Figure 2 shows the variation in the predicted dry velocities and velocity ratio for an increasing differential stress.

The H-M model assumes that the sand grains are spherical and that there is a certain area of grain-to-grain contacts. A major shortcoming of the H-M model is that in the limit of unconsolidated sands, both P- and S-wave velocities will have the same behavior with respect to pressure changes, as shown in equation 6. Combining the Hertz-Mindlin predictions with the Gassmann model (e.g., introducing fluids in the pore system of the rock, Gassmann, 1951) will ensure that the P-wave velocity approaches the suspension velocity at zero differential stress (and not zero as the H-M model predicts for

dry rocks). This difference in dry versus saturated rock velocities appears in Figure 2. Appendix A outlines further discussion on the relation between dry and wet modulies.

OBSERVED PRESSURE EFFECTS AT THE GULLFAKS FIELD (POSTSTACK ANALYSIS)

In our first field example, we will use time-lapse seismic data from the Gullfaks field. The average porosity in this field is 33%, and the rock consolidation is judged to be low to medium based on measurements of Young's moduli (E_{50}) of approximately 2.5 GPa at in situ stress conditions. Close to one of the water injectors at Gullfaks, a significant pore pressure increase was measured in well 34/10-B-33 (hereafter named B-33) on the order of 5–7 MPa.

Well B-33 started to inject 3000 m³ of water per day into the Cook Formation in the summer of 1995, about one year before the monitor seismic survey was acquired in 1996. A map view of the amplitude differences observed between the base and monitor survey at the top Cook interface appears in Figure 3. We observe significant amplitude changes close to the injector well. Because we also observe these amplitude changes below the original oil-water contact (OWC), we may conclude that these amplitude changes are caused by the observed pressure increase in well B-33. A detailed comparison of stacked seismic data from 1985 and 1996 is shown in Landrø et al. (2001), where the distinct amplitude increase at the top reservoir interface is evident.

Log analysis of wells in the vicinity of well B-33 was done to estimate the V_p/V_s ratio for the Cook reservoir sand and the overlying shale. A distinct drop in V_p/V_s ratio is observed in Figure 4 at the shale-sand interface, and this ratio remains constant at approximately 1.9 throughout the reservoir unit.

The sands in this section are within neighboring formations and do not necessarily represent the Cook sand. Despite this limitation, we assume that the V_p/V_s ratio is 1.9 also for the Cook Formation, whereas the velocity ratio of the overlaying shale was estimated to be 2.6. There is some uncertainty coupled to the V_p/V_s ratio estimates for both the Cook sand and the overlaying shale because of incomplete logging across these formation intervals. The average acoustic
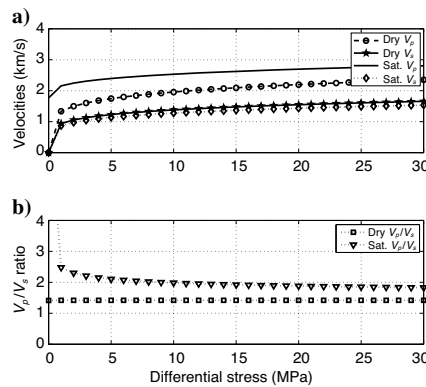

Figure 2. (a) Differential stress versus dry and saturated P- and S-wave velocities estimated from the combined Hertz-Mindlin-Gassmann model. (b) The corresponding V_p/V_s ratios derived from the dry and wet velocities.

log parameters in Table 3 are used to generate seismic half-space models.

Rock-physical measurements performed on Gullfaks core material show a clear reduction in the P-wave velocity for a measured pore pressure increase of 5–7 MPa. Figure 5 shows how the P-wave velocity varies with differential stress according to the H-M model in comparison with various types of ultrasonic core measurements. Although the various modeled and experimental curves deviate, especially for higher differential stresses, they all indicate a velocity drop in the range of 15%–20% when the differential stress is reduced by 5 MPa. The actual in situ vertical differential stress at Gullfaks is close to 8 MPa, and not 5 MPa as shown in Figure 5.

The 5 MPa measurement is close to the mean differential stress one obtains when using the in-situ stress numbers of the Gullfaks field, Table 1. The core measurements were normalized to this mean differential stress. The uncertainties related to estimation of vertical and horizontal stresses are greater than the corresponding uncertainty of the pore pressure estimates. Furthermore, we see from Figure 5

that the H-M model deviates from the ultrasonic core measurements, especially for high differential stresses (6–8 MPa). According to the H-M model, the P-wave velocity is proportional to the differential stress raised to the power of 1/6 (black curve). Using 1/10 as the exponent (red curve) instead of 1/6 gives a much better fit with the rock-physics measurements (blue curve).

All rock-physics measurements were performed on dry core samples, and the blue curve in Figure 5 represents the average of 29 core samples from the Gullfaks field. As a complementary curve (green), we also have sketched the behavior of a synthetic sandstone made at in situ stress conditions before being exposed to stress release, which is based on Nes et al.'s experiments (2000). This curve shows far less changes in P-wave velocity when the differential stress is increasing above the in-situ conditions. For our purpose, these deviations for increased differential stresses, as compared with the initial vertical differential stress, are unimportant because we will study only an increase in pore pressure, hence reduced differential stress.
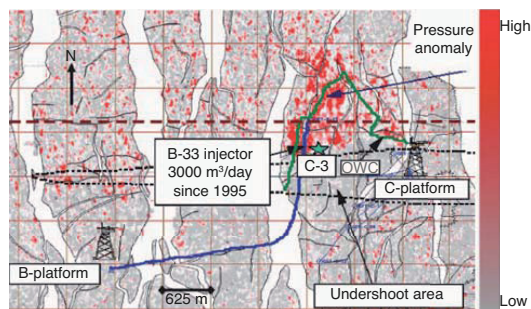

Figure 3. Seismic amplitude difference between 1996 and 1985 data for the top Cook interface at the Gullfaks field. The B-33 well started to inject 3000 m³ of water per day in 1995, and the amplitude anomaly shown on this figure is interpreted as being caused mainly by the pore pressure increase resulting from the water injection. The original oil-water contact line appears in green. The amplitude anomaly extends below this line, into the water zone, indicating a pressure effect. The inline shown in Figure 9 is indicated by a dashed line.
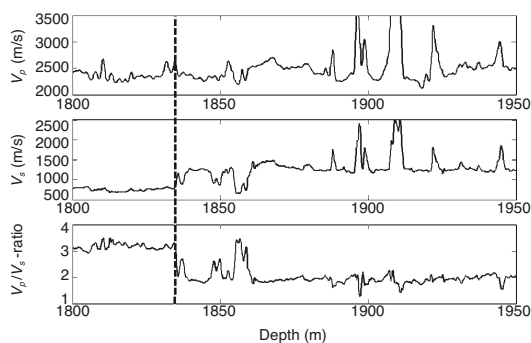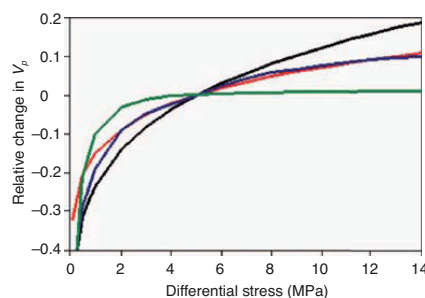

Figure 4. Acoustic logs from a neighboring well of B-33 at the Gullfaks field. From top to bottom: the P-wave, S-wave velocity, and the velocity ratio. The dashed line indicates an interface between shale and an analog of the Cook sand. Notice the drop in the V_p/V_s ratio at this level (from 3 to 2). This well does not cover the Cook formation.

Figure 5. Relative change in the dry P-wave velocity as a function of the differential or net stress predicted by the Hertz-Mindlin model (exp = 1/6, black curve), modified Hertz-Mindlin model (exp = 1/10, red curve), dry core measurements (29 dry core samples, Gullfaks Field, blue curve) and synthetic core measurements (green curve). Here, we have assumed about 5 MPa initial net stress representing the mean net stress at the Gullfaks field. The synthetic core measurement curve does not represent real measurements from the Gullfaks field, but has been drawn on the basis of the published work by Nes et al. (2000).

Table 1. Initial stress conditions at the Gullfaks field. Using these numbers in equation 1 gives initial horizontal and vertical differential stresses of 4.5 and 8 MPa, respectively, assuming an effective stress coefficient (n) equal to 1.

Parameters (MPa)	Gullfaks field
Vertical stress $= \sigma_v$	40
Horizontal stress $= \sigma_H = \sigma_h$	36.5
Pore pressure $= P_{pore}$	32
Hydrostatic pressure $= P_{Hyd}$	18
Vertical differential stress $= \sigma'_v$	8
Horizontal differential stress $= \sigma'_h$	4.5
Geopressure $= P_{pore} - P_{Hyd}$	14

CALIBRATION OF THE COMBINED ROCK-PHYSICS MODEL — GULLFAKS FIELD

The V_p/V_s ratio of a typical oil-saturated reservoir sand at Gullfaks is approximately 1.9 at initial stress conditions which is summarized in Table 1.

The first step in the calibration procedure is to fix the rock shear modulus G to 44 GPa (Mavko et al., 1998) assuming the solid grains to represent quartz. A Poisson's ratio of 0.07 is therefore used in equations 2 and 3. Figure 6 shows the V_p/V_s ratio variations with the degree of rock consolidation (represented by the number of contact points per grain, C_p) and differential stress.

The vertical arrows pointing downwards show the apparent number of contacts per grain at in situ stress conditions. With increasing pore pressure, one is likely to assume that the number of contact points decreases (dotted arrows) although we have limited knowledge on how the C_p-number varies when lowering the differential stress. Intuitively, we expect a reduction. Figure 7 shows a thin section of the Tarbert reservoir sand at the Gullfaks field together with the Tarbert sand of the Statfjord field. The best Cook sands at Gullfaks have a similar porosity as the Tarbert Formation. We observe that the Tarbert sand at the Gullfaks field is better sorted than the Tarbert sand at Statfjord. Furthermore, the number of contact points per grain appear to be higher for the Statfjord sample.

We will discuss the Statfjord case in more detail in later sections. A more detailed plot of V_p/V_s ratios versus differential stress (for the Gullfaks) is shown in Figure 8a for varying numbers of contact points (C_p equals 3, 6, and 100, respectively).

For the Cook reservoir at Gullfaks, we estimate the initial vertical differential stress at 8 MPa, whereas for calibration we choose to use the mean differential stress of 6 MPa. Based on a simple calibration (indicated by the solid line in Figure 8a), we find that $C_p = 6$ matches this observation. According to the ultrasonic dry core measurements, the V_p/V_s ratio for the two samples representing the Cook Formation (not shown) is equal to 1.7 at 6 MPa differential stress and 1.9 at 2 MPa differential stress. The value of 1.7 is somewhat lower than the log-derived value of 1.9, which is mainly because of dry versus wet material measurements. We have chosen to use the well log value in this study.
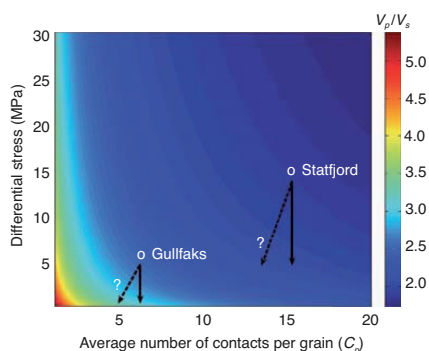
The observed increase in V_p/V_s ratio based on the dry rock core measurements is approximately 12% for the two samples representing the Cook Formation. A similar increase based on the calibrated rock-physics model is 14%. The measured pore pressure increase is on the order of 5–7 MPa, which means that the vertical differential stress at the time of the monitor survey is likely to be close to zero. According to the calibrated rock-physics model (Figure 8a), this should correspond to a V_p/V_s ratio around 2.8. However, we realize that an effective stress coefficient (n) less than 1.0 (equation 1) will reduce this number significantly.

COMPARISON BETWEEN TWO-LAYER ZOEPPRITZ MODELING AND TIME-LAPSE AVO — GULLFAKS FIELD

Figure 9 shows cross sections of the near-, mid-, and far-offset stacks of the 1985 and 1996 data sets from Gullfaks field. The aver-
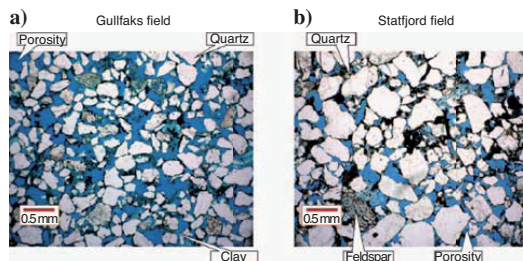
Figure 7. Thin section samples from the Tarbert reservoir sandstone at (a) Gullfaks (left) and Statfjord fields, respectively. We observe that the Gullfaks sand on average has fewer grain contacts than the Tarbert sand at Statfjord, and the Gullfaks sample appears to be better sorted with respect to grain size. The log derived total porosities are 33% and 30% for the Gullfaks and Statfjord fields, respectively.
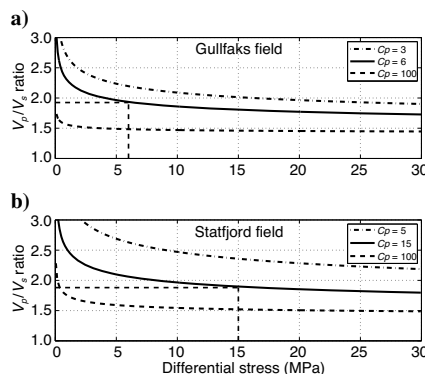
Figure 8. (a) V_p/V_s ratio versus differential stress for various number of contact points per grain (C_p) derived from the combined Hertz-Mindlin-Gassmann model for the Gullfaks Cook sand using parameters from Table 6. A $C_p = 6$ corresponds to an observed V_p/V_s ratio of 1.9. (b) A similar calibration is done for the Tarbert-sand at the Statfjord field using very similar numbers for the rock properties, Table 6. We observe that $C_p = 15$ corresponds to the observed V_p/V_s ratio of 1.88 for the Statfjord case.

Figure 6. V_p/V_s ratio predicted by the combined Hertz-Mindlin-Gassmann model versus differential stress and average number of contacts per grain (C_p). We assume quartz grains for the modeling using parameters from Table 6.

age dip angle of the top Cook interface is about 10° along this inline, and the average angle of incidence of the near-, mid-, and far-offset stacks are estimated by ray tracing to be 15°, 23°, and 31°, respectively.

The significant amplitude brightening, decreasing negative amplitude value from 1985 to 1996 at the top reservoir (top Cook) event is clearly observed. Furthermore, we see that the amplitudes increases, but obtain smaller negative values, with offset or angle for the top reservoir event. This means that the increased pore pressure leads to an amplitude-dimming, positive-amplitude gradient, with offset in this case.

To quantify the observed AVO-effect shown in Figure 9, horizon flattening was applied to the central part (dashed line in Figure 9) of the top reservoir reflection. After horizon flattening, the rms amplitude was computed for each trace within a 60-ms window. There is a significant variation in the rms-level along the reflector, and the variation is probably caused by various types of seismic noise, such as remaining multiple energy, diffracted noise from overlaying lenses, inaccurate processing, and so forth. The average rms amplitudes and the corresponding standard deviations for each offset stack are given in Table 2. We notice that the average standard deviation is 28% (averaged over the three offset stacks).

To compare the predicted V_p/V_s ratios with observed AVO changes, a simple two-layer isotropic Zoeppritz modeling is performed using the well-derived seismic parameters given in Table 3.

In addition to the base case, four monitor cases are modeled: One representing no change in V_p/V_s ratio ($V_p/V_s = 1.9$) reducing both P- and S-wave velocities by 15% to simulate a pore pressure increase, another representing $V_p/V_s = 2.8$, and a third representing $V_p/V_s = 7$. A fourth case was modeled by keeping the $V_p/V_s = 1.9$ in addition to introducing vertical cracks because of fracturing (see Appendix B). All modeling results are summarized in Figure 10, where we also show the observed top target amplitude response of the 1996 seismic data (solid circles).

The average rms amplitudes were computed for 46 traces within a 60-ms window around the top reservoir interface. The vertical bars indicate one standard deviation of the rms value. A global wavelet scalar (derived from well-tie) of 0.000015 was applied to the seismic data to enable comparison of real and synthetic AVO responses. Based on this comparison, one likely assumes that the V_p/V_s ratio increases from 1.9 to well above 3, because of the increased pore pres-

sure. According to the calibrated rock-physics model (Figure 8a), a V_p/V_s ratio around 3 is expected, whereas the real seismic AVO response suggest a higher velocity ratio, most likely around 7. This observed deviation between modeled and time-lapse AVO-based velocity ratios is consistent with the Bachrach et al. (2000) experiment on unconsolidated sand. They compared V_p/V_s ratio measurements on unconsolidated beach sand with Hertz-Mindlin contact theory. Their explanation of the underprediction of the H-M-model is by assuming slip at the grain contacts of the real sand, reducing the shearing between grains. Hence, V_p/V_s ratio increases.

Discrepancy also is observed between the AVO response of the field data from 1985 (left column in Figure 9) and the AVO modeling based on average well log values (Figure 10). There are several possible causes for this discrepancy. First, the seismic reflectivity is much weaker in 1985 than in 1996, and thus the amplitude versus offset or angle is suffering from the low signal-to-noise ratio. Furthermore, the average acoustic log values are questionable at this location because of incomplete logging across the shale-sand interface, leading to a somewhat stronger amplitude response both for zero and far offsets. Trusting the seismic amplitude response of the partial stacks at the top Cook sand, the shale-sand interface appear transparent, indicating a very small to no acoustic impedance and V_p/V_s contrast between the overburden and the Cook sand. This contradicts the well logs in the area (Figure 4). Therefore, we have chosen not to compare the field data from 1985 with the synthetic 1985 AVO response (open circle symbol, Figure 10).

OBSERVED PRESSURE EFFECTS AT THE STATFJORD FIELD (POSTSTACK ANALYSIS)

In our second field example, we use time-lapse seismic data from the Statfjord field in the North Sea. The upper Jurassic Brent Group

Table 2. The rms values estimated across a 60-ms window around the top Cook interface at Gullfaks. The standard deviations were estimated based on 46 crossline traces.

	Near (15°)	Mid (23°)	Far (31°)
rms-average	8574	6549	5500
st-deviation	2387	1597	1821

Table 3. The average seismic parameters for shale and sand are used for the five Gullfaks half-space seismic models. The P- and S-wave velocities of the monitor 1 case (layer 2) is reduced by 15% by respect to the in situ stress conditions resulting from a pore pressure increase. In the latter two cases, only the S-wave velocities are changed for the given V_p/V_s for layer 2. A fifth case is made by introducing vertical cracks because of fracturing. Model parameters for this case are listed in Table 6.

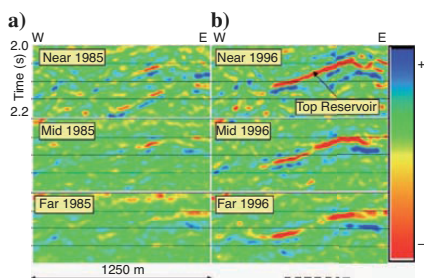|	V_p(m/s)	V_s(m/s)	ρ(kg/m³)	V_p/V_s
Layer1 (Shale)	2600	1000	2300	2.6
Layer2 (Baseline)	2500	1315	2100	1.9
Layer2 (monitor 1)	2125	1118	2100	1.9
Layer2 ($V_p/V_s = 2.8$)	2125	759	2100	2.8
Layer2 ($V_p/V_s = 7.0$)	2125	303.6	2100	7.0

Figure 9. Near-, mid-, and far-offset stacks (top to bottom) from (a) 1985 and (b) 1996. Notice the significant amplitude decrease (amplitudes becomes more negative) from 1985 to 1996 for the near offset data at top reservoir (top Cook). The dashed line (below the 1996 data) indicates the selected area for the quantitative amplitude analysis.

(Tarbert and Ness formations) has been by far the most prolific reservoir unit since production started in 1979. (Hesthammer et al., 1999). The average porosity in this reservoir unit is about 30%, and the sandstone is medium consolidated with a Young's moduli (E_{50}) of approximately 9 GPa at initial in-situ stress conditions (Table 4). Table 5 lists the initial in situ stress numbers of the Statfjord field.

During production the pore pressure decreased to a minimum of approximately 32 MPa in 1992–1993 (pure pressure depletion), a net pore pressure decrease of about 6 MPa. Downflank water injection was used to maintain and increase the reservoir pressure, and the pore pressure increased from 32 to about 35 MPa as a result. Near the injectors, the pore pressure is expected to build up (typically 15 MPa above the minimum pressure of 32 MPa), resulting in a reduction in P- and S-wave velocity of the order of 8%–10%, whereas a 6-MPa pore pressure reduction (38 to 32 MPa) gives an expected increase in velocities in the order of 3%–4%. These estimates are derived from ultrasonic measurements done on 34 dry core samples. Figure 1b shows the normalized V_p/V_s ratio for the same core samples. A slight increase of the V_p/V_s ratio is observed for low and high differential stresses.

In the Statfjord time-lapse seismic data, there are examples of amplitude brightening in the immediate vicinity of Brent water injectors, which are interpreted to be caused by a pore pressure increase. Figure 11 shows a segment of an amplitude difference map (1997–1991) extracted along the top reservoir interface (Top Tarbert Formation).

An amplitude increase is observed as a circular area around well 33/9-A-4. The diameter of the anomaly is approximately 4–500 m. This is consistent with the expected extent (based on simple reservoir engineering considerations) of a pressure buildup in the vicinity of an injector in this highly permeable formation. The average injection pressure is about 47 MPa (about 15 MPa higher that the average

pore pressure), and the pressure gradient away from the injection point is normally steep — in the order of a few hundred meters. Because the Tarbert reservoir is relatively homogeneous with high permeability (5–7 Darcys), there is rarely any pore pressure buildup over time. The pressure is distributed effectively, which explains why water injection provides excellent pressure support in these reservoirs. If an injector is shut down, only a few hours pass before the pressure is normalized close to the injection point. Consequently, because there is no pressure buildup, 4D seismic response to a pressure increase can only be seen when the injector was offline during the first seismic acquisition, and online during the second. Well 33/9-A-4 was shut down when the 1991 seismic survey was acquired and online during the acquisition of the 1997 monitoring survey.

CALIBRATION OF THE COMBINED ROCK-PHYSICS MODEL — STATFJORD FIELD

The same calibration procedure as described for the Gullfaks field is repeated for the Statfjord example. The result of the calibration is shown in Figure 8b, where the average number of contacts per sphere (C_p) is estimated to 15. Compared with the thin section dis-

Table 4. Initial stress conditions at the Statfjord field. The initial horizontal and vertical differential stresses are 8 and 15 MPa, respectively, when assuming an effective stress coefficient (n) equal to 1.

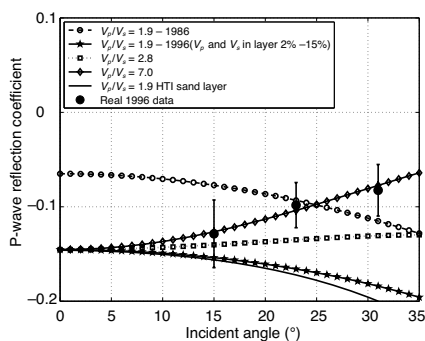| Parameters (MPa)	Statfjord field
Vertical stress = σ_v	53
Horizontal stress = $\sigma_H = \sigma_h$	46
Pore pressure = P_{pore}	38
Hydrostatic pressure = P_{Hyd}	22.5
Vertical differential stress = σ_v'	15
Horizontal differential stress = σ_h'	8
Geopressure = $P_{pore} - P_{Hyd}$	15.5

Figure 10. Two-layer Zoeppritz modeling based on log-derived parameters (Table 3) for the Gullfaks field. The baseline reflection coefficient (open circle symbol) is relatively weak, and the absolute amplitude increases with angle. For the monitoring scenarios, we have assumed a 15% velocity drop caused by a reduced differential stress, and various V_p/V_s ratios. The solid circles represents the average rms-values at the top Cook reflector of the 1996 near-, mid-, and far-offset stacks (Figure 9). The error bars represent ± one standard deviation obtained from averaging. We observe that real time-lapse amplitude measurements fit reasonably well assuming an average V_p/V_s ratio equal to 7. The AVO response of the half space model between an isotropic shale overlying an HTI medium (solid line) simulating a vertically fractured reservoir has the same trend but is slightly boosted with respect to the monitor 1 case (star symbol).
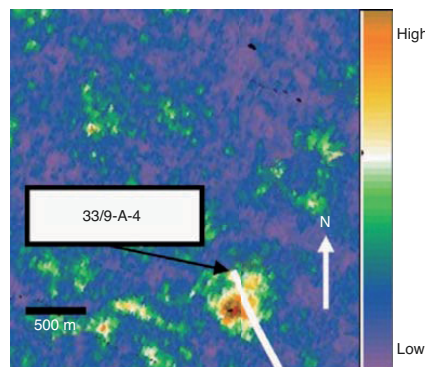

Figure 11. A seismic amplitude difference map between the 1997 and 1991 data sets for the top Tarbert interface at the Statfjord field. The pore pressure increase in well 33/9-A-4, resulting from water injection is about 15 MPa above a reservoir pressure of 32 MPa. We observe a circular-shaped anomaly on the amplitude difference map which is interpreted as a pure pressure effect.

played in Figure 7, it is reasonable to expect a higher C_p number for the Statfjord case compared with the Gullfaks case because the Tarbert sand is more poorly sorted; hence, we would expect a larger number of contacts per grain.

In addition, differences in mechanical packing of the sands may contribute in explaining the deviation between the estimated C_p numbers obtained for the two fields. This, however, does not necessarily mean that a thorough thin section analysis of rock samples from the Statfjord field will give the same number of contact points per grain as estimated by our calibration procedure. For our purpose we, consider this C_p number as an empirical calibration parameter that forces the combined Hertz-Mindlin-Gassmann model to match the average V_p/V_s ratio derived from well logs.

PRESTACK TIME-LAPSE OBSERVATIONS — STATFJORD FIELD

Prestack seismic data for both the 1991 and 1997 surveys were available for this time-lapse study. Prior to the analysis, the noise level of the prestack seismic gathers was reduced by first stacking five adjacent common offset traces around the well location. Second, these five super-gathers were further stacked to a single "super-super" gather centered at the well position. The final result is shown in Figure 12 after offset-to-angle transformation.

We believe this "super-super-angle gather" is a good representation of the amplitude versus angle (AVA) behavior around the injector. Furthermore, this extensive stacking is assumed to increase the signal-to-noise ratio of the time-lapse AVA data. A single scalar was applied to match the 1997 to the 1991 data. From Figure 12 we observe a time-lapse amplitude decrease, decreasing negative value, of
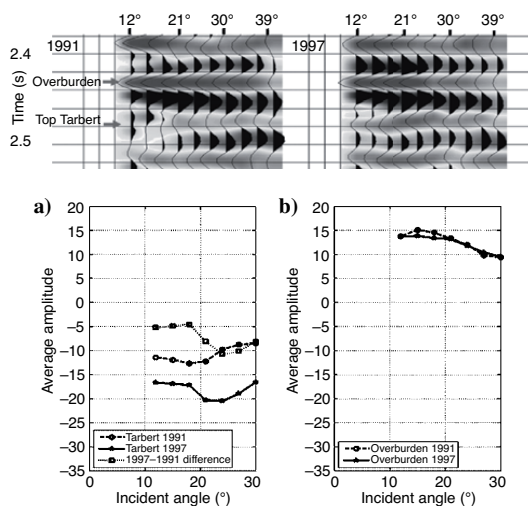
approximately 50% for angles between 12° and 18°, and approximately 100% amplitude decrease for angles between 21° and 30°. For a 350-m s-wide window above the top Tarbert interface, we observe only small time-lapse amplitude changes as expected.

Synthetic data corresponding to the angle gathers shown in Figure 12 (assuming a pore pressure increase of 15 MPa) are shown in Figure 13, demonstrating an amplitude decrease in the range of 30%–50% which is on the order of magnitude of field data observations shown in Figure 12. The deviation between field and synthetic time-lapse differences is most pronounced for small angles, whereas moderate to large angles show a fairly good correspondence. The deviation in time-lapse amplitude differences at small angles might be because of remanent multiple energy in the 1991 seismic data. The presence of this kind of energy is suggested by the interfering events that are observed for the two-three near-angle seismic traces in Figure 12.

As in the Gullfaks case example, five-half space models including the base case of 1991 are derived from well logs (Table 5).

One represents no change in the V_p/V_s ratio ($V_p/V_s = 1.88$) by reducing both P- and S-wave velocity by 10%; a second simulates a pore pressure increase, and two others represent a V_p/V_s of 2.1 and 5, respectively. A fifth model is made by keeping the $V_p/V_s = 1.88$ in addition to introducing vertical cracks resulting from fracturing (see Appendix B). The deviation between the two-layer modeling and the ray-trace modeling is negligible, confirming the validity of the simple half-space models.

All modeling results are summarized in Figure 14, where the observed amplitude changes of the time-lapse seismic data also are

Figure 12. Seismic "super-super-angle gathers" of the 1991 and 1997 data set at the A-4 well location, with nonreservoir interface and Top Tarbert reflectors (reservoir interface) shown (top figure). (a) AVA-response extracted along the top Tarbert trough reflector and (b) AVA-response (rms value) extracted in an overburden interval just above the reservoir. The time-lapse amplitude difference of the top reservoir reflector between the 1997 and 1991 data sets is shown as squares in (a).

Figure 13. Ray-traced synthetic AVO or AVA-gathers at the A-4 well simulating a pore pressure increase of 15 MPa (causing a P- and S-wave velocity decrease of about 10%). The 1D earth model used as input to the seismic modeling is isotropic. The time-lapse amplitude difference at the top reservoir reflector (top Tarbert) is shown as the dotted square symbols in (a). (b) No amplitude difference is seen for the overburden reflector, as expected because no changes have been applied.

shown (solid circles). A global amplitude scalar of 0.0054 was applied to the field data to enable comparison with the synthetic AVO curves of the half-space models. Based on comparison between field and modeled AVO behavior, it is likely to assume that the V_p/V_s ratio has not changed much because of the pore pressure increase. According to the calibrated rock physics model (Figure 8), a V_p/V_s ratio around 2.0 is most likely (the postinjection vertical differential stress is assumed to be around 6 MPa), which is in good agreement with the seismic observations, especially for the mid-far angle range (beyond 15°).

DISCUSSION

Recent time-lapse seismic studies show that for most cases the observed amplitude and time-shift effects are in reasonable agreement with changes predicted from rock-physics models and measurements. However, ultrasonic core measurements of especially the shear wave velocity at low differential stresses are probably more uncertain than corresponding measurements made at higher differential stresses. The effect of unloading and reloading of a core sample is discussed in Nes et al. (2000). Therefore, time-lapse AVO studies or alternatively time-lapse 4-C studies can add additional information on how the V_p/V_s ratio varies with differential stress, especially in areas close to an injection well.

However, there are significant uncertainties associated with this approach. Varying dip angle of the top reservoir interface, overburden distortions, absorption, anisotropy, and remanent multiple energy (especially at near offsets) are examples of effects that will increase the uncertainty in our time-lapse AVO analysis. Both AVO data sets have been prestack time migrated prior to the analysis, which should ensure better quality of the amplitude information used in this study.

The combination of two well-known rock-physics models, the Hertz-Mindlin granular model and the Gassmann model, is simple and straightforward, and motivated by keeping things simple and capturing the lowest order physical effects. Effects such as nonspherical grain shapes, uneven grain sorting, clean grain contact surfaces, and so forth are not taken into account by the H-M model.

Strictly speaking, this model is valid only for unconsolidated sands. Still, we hope that for estimation of the V_p/V_s ratio as a function of differential stress, this model also is valid for more consolidated rocks. The main motivation for combining this model with the Gassmann model is to ensure that the P-wave velocity approaches the suspension velocity as the differential stress approaches zero. Near the same limit, the shear wave velocity will approach zero, leading to infinite V_p/V_s ratios for very low differential stresses.

We think that this effect is observed both for ultrasonic core measurements (Huffman and Castagna, 2001), as well as for the Gullfaks time-lapse seismic case study presented here. It is not as pronounced for the Statfjord case because the vertical differential stress does not approach zero ($\sigma_v' = 53$–47 MPa $= 6$ MPa) in the postinjection phase. We find that the calibrated Hertz-Mindlin-Gassmann model predicts a V_p/V_s ratio of about 3 for the Gullfaks case, where we assume that the differential stress in the post-injection phase is close to zero. The most likely V_p/V_s ratio estimated from time-lapse seismic AVO data is around 7, but this number has a high degree of uncertainty, as indicated by the error bars in Figure 10.

Qualitatively, we find that the simple rock-physics model and the time-lapse seismic measurement both indicate that the V_p/V_s ratio increases with increasing pore pressure. For the Statfjord case, where the vertical differential stress of 6 MPa still is positive in the postinjection phase, the calibrated rock-physics model predicts an increase in the V_p/V_s ratio from ~ 1.9 to ~ 2.0 (Figure 8). This agrees well with the predictions obtained from the time-lapse AVO analysis.

Both field examples used in this study have a measured stress anisotropy where the vertical overburden stresses (σ_v) are greater than the horizontal stresses ($\sigma_H = \sigma_h$). Hence, the differential stresses in the vertical direction are greater than that in the horizontal direction ($\sigma_v' \geq \sigma_h'$). The injection pressure at both fields exceeded their respective horizontal differential stresses ($P_{inj} \geq \sigma_h'$), especially at Gullfaks field. Thus, it is likely that vertical fractures open within the reservoir in the vicinity of the injecting wells.
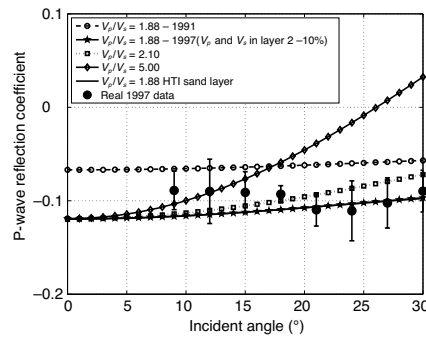

Figure 14. Two-layer Zoeppritz modeling based on average acoustic log values from well A-4 (Table 5) at the Statfjord field. The baseline reflection coefficient (1991) is about half the strength of the monitoring reflection coefficient (1997) with a slight amplitude decrease with angle. For the monitor survey, we have assumed a 10% drop in both V_p and V_s (caused by reduced differential stress), plus various V_p/V_s ratios. The solid circles represent the average amplitude values estimated from 1997 prestack angle gather (Figure 12). The error bars represent the amplitude uncertainty (± one standard deviation). The real data points indicate that the change in V_p/V_s because of pore pressure increase is most likely less than 2.1 when considering the seismic amplitude measurements beyond 15°. The AVO response of the half-space model between an isotropic shale overlying an HTI medium (solid line) simulating a vertically fractured reservoir is more or less identical to the monitor 1 case (star symbol).

Table 5. Seismic parameters used for the half-space seismic modeling of the Statfjord case. The P-wave, S-wave velocity and density values are derived from the logs in well 33/9-A-4. A synthetic shear wave velocity log is used because no S-wave log is acquired for this well. Similar to the Gullfaks case, the P- and S-wave velocities of the monitor 1 case (layer 2) is reduced because of a pore pressure increase by 10%. In the latter two cases, only the S-wave velocities are changed for the given V_p/V_s for layer 2. A fifth half-space model is made by introducing vertical cracks within the reservoir layer with parameters given in Table 6.

	V_p (m/s)	V_s (m/s)	ρ (kg/m³)	V_p/V_s
Layer 1 (Shale)	3157	1635	2436	1.93
Layer 2 (baseline)	3088	1643	2178	1.88
Layer 2 (monitor 1)	2779	1479	2178	1.88
Layer 2 ($V_p/V_s = 2.1$)	2779	1323	2178	2.10
Layer 2 ($V_p/V_s = 5.0$)	2779	556	2178	5.00

In order to model such a fracturing effect seismically, the incident shale and background for the fractured reservoir layers are assumed to be isotropic. Only the presence of fractures within the reservoir layer contributes to the anisotropy of the model examined. This is done by introducing one set of dry penny-shaped vertical fractures in a reservoir sand using Hudson's crack model (Hudson, 1981) to quantify the magnitude of the horizontal transverse anisotropy (HTI). This result is then combined with the Gassmann model to estimate Thomsen's (1986) anisotropy parameters of a fluid-filled vertical fractured sand (see Table 6 and Appendix B for more details).

One of the more difficult parameters to quantify in Hudson's model is the crack or fracture density (ξ_h) and its variation with changing stress conditions. Liu et al. (2002) use a nonlinear crack density-differential stress relation when quantifying the crack-induced seismic anisotropy in terms of Thomsen's anisotropic parameters for different stress paths.

We have chosen to use a simple linear relation between crack density and normalized horizontal differential stress, $(P_{inj} - \sigma_h)/(\sigma_v - \sigma_h)$. This simple model states that increased deviation between pore pressure and horizontal stress leads to a greater crack density (Figure 15). This relationship will probably only be valid up to a certain crack density. Beyond this crack density threshold, the permeability through the fracture network will be high enough that no further pore pressure buildup will occur. Hence, the crack density will stabilize.

Table 6. Seismic parameters of the monitor 1 case are used to estimate the magnitude of the crack-induced anisotropy because of water injection in the Cook and Tarbert reservoirs at Gullfaks and Statfjord, respectively. The crack thickness and diameter come from Rathore et al. (1995). The crack-induced anisotropy is expressed using Thomsen's parameters.

	Monitor 1 case	
Parameters	Gullfaks	Statfjord
V_p (m/s)	2125	2779
V_s (m/s)	1118	1479
ρ (kg/m³)	2100	2178
K_{ma} (GPa)	37	37
G_{ma} (GPa)	44	44
ρ_{ma} (kg/m³)	2650	2650
K_{fl} (GPa)	1.0	2.7
ρ_{fl} (kg/m³)	700	1000
ϕ (fraction)	0.33	0.30
Crack density (ξ_h)	0.078	0.015
Crack diameter a (mm)	5.5	5.5
Crack thickness b (mm)	0.02	0.02
Crack porosity ϕ_c (fraction)	$\sim$ 0.0009	$\sim$ 0.0002
σ_v (MPa)	40	53
σ_h (MPa)	36.5	46
P_{inj} (MPa)	39	47
ϵ^v	−0.15	−0.027
δ^v	−0.15	−0.029
γ	0.11	0.0018

Sanderson and Zhang (2004) analyzed how various fracture networks affected geometrical parameters, such as fracture density, length, and anisotropy. They used numerical modeling to investigate how fracture networks develop because of changes in the differential stress. One scenario focuses on how the fracture density increases with decreasing differential stress. Qualitatively, their results support our simple linear crack density-stress relation. Because the injection pressure at the Gullfaks field exceeds the horizontal differential stress far more than that at the Statfjord field, it may be reasonable to conclude that the crack density would be larger at Gullfaks (as shown in Figure 15). We choose a maximum injection pressure scenario when simulating the impact of fracturing on the P-wave reflectivity.

An approximate P-wave reflection coefficient (equation 7, Rüger, 1997) for an HTI medium is used to simulate the offset or angle-dependent reflectivity of an interface between a shale and a vertically fractured reservoir, as given by

$$R(\phi = 0^0, \theta) \approx \frac{1}{2}\left(\frac{\Delta V_{p\perp}}{\overline{V}_{p\perp}} + \frac{\Delta \rho}{\overline{\rho}}\right) + \frac{1}{2}\left[\frac{\Delta V_{p\perp}}{\overline{V}_{p\perp}}\right.$$
$$\left. - \left(\frac{2\overline{V}_{s\perp}}{V_{p\perp}}\right)^2\left(\frac{\Delta G_\perp}{\overline{G}_\perp} - 2\Delta\gamma\right) + \Delta\delta^{(V)}\right]\sin^2\theta$$
$$+ \frac{1}{2}\left[\frac{\Delta V_{p\perp}}{\overline{V}_{p\perp}} + \Delta\epsilon^{(V)}\right]\sin^2\theta\tan^2\theta, \qquad (7)$$

where Δ indicates a difference and an overbar indicates an average of the corresponding quantity. The $\perp$ symbol denotes vertical bedding direction of the given quantity; ϕ represents the azimuth angle; while θ is the incidence angle; ϵ, γ and δ represents the P-wave anisotropy, S-wave anisotropy, and the relation between vertical velocity to short-offset normal moveout velocity. The superscript (V) denotes that the anisotropy parameter is defined with respect to the vertical symmetry-axis plane.

Figures 10 and 14 show the synthetic AVO curves (solid line) of a vertically fractured sand underneath an isotropic shale with input pa-
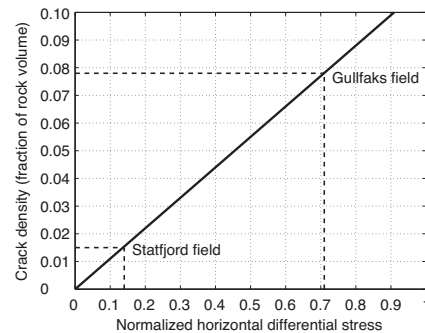

Figure 15. We are assuming a simple relationship between the crack density (ξ_h) and normalized horizontal differential stress, $(P_{inj} - \sigma_h)/(\sigma_v - \sigma_h)$, for both field examples. We have no evidence of field data that supports such a relationship other than numerical modeling of fracture networks done by Sanderson and Zhang (2004). Despite the validity of such a model, we obtain a larger crack density value of the Gullfaks field, which seems reasonable because the injection pressure exceeds further beyond its initial horizontal principal stress (σ_h) than that of the Statfjord field.

rameters as given in Table 6 for the Gullfaks and Statfjord fields. No azimuthal variation of the P-wave reflectivity induced by specific crack orientation is modeled because we assume $\sigma_H = \sigma_h$. This might not necessarily be true because the estimation of the two horizontal stresses are uncertain. We observe that the fracturing does not alter the AVO responses significantly when compared with the isotropic cases (star symbols) for the two field examples.

Larger amplitude changes are predicted for the Gullfaks case when compared with the Statfjord case because the crack-induced anisotropy is larger, Figure 10. The weak AVO changes resulting from fracturing are mainly explained by the fact that δ and γ are roughly the same order of magnitude (δ is one to two times larger than γ) and that the average V_p/V_s ratio across the shale-sand interface is close to 2 (equation 7). Also, ϵ has almost no impact on the AVO response for incidence angles limited to 30°–35°.

For the Statfjord case, it is impossible to relate the predicted V_p/V_s ratio increase to either a pore pressure increase or fracturing because the modeled AVO responses are within the uncertainty of the time-lapse AVO data. However, for the Gullfaks case, it seems more likely that the change in the V_p/V_s ratio is caused by a pore pressure increase instead of fracturing. The seismic modeling representing reservoir fracturing does not explain the amplitude dimming with angle/offset as observed from the seismic field data.

Because most of the analysis in this work is done for areas below the original OWC, one may assume that the observed amplitude effects are caused mainly by the observed pore pressure increase. In this respect, the two data sets analyzed are ideal because we can study the pure pore pressure effect from the time-lapse seismic data.

This study has not investigated possible other effects such as cooling of the reservoir by the water injection and compaction processes. Prior to drawing firm conclusions, establishing similar observations from other fields is necessary, as well as studying other pressure scenarios, such as pressure depletion. The value of knowing the V_p/V_s ratio is significant, both for time-lapse seismic studies and for pore pressure prediction from conventional seismic data. Such observations might provide useful insight into the validity and usefulness of various rock-physics models.

CONCLUSIONS

We demonstrate that it is straightforward to combine the granular H-M model with the Gassmann model in order to estimate the V_p/V_s ratio versus differential stress, when assuming isotropic stress conditions. By using the average number of contacts per grain or coordination number as a calibration parameter in this combined rock-physics model, we estimate the V_p/V_s ratio versus differential stress for two time-lapse seismic case studies from the North Sea. Both case studies represent a significant pore pressure increase (on the order of 5–15 MPa) caused by water injection. However, the end reservoir stress states are quite different for the two cases, as the first example represents near-zero vertical differential stress in the postinjection phase compared with 6 MPa vertical differential stress in the second example.

From the calibration procedure for the two fields, we found significant differences in the estimated coordination number, 6 for Gullfaks and 15 for Statfjord, indicating that Gullfaks is the least consolidated reservoir. A quick comparison of thin sections of the two reservoir sandstones together with static Young's moduli (E_{50}) measurements supports this view.

The calibrated rock-physics model predicted a V_p/V_s ratio increase from ~1.9 to ~2.8 for the Gullfaks example, and a corresponding increase from ~1.9 to ~2.0 of the Statfjord case study. The estimated V_p-V_s ratio increase based on time-lapse AVO analysis is from ~1.9 to ~7 for the Gullfaks field and from ~1.9 to ~2 for the Statfjord field. The uncertainties in the time-lapse AVO estimates are significant; however, both observations indicate an increase in V_p/V_s ratio with increasing pore pressure. The observed increase in the V_p/V_s ratio agrees with many published ultrasonic core measurements. The changes of the V_p/V_s ratio obtained from the Gullfaks 4D seismic data set appear to be more dramatic than the estimates obtained from models and core measurements. The seismically derived velocity ratios appear to be more stress sensitive at very low differential stresses.

The impact of crack-induced anisotropy caused by fracturing is considered through seismic modeling. However, we found that the change in the AVO responses between anisotropic and isotropic cases is minor for the assumed crack densities for the two fields. For the Gullfaks case, it seems more likely that the change in the V_p/V_s is controlled by a pore pressure increase instead of fracturing. We find that the synthetic AVO responses assuming fracturing are opposite of the real time-lapse seismic AVO responses. For the Statfjord case, no AVO differences are seen between an isotropic and a fractured (anisotropic) reservoir sand. Hence, it is impossible to determine whether the predicted V_p/V_s increase results from either a pore pressure buildup, fracturing, or both combined because the synthetic AVO responses are within the uncertainty of the Statfjord 4D seismic AVO data.

APPENDIX A

THE H-M AND GASSMANN MODELS

The H-M model provides an estimate of how the dry frame moduli, K_{dry} and G_{dry}, of granular rocks vary with differential or net stress for a fixed porosity. By combining the H-M with the Gassmann model, an estimate of the effective bulk and shear modulus of a fluid-filled rock can be computed as a function of differential stress.

The Gassmann equations can be expressed as

$$K_{sat} = K_{dry} + \frac{\left(1 - \dfrac{K_{dry}}{K_{ma}}\right)^2}{\dfrac{\phi}{K_{fl}} + \dfrac{1 - \phi}{K_{ma}} - \dfrac{K_{dry}}{K_{ma}^2}}, \tag{A-1}$$

$$G_{sat} = G_{dry}, \tag{A-2}$$

where K_{dry} and G_{dry} represents the effective bulk and shear moduli of a dry porous rock as defined in equations 2 and 3, K_{sat} and G_{sat} are the effective bulk and shear modulus of the fluid-filled rock, and ϕ is the porosity. K_{fl} and K_{ma} represent the effective bulk moduli of the pore fluid and the mineral rock matrix, respectively. K_{fl} is pressure sensitive (Batzle and Wang, 1992), which is taken into account when calculating the effective bulk modulus (K_{sat}) of the rock. K_{ma} is assumed to be pressure independent.

The bulk density (ρ_{sat}) of porous rock is given as

$$\rho_{sat} = (1 - \phi)\rho_{ma} + \phi\rho_{fl}, \qquad (A\text{-}3)$$

where ρ_{ma} represents the effective mineral matrix density, whereas ρ_{fl} is the effective fluid density.

Finally, the isotropic P- and S-wave velocities for a saturated rock (Figure 2) are given by

$$V_{p_{sat}} = \sqrt{\frac{c_{11}}{\rho_{sat}}} = \sqrt{\frac{K_{sat} + \frac{4}{3}G_{sat}}{\rho_{sat}}}, \qquad (A\text{-}4)$$

$$V_{s_{sat}} = \sqrt{\frac{c_{44}}{\rho_{sat}}} = \sqrt{\frac{G_{sat}}{\rho_{sat}}}. \qquad (A\text{-}5)$$

APPENDIX B

CRACK-INDUCED ANISOTROPY MODELING

Assuming an isotropic and homogeneous background material, vertical fractures are introduced using a scattering approach (Hudson, 1981) to estimate the moduli of an elastic solid with fluid-filled thin, penny-shaped circular cracks. The objective is to quantify the contribution of fractures in terms of Thomsen's (1986) anisotropy parameters of a transversely isotropic medium (HTI) with a horizontal axis of symmetry.

The effective stiffness $\mathbf{C}^{dry}$ for the fractured dry rock frame is given as

$$\mathbf{C}^{dry} = \mathbf{C^0} + \mathbf{C^1}, \qquad (B\text{-}1)$$

where $\mathbf{C^0}$ is the stiffness of the isotropic background material and $\mathbf{C^1}$ is the first-order correction resulting from vertical fracturing, hence the crack stiffness.

The dry isotropic moduli components (c_{ij}^0) are determined through inverting equations A-4, A-5, and A-1, resulting in

$$K_{dry} = \frac{K_{ma}\left(\dfrac{K_{sat}}{K_{ma} - K_{sat}} - \dfrac{K_{fl}}{\phi(K_{ma} - K_{fl})}\right)}{1 + \left(\dfrac{K_{sat}}{K_{ma} - K_{sat}} - \dfrac{K_{fl}}{\phi(K_{ma} - K_{fl})}\right)}. \qquad (B\text{-}2)$$

K_{ma}, K_{fl}, K_{sat}, and K_{dry} are the effective bulk moduli of the mineral rock matrix, pore fluid, saturated rock, and dry rock frame, respectively. ϕ represents the porosity of the background material. Because we assume an isotropic background, the medium stiffness is given by

$$\mathbf{C^0} = \begin{bmatrix} c_{11}^0 & c_{12}^0 & c_{12}^0 & 0 & 0 & 0 \\ c_{12}^0 & c_{11}^0 & c_{12}^0 & 0 & 0 & 0 \\ c_{12}^0 & c_{12}^0 & c_{11}^0 & 0 & 0 & 0 \\ 0 & 0 & 0 & c_{44}^0 & 0 & 0 \\ 0 & 0 & 0 & 0 & c_{44}^0 & 0 \\ 0 & 0 & 0 & 0 & 0 & c_{44}^0 \end{bmatrix}, \qquad (B\text{-}3)$$

where

$$c_{11}^0 = c_{22}^0 = c_{33}^0 = K_{dry} + \frac{4}{3}G_{dry},$$

$$c_{12}^0 = c_{11}^0 - 2c_{44}^0 = K_{dry} - \frac{2}{3}G_{dry},$$

$$c_{44}^0 = c_{55}^0 = c_{66}^0 = G_{dry}. \qquad (B\text{-}4)$$

Hudson's inclusion model is used to estimate the dry effective elastic moduli of an isotropic background medium with fractures. The inclusion set introduced is vertical with horizontal crack normal. The first order correction $\mathbf{C^1}$, representing the stiffness of the dry vertical cracks, can then be expressed as an HTI medium given by

$$\mathbf{C^1} = \begin{bmatrix} c_{11}^1 & c_{13}^1 & c_{13}^1 & 0 & 0 & 0 \\ c_{13}^1 & c_{33}^1 & c_{23}^1 & 0 & 0 & 0 \\ c_{13}^1 & c_{23}^1 & c_{33}^1 & 0 & 0 & 0 \\ 0 & 0 & 0 & 0 & 0 & 0 \\ 0 & 0 & 0 & 0 & c_{55}^1 & 0 \\ 0 & 0 & 0 & 0 & 0 & c_{55}^1 \end{bmatrix}, \qquad (B\text{-}5)$$

where

$$c_{11}^1 = -\frac{4}{3}\xi_h\left[\frac{\left(K_{dry} + \frac{4}{3}G_{dry}\right)^3}{G_{dry}\left(K_{dry} + \frac{1}{3}G_{dry}\right)}\right],$$

$$c_{13}^1 = -\frac{4}{3}\xi_h\left[\frac{\left(K_{dry} - \frac{2}{3}G_{dry}\right)\left(K_{dry} + \frac{4}{3}G_{dry}\right)^2}{G_{dry}\left(K_{dry} + \frac{1}{3}G_{dry}\right)}\right],$$

$$c_{33}^1 = -\frac{4}{3}\xi_h\left[\frac{\left(K_{dry} - \frac{2}{3}G_{dry}\right)^2\left(K_{dry} + \frac{4}{3}G_{dry}\right)}{G_{dry}\left(K_{dry} + \frac{1}{3}G_{dry}\right)}\right],$$

$$c_{23}^1 = \left(c_{33}^1 - 2c_{44}^1\right) = c_{33}^1, \quad c_{44}^1 = 0,$$

$$c_{55}^1 = -\frac{16}{3}\xi_h\left[\frac{\left(K_{dry} + \frac{4}{3}G_{dry}\right)}{G_{dry}(3K_{dry} + 2G_{dry})}\right]. \qquad (B\text{-}6)$$

Note that the crack density ξ_h (number of cracks per unit volume) denotes a crack set with horizontal crack normal.

Assuming penny-shaped cracks, the crack porosity ϕ_c is given as

$$\phi_c = \pi \xi_h \left(\frac{b}{a} \right), \tag{B-7}$$

where b/a represents the thickness-diameter ratio of a single crack.

The porosity after fracturing is given as

$$\phi_t = \phi + \phi_c. \tag{B-8}$$

The effective medium stiffness of the dry fractured rock frame ($\mathbf{C}^{dry}$) is derived by adding equations B-3 and B-5,

$$\mathbf{C}^{dry} = \begin{bmatrix} c_{11}^0 + c_{11}^1 & c_{12}^0 + c_{13}^1 & c_{12}^0 + c_{13}^1 & 0 & 0 & 0 \\ c_{12}^0 + c_{13}^1 & c_{11}^0 + c_{33}^1 & c_{12}^0 + c_{33}^1 & 0 & 0 & 0 \\ c_{12}^0 + c_{13}^1 & c_{12}^0 + c_{23}^1 & c_{11}^0 + c_{33}^1 & 0 & 0 & 0 \\ 0 & 0 & 0 & c_{44}^0 & 0 & 0 \\ 0 & 0 & 0 & 0 & c_{44}^0 + c_{55}^1 & 0 \\ 0 & 0 & 0 & 0 & 0 & c_{44}^0 + c_{55}^1 \end{bmatrix}. \tag{B-9}$$

The saturated stiffness moduli components c_{ij}^{sat} are predicted using an anisotropic version of Gassmann's relations (Carcione, 2001) given for $j \geq i$ as

$$c_{ij}^{sat} = c_{ij}^{dry} + M \alpha_i \alpha_j. \tag{B-10}$$

The individual moduli components c_{ij}^{dry} are defined in equation B-9, whereas $\boldsymbol{\alpha}$ and M are given as

$$\boldsymbol{\alpha} = \begin{bmatrix} \alpha_1 \\ \alpha_2 \\ \alpha_3 \\ \alpha_4 \\ \alpha_5 \\ \alpha_6 \end{bmatrix} = \begin{bmatrix} 1 \\ 1 \\ 1 \\ 0 \\ 0 \\ 0 \end{bmatrix} - \frac{1}{3 K_{ma}} \begin{bmatrix} c_{11}^{dry} + c_{12}^{dry} + c_{13}^{dry} \\ c_{12}^{dry} + c_{22}^{dry} + c_{23}^{dry} \\ c_{13}^{dry} + c_{23}^{dry} + c_{33}^{dry} \\ c_{14}^{dry} + c_{24}^{dry} + c_{34}^{dry} \\ c_{15}^{dry} + c_{25}^{dry} + c_{35}^{dry} \\ c_{16}^{dry} + c_{26}^{dry} + c_{36}^{dry} \end{bmatrix}, \tag{B-11}$$

and

$$M = \frac{K_{ma}}{\left(1 - \frac{K^*}{K_{ma}} \right) - \phi_t \left(1 - \frac{K_{ma}}{K_{fl}} \right)}. \tag{B-12}$$

The average bulk moduli of the dry rock frame (K^*) is given as

$$K^* = \frac{1}{9} \left[c_{11}^{dry} + c_{22}^{dry} + c_{33}^{dry} + 2(c_{12}^{dry} + c_{13}^{dry} + c_{23}^{dry}) \right]. \tag{B-13}$$

The effective medium stiffness matrix ($\mathbf{C}^{sat}$) of the water-saturated fractured rock derived from equation B-10 is given as

$$\mathbf{C}^{sat} = \begin{bmatrix} c_{11}^{dry} & c_{13}^{dry} & c_{13}^{dry} & 0 & 0 & 0 \\ c_{13}^{dry} & c_{33}^{dry} & c_{23}^{dry} & 0 & 0 & 0 \\ c_{13}^{dry} & c_{23}^{dry} & c_{33}^{dry} & 0 & 0 & 0 \\ 0 & 0 & 0 & c_{44}^{dry} & 0 & 0 \\ 0 & 0 & 0 & 0 & c_{55}^{dry} & 0 \\ 0 & 0 & 0 & 0 & 0 & c_{55}^{dry} \end{bmatrix}$$

$$+ M \begin{bmatrix} \alpha_1^2 & \alpha_1 \alpha_3 & \alpha_1 \alpha_3 & 0 & 0 & 0 \\ \alpha_1 \alpha_3 & \alpha_3^2 & \alpha_3^2 & 0 & 0 & 0 \\ \alpha_1 \alpha_3 & \alpha_3^2 & \alpha_3^2 & 0 & 0 & 0 \\ 0 & 0 & 0 & 0 & 0 & 0 \\ 0 & 0 & 0 & 0 & 0 & 0 \\ 0 & 0 & 0 & 0 & 0 & 0 \end{bmatrix}. \tag{B-14}$$

The crack-induced anisotropy, assuming vertical fluid-filled cracks, can be quantified for an HTI media using generic Thomsen parameters (Rüger, 1998). These parameters, $\epsilon^{(V)}$, $\delta^{(V)}$, and γ, are related to the saturated stiffness moduli components c_{ij}^{sat} as

$$\epsilon^{(V)} = \frac{c_{11}^{sat} - c_{33}^{sat}}{2 c_{33}^{sat}},$$

$$\delta^{(V)} = \frac{(c_{13}^{sat} + c_{55}^{sat})^2 - (c_{33}^{sat} - c_{55}^{sat})^2}{2 c_{33}^{sat} (c_{33}^{sat} - c_{55}^{sat})},$$

$$\gamma = \frac{c_{44}^{sat} - c_{55}^{sat}}{2 c_{55}^{sat}}. \tag{B-15}$$

where $\epsilon^{(V)}$ and $\delta^{(V)}$ are defined with respect to the vertical symmetry-axis plane, whereas γ is defined with respect to the horizontal symmetry-axis plane.

Numerical estimates of the crack-induced anisotropy are given in Table 6 for the monitor 1 case of the Gullfaks and Statfjord fields.

In both field cases, anisotropic stress conditions exist where the principal vertical stresses are assumed to be larger than the major and minor horizontal principal stresses ($\sigma_v > \sigma_H = \sigma_h$). During pressure maintenance at both fields, the injection pressure (P_{inj}) exceeded the horizontal stresses $P_{inj} \geq \sigma_h$, which may result in opening vertical fractures. Figures 10 and 14 show the AVO response using a weak anisotropic P-wave reflectivity approximation at an interface between an isotropic shale overlying the HTI reservoir sandstone, and Table 6 gives the anisotropy parameters for the two field cases.

REFERENCES

Bachrach, R., J. Dvorkin, and A. M. Nur, 2000, Seismic velocities and Poisson's ratio of shallow unconsolidated sands: Geophysics, **65**, 559–564.

Batzle, M., and Z. Wang, 1992, Seismic properties of pore fluids: Geophysics, **57**, 1396–1408.

Brandt, H., 1955, A study of the speed of sound in porous granular media: Journal of Applied Mechanics, **22**, 479–486.

Capello De P, M. A., and M. Batzle, 1997, Rock physics in seismic monitoring: The Leading Edge, **16**, 1255–1260.

Carcione, J. M., 2001, Wave fields in real media: Wave propagation in anisotropic anelastic and porous media: Pergamon.

Gassmann, F., 1951, Elastic waves through a packing of spheres: Geophys-

ics, **16**, 673–685.

Hesthammer, J., C. A. Jourdan, P. E. Nielsen, T. E. Ekern, and K. A. Gibbons, 1999, A tectonostratigraphic framework for the Statfjord Field, northern North Sea: Petroleum Geoscience, **5**, 241–256.

Hudson, J. A., 1981, Wave speeds and attenuation of elastic waves in material containing cracks: Geophysical Journal of the Royal Astronomical Society, **64**, 133–150.

Huffman, A. R., and J. P. Castagna, 2001, The petrophysical basis for shallow-water flow prediction using multicomponent seismic data: The Leading Edge, **20**, 1030–1052.

Landrø, M., 2001, Discrimination between pressure and fluid saturation changes from time-lapse seismic data: Geophysics, **66**, 836–844.

Landrø, M., P. Digranes, and L. K. Stronen, 2001, Mapping reservoir pressure and saturation changes using seismic methods — Possibilities and limitations: First Break, **19**, 671–677.

Liu, E., S. R. Tod, and X. Y. Li, 2002, Effects of stress and pore fluid pressure on seismic anisotropy in cracked rock: CSEG Recorder, 92–98.

Mavko, G., T. Mukerji, and J. Dvorkin, 1998, The rock physics handbook: Cambridge University Press.

Mindlin, R. D., 1949, Compliance of elastic bodies in contact: Journal of Applied Mechanics, **16**, 259–268.

Nes, O. M., R. M. Holt, and E. Fjaer, 2000, The reliability of core data as input to seismic reservoir monitoring studies: Society of Petroleum Engineering Journal, 65180.

Prasad, M., 2002, Acoustic measurements in unconsolidated sands at low effective pressure and overpressure detection: Geophysics, **67**, 405–412.

Rathore, J. S., E. Fjaer, R. M. Holt, and L. Renlie, 1995, P-wave and S-wave anisotropy of a synthetic sandstone with controlled crack geometry: Geophysical Prospecting, **43**, 711–728.

Rognø, H., K. Duffaut, A. K. Furre, and L. B. Kvamme, 1999, Calibration of time lapse seismic to well and production data — Examples from the Statfjord field: 61st Annual International Meeting, European Society of Geosciences Engineering, Session 5019.

Rüger, A., 1997, P-wave reflection coefficients for transversely isotropic models with vertical and horizontal axis of symmetry: Geophysics, **62**, 713–722.

——, 1998, Variation of P-wave reflectivity with offset and azimuth in anisotropic media: Geophysics, **63**, 935–947.

Sanderson, D. J., and X. Zhang, 2004, The initiation, propagation, and arrest of joints and other fractures: Geological Society of London.

Siggins, A. F., and D. N. Dewhurst, 2003, Saturation, pore pressure and effective stress from sandstone acoustic properties: Geophysical Research Letters, **30**, 1089.

Thomsen, L., 1986, Weak elastic anisotropy: Geophysics, **51**, 1954–1966.

Zimmer, M., M. Prasad, A. Mavko, and A. Nur, 2007, Seismic velocities of unconsolidated sands: Part 1 — Pressure trends from 0.1 to 20 MPa: Geophysics, **72**, no. 1, E1–E13.

2.1   Extended discussion

This section has an extended discussion about assumptions made and results presented in Chapter 2.

The assumption of a 15% P-wave velocity reduction: This is actually more than an assumption; it is justified by the following observations made from both the Gullfaks time-lapse seismic data and core measurements:

- Landrø et al. (2001) observed a time-lapse slowdown of the traveltimes below the reservoir by 4-6 ms. This is a strong indication of a velocity slowdown (reduction of the vertical P-wave velocity within the reservoir). No significant slowdown is observed at the top reservoir, indicating no significant velocity changes in the cap rock.

- In Figure 9 of Chapter 2, a strong increase in the magnitude of the negative reflection coefficient is observed at the top reservoir on the near offset stack. Rock physics measurements from the Gullfaks Field show no significant density changes (Landrø, 2001) when pore pressure is changed, therefore it is reasonable to assume minor density changes. If we assume negligible density changes, this strong increase in the magnitude of the near offset reflection coefficient leads to a significant decrease in the P-wave velocity.

- The dry core measurements shown in Figure 5 of Chapter 2 indicate significant reduction in the P-wave velocity ranging between 10-30% when the pore pressure increases with 5 to 6 MPa.

- We have neglected time-lapse changes in the overburden. If we assume that the pore pressure has increased also in the cap rock, we should expect a velocity slowdown (both in the case of fracturing and pore pressure increase). This implies a reduction in the near offset reflection coefficient, which is opposite of the observed amplitude increase seen in Figure 9. Also note that the overburden stresses will change if the overburden pore pressure change. Above the crest the vertical stress will increase while the horizontal stress will decrease

As stated in our paper the amplitude versus offset (AVO) analysis is associated with uncertainties contributing from the Gullfaks time-lapse seismic data, core data and the underlying assumptions of the AVO modeling. The time-lapse seismic data has been exposed to an industry standard time migration which is likely to improve the signal-to-noise ratio of the data. No particular attempts where made to monitor the AVO variation before and after time migration. We observe significant variation in the root-mean-square

(rms) amplitude level along the target reflector at the Gullfaks Field. This is likely to be due to various propagation and repeatability effects as briefly discussed in Chapter 2. The rms amplitude (a_{rms}) is calculated as

$$a_{rms} = \sqrt{\frac{a^2{}_1 + a^2{}_2 + ... + a^2{}_n}{n}}, \tag{2.1}$$

for all three partial stacks. n represents the number of amplitude samples ($a_1, a_2...$) in the 60 ms time window centered around top reservoir reflector. No azimuthal AVO analysis was performed because the marine surface seismic data do not have the necessary azimuth coverage to allow such analysis. The time-lapse seismic data is acquired in an East-West direction which coincides more or less with the direction of the largest regional horizontal stress (Brudy and Kjørholt, 2001). Hence, the potential fracture pattern across the Gullfaks Field coincides more or less with the acquisition direction of the seismic data. Based on Brudy and Kjørholt (2001) analysis of well data where the horizontal stress condition is $\sigma_H > \sigma_h$ and the modeling work of Alassi et al. (2010), it is reasonable to consider a case where parallel vertical cracks might develop with a preferred orientation in an East-West direction making the initial isotropic Cook sand horizontal transverse isotropic (HTI).

To further explore plausible models explaining the time-lapse seismic AVO data some additional anisotropic model scenarios are made as shown in Table 2.1 and in Figures 2.1 to 2.5. The horizontal and vertical axes of the AVO plots are the same as that of Figure 10 in Chapter 2. Two pairs of shale anisotropy parameters are selected for δ and ϵ based on Wang (2002) and Brevik et al. (2007), whereas anisotropy values of the sand is taken from Thomsen (1995). The P- and S-wave velocities of the sand are reduced with 15% with respect to the in-situ stress conditions (baseline, model 1) due to pore pressure increase and fracturing. In the latter seven cases, only δ and ϵ values are changed due to introduction of horizontal cracks preferably in the sand. The anisotropy values of the VTI shale in the fourth model is doubled with respect to the baseline model simulating also time-lapse changes due to development of horizontal cracks. In the fifth and eighth model scenarios we adjusted the anisotropy parameters (δ and ϵ) of the sand to best fit the Gullfaks time-lapse seismic AVO data. An extreme δ-value is obtained in both cases which in our view is not very realistic. In models six to eight we changed the δ and ϵ values of the shale according to the anisotropy parameter estimation done by Brevik et al. (2007). In the five Figures below the isotropic baseline P-wave reflection coefficient (circle symbol) based on Zoeppritz equation is relatively weak and the absolute amplitude increases with angle. The corresponding baseline reflection coefficient assuming a vertical transverse isotropic (VTI)

shale overlying an isotropic Cook reservoir sand is shown as a black solid line. This is modeled using a VTI P-wave reflection coefficient of Rüger (1997) for a weakly anisotropic medium.

Model	Half-space	V_p(m/s)	V_s(m/s)	ρ(kg/m^3)	V_p/V_s	δ	ϵ
1	Layer1 (baseline shale)	2600	1000	2300	2.6	0.05	0.15
	Layer2 (baseline sand)	2500	1315	2100	1.9	0.00	0.00
2	Layer1 (VTI shale)	2600	1000	2300	2.6	0.05	0.15
	Layer2 (ISO sand)	2125	1118	2100	1.9	0.00	0.00
3	Layer1 (VTI shale)	2600	1000	2300	2.6	0.05	0.15
	Layer2 (VTI sand)	2125	1118	2100	1.9	0.09	0.14
4	Layer1 (VTI shale)	2600	1000	2300	2.6	0.10	0.30
	Layer2 (VTI sand)	2125	1118	2100	1.9	0.09	0.14
5	Layer1 (VTI shale)	2600	1000	2300	2.6	0.05	0.15
	Layer2 (VTI sand)	2125	1118	2100	1.9	0.90	0.30
6	Layer1 (VTI shale)	2600	1000	2300	2.6	-0.07	0.15
	Layer2 (ISO sand)	2125	1118	2100	1.9	0.00	0.00
7	Layer1 (VTI shale)	2600	1000	2300	2.6	-0.07	0.15
	Layer2 (VTI sand)	2125	1118	2100	1.9	0.09	0.14
8	Layer1 (VTI shale)	2600	1000	2300	2.6	-0.07	0.15
	Layer2 (VTI sand)	2125	1118	2100	1.9	0.70	0.50

Table 2.1: Average seismic and anisotropy parameters of shale (layer 1) and sand (layer 2) used for the additional eight Gullfaks half space seismic models.
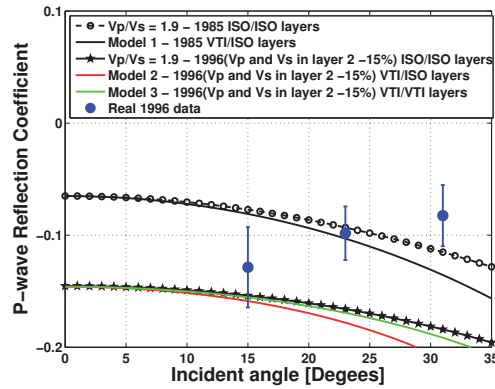
Figure 2.1: Two-layer AVO modeling based on log derived parameters (Table 2.1) for the Gullfaks Field. The red P-wave AVO curve represents a VTI shale overlying a isotropic sand while the green AVO curve simulates a VTI shale overlying a VTI reservoir sand with horizontal cracks. The solid blue circles represents the rms-values (scaled by -0.000015) at the Top Cook reflector of the 1996 near, mid and far offset stacks (Table 2, Chapter 2). The error bars represent ± one standard deviation, based on the variation in the rms-values obtained from averaging 46 cross-line traces.
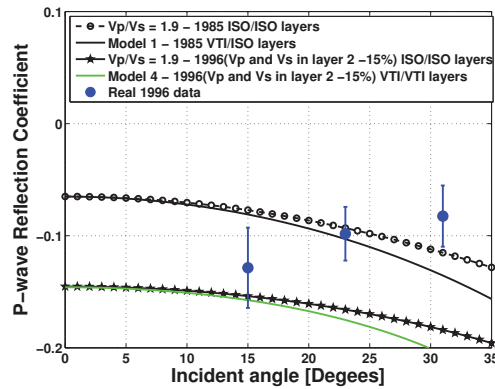

Figure 2.2: Two-layer AVO modeling based on log derived parameters (Table 2.1) for the Gullfaks Field. The green P-wave AVO curve simulates time-lapse changes in the VTI shale through a doubling of the anisotropy values with respect to those of the baseline model due to potential development of horizontal cracks.
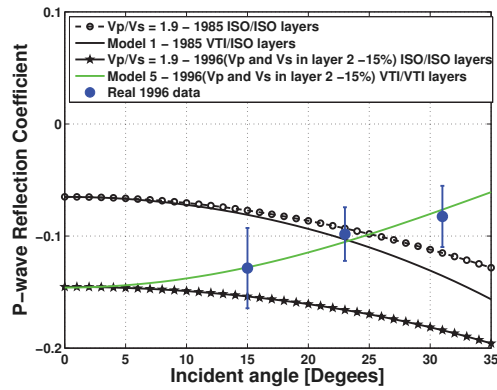
Figure 2.3: Two-layer AVO modeling based on log derived parameters (Table 2.1) for the Gullfaks Field. The green P-wave AVO curve is obtained by adjusting the anisotropy values of the reservoir sand to "best fit" the real 1996 AVO response of the Top Cook reflector.
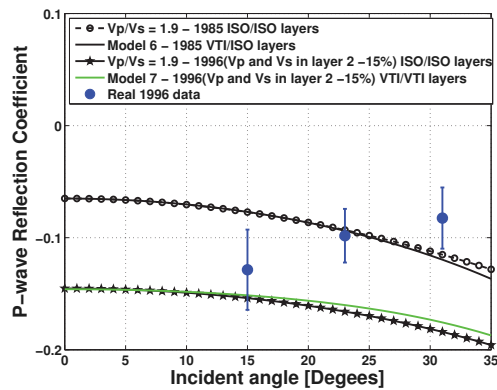

Figure 2.4: Two-layer AVO modeling based on log derived parameters for the Gullfaks Field. The green P-wave AVO curve simulates a VTI shale with a different pair of anisotropy parameters taken from Brevik et al. (2007).
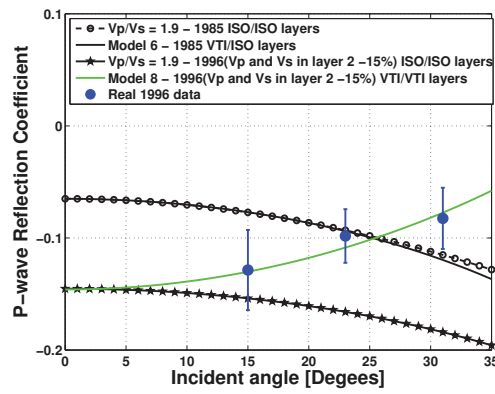
Figure 2.5: Two-layer AVO modeling based on log derived parameters for the Gullfaks Field. The green P-wave AVO curve simulates a VTI shale with a different pair of anisotropy parameters taken from Brevik et al. (2007) and anisotropy values of the reservoir sand obtained by a "best fit" to the real 1996 AVO response of the Top Cook reflector.

The Hudson model (Hudson, 1981) assumes that cracks are isolated with respect to fluid flow. The model assuming cracks filled with weak material is therefore appropriate for high-frequency laboratory conditions and Thomsen (1995) points out that this fails to account for fluid flow between cracks and pores, resulting in significant under-prediction of ϵ. However, Thomsen (1995) also shows comparison of the Thomsen anisotropy predictions from his model with that of Hudson (1981) when assuming a dry porous medium. In this dry case the deviation between the two model-predictions are in order of maximum 10% for the Thomsen δ parameter which is not significant. The approach we follow in Chapter 2 simulates a low-frequency field situation by use of Hudson's dry equations and then saturate the porous medium using an anisotropic version of Gassmann's relation (Carcione, 2001). The Thomsen anisotropy parameters are then calculated from the saturated stiffnesses. Without further comparison of model-predictions we think that our modeling approach may account for the dispersion mechanism.

Chapter 3

Using Mindlin theory to model friction-dependent shear modulus in granular media

Using Mindlin theory to model friction-dependent shear modulus in granular media

Kenneth Duffaut[1,2], Martin Landrø[1], and Roger Sollie[2,3]

ABSTRACT

An explicit expression for the effective shear modulus of a random packing of identical spheres is derived as a function of Mindlin's tangential stiffness with interparticle contact friction. The motivation behind the approach is to incorporate the effect of intergrain friction to predict velocities in unconsolidated sands. The Mindlin friction term, allowing partial slip across the contact area between pairs of spheres, can be viewed as a parameter accounting for the growing macroscopic intergrain friction in sands as burial progresses. Hence, both moduli and velocities will gradually increase as the compressional- to shear-wave velocity ratio (V_P/V_S) or Poisson's ratio (ν) decreases. An estimate of effective elastic constants in particular shear modulus can be obtained for a spherical grain pack with an arbitrary frictional behavior ranging between two special contact boundary conditions representing infinite friction and zero friction. The proposed model predicts a nonlinear transition between the two special grain-contact conditions when compared to previously published linear relationships. Comparison of elastic properties, i.e., dynamic shear-modulus predictions assuming zero contact friction with experimental data on loose glass bead and sand samples undergoing hydrostatic compression, appears to match reasonably well at low confining stress (less than 5 MPa) but deviates gradually as stress increases. It is advocated that the increasing effective internal frictional resistance of the experimental core samples control both the frictional attenuation mechanism in loose grain packs under low confining stress for strain amplitudes typical of seismic waves (less than 10^{-6}) and the higher stress-velocity sensitivity. Circumstantial evidence of this is found in publications describing both laboratory attenuation analysis and consolidation experiments on granular materials with different degrees of competence or static shear strength.

INTRODUCTION

Measured values of Poisson's ratio for dry, clean unconsolidated sand or sandstone are often close to 0.25 or less (Domenico, 1977; Han, 1986; Wang and Nur, 1992; Spencer et al., 1994; Bachrach et al., 2000; Zimmer, 2003). As granular material compacts, the Poisson's ratio diminishes due to rearrangement of particles or grain crushing, which results in a porosity reduction (Gaither, 1953; Magara, 1980; Ramm and Bjørlykke, 1994; Avseth et al., 2001; Chuhan et al., 2002; Zimmer et al., 2002). Often in granular rock-physics analysis, contact models developed by Hertz (1882), Mindlin (1949), Digby (1981), Walton (1987), and Norris and Johnson (1997) are extensively used for two special limits representing either an upper or lower bound for the effective Poisson's ratio of a ran-

domly stacked assembly of identical spheres (Wang and Nur, 1992).

The lower bound, usually referred to as the Hertz-Mindlin model or Walton's "rough-spheres case" (Wang and Nur, 1992; Mavko et al., 1998), assumes no slip across the Hertzian contact area, implying infinite contact friction. The other end limit, Walton's "smooth-sphere case," assumes frictionless contacts and hence zero tangential traction and contact stiffness, allowing slip to occur across the whole contact area. Mindlin (1949) extended his no-slip tangential stiffness solution further, allowing partial slip to occur whenever the tangential force exceeds the interparticle friction force between grains.

To provide a clear understanding of our approach in tying the special limits (Walton, 1987), we review briefly the main derivation of the grain-contact stiffnesses and effective moduli of a random pack-

ing of identical spheres with either infinite friction or zero friction between grains in contact. Thereafter, we derive a new expression for the effective shear modulus combining Digby's result (Digby, 1981) with Mindlin's extended solution (Mindlin, 1949), including frictional tangential contact stiffness. Our approach assumes a uniform stress-strain field applied to the entire pack of spheres composed of identical frictional contacts. This mean strain-field assumption is analogous to that of Digby (1981) and to that of the special bounds given by Walton (1987). The effective shear modulus can be combined with the corresponding bulk modulus to obtain other elastic constants of an isotropic material. Our contact model may be a tool for predicting velocities in unconsolidated sands or sandstone composed of different interparticle bonds or grain-interlocking characteristics. Finally, we compare our modeled dynamic shear modulus and velocities with corresponding data from hydrostatic compression tests on glass beads and sand of Zimmer (2003).

DRY EFFECTIVE BULK AND SHEAR MODULUS OF A RANDOM PACK OF IDENTICAL SPHERES

Digby (1981) solved the problem of the interaction of an assembly of spherical particles that are initially bonded together across small areas by use of elastic contact stiffnesses. He calculated explicitly the dry effective Lamé moduli of a porous granular assembly of identical spheres in contact arranged in a random isotropic packing. Combining equations 33 and 34 of Digby (1981) when assuming either no initial bonding between neighboring particles (circular bonding radius $b = 0$, slip limit) or that the contact radius a is greater than or equal to the bonding radius ($a \geq b$), the effective bulk modulus is given as

$$K_{\text{dry}} = \frac{(1 - \phi)C_p}{12\pi R} S_N, \tag{1}$$

where ϕ is porosity, C_p is the coordination number (average number of contacts per sphere), and R is the sphere radius. The normal stiffness contact, S_N, is given by (Digby, 1981)
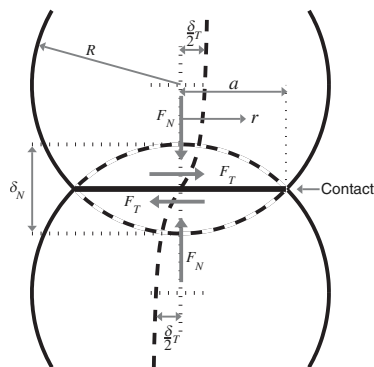

Figure 1. Schematic cross-section view of two identical spheres with radius R undergoing deformation along with contact forces and displacement. The radius of the circular contact area is marked a, and r is the distance from the center of the circle on which the stress acts.

$$S_N = \frac{4Ga}{1 - \nu}, \tag{2}$$

where G and ν are the shear modulus and the Poisson's ratio of the solid spheres, respectively. The corresponding effective shear modulus is given by (Digby, 1981)

$$G_{\text{dry}} = \frac{(1 - \phi)C_p}{20\pi R}\left(S_N + \frac{3}{2}S_T\right), \tag{3}$$

where S_T is the tangential contact stiffness

$$S_T = \frac{8Gb}{2 - \nu}. \tag{4}$$

NO-SLIP LIMIT, INFINITE-CONTACT FRICTION

In this and the following section, we review briefly the main derivation of the effective bulk and shear modulus for two special cases assuming no slip ($a = b$, infinite friction) and slip ($b = 0$, zero friction) inside the contact area between a pair of spheres. We will discuss later how these limits are connected smoothly by including interparticle contact friction.

If two identical elastic spheres are in contact under the action of a normal force F_N, as shown in Figure 1, the Hertz theory (Hertz, 1882) provides a relationship between the circular contact area with radius a and the normal displacement δ_N, given as

$$a \approx \sqrt{\delta_N R} = \left(\frac{3F_N R(1 - \nu)}{8G}\right)^{\frac{1}{3}}. \tag{5}$$

The normal stress distribution as function of distance r from the center of the circle on which the stress acts is (Hertz, 1882)

$$\sigma(r) = \frac{3F_N}{2\pi a^2}\left(1 - \frac{r^2}{a^2}\right)^{\frac{1}{2}}. \tag{6}$$

The maximum contact stress at the center ($r = 0$) is

$$\sigma(r = 0) = \frac{3F_N}{2\pi a^2}, \tag{7}$$

whereas at the edge of the contact area ($r = a$), the normal stress becomes zero. Rearranging equation 5 results in a force-displacement relation that describes normal loading for an elastic contact between two spheres:

$$F_N = \frac{8GR^{\frac{1}{2}}}{3(1 - \nu)}\delta_N^{\frac{3}{2}}. \tag{8}$$

Differentiating equation 8 ($\partial F_N / \partial \delta_N$) yields the normal contact stiffness defined in equation 2.

If a hydrostatic confining pressure P is applied to the solid portion of the random isotropic packing, the confining force F_N acting between pairs of spheres is

$$F_N = \frac{4\pi R^2 P}{C_p(1 - \phi)}. \tag{9}$$

Replacing the normal force in equation 5 with that of equation 9, the radius of the contact area is

$$a = R\left(\frac{3\pi(1-\nu)P}{2C_p(1-\phi)G}\right)^{\frac{1}{3}}. \qquad (10)$$

Inserting equation 10 into equation 2, we find that

$$S_N = R\left(\frac{96\pi G^2 P}{C_p(1-\nu)^2(1-\phi)}\right)^{\frac{1}{3}}. \qquad (11)$$

The dry effective bulk modulus of a random sphere packing is obtained by inserting equation 11 into equation 1:

$$K_{\text{dry}} = \left(\frac{C_p^2(1-\phi)^2 G^2 P}{18\pi^2(1-\nu)^2}\right)^{\frac{1}{3}}. \qquad (12)$$

Equation 12 assumes a hydrostatic stress-strain relationship given by Walton (1987):

$$P = \frac{2C_p(1-\phi)G}{3\pi(1-\nu)}\left(\frac{\epsilon_p}{3}\right)^{\frac{3}{2}}, \qquad (13)$$

where $\epsilon_p/3$ is the average isotropic volumetric strain. Equation 13 can be derived from equations 8 and 9 using that $\epsilon_p/3 = \delta_N/R$.

Mindlin (1949) extended Hertz theory by applying a small tangential force F_T across the circular contact area between two spheres that initially are pressed together by a constant normal force F_N. The tangential force-displacement relation is (Mindlin, 1949)

$$F_T = \frac{4Ga}{(2-\nu)}\delta_T, \qquad (14)$$

where δ_T is the tangential displacement of a sphere center relative to the contact-area center (see Figure 1). For such loading, the distribution of tangential traction or shear stress τ is not constant across the contact area, as shown in Figure 2a, and its intensity is given as (Mindlin, 1949)

$$\tau(r) = \frac{F_T}{2\pi a^2}\left(1 - \frac{r^2}{a^2}\right)^{-\frac{1}{2}}, \qquad (15)$$

where a is given by equation 5 and r is the distance from the center of the circle on which the stress acts. Minimum stress value is at the center ($r = 0$), where

$$\tau(r = 0) = \frac{F_T}{2\pi a^2}. \qquad (16)$$

At the edge of the same contact area ($r = a$), the shear stress becomes infinite, $\tau(r = a) = \infty$. This can occur only if the coefficient of friction is infinite, which implies that there is no partial slip in the contact area. Mindlin (1949) gave the tangential stiffness solution for such a loading and boundary condition as $S_T = 2(\partial F_T/\partial \delta_T)$:

$$S_T = \frac{8Ga}{2-\nu}. \qquad (17)$$

Inserting expressions of the contact radius a and normal and tangential stiffnesses (equations 10, 2, and 17) into equation 3, the effective shear modulus of a random sphere packing is

$$G_{\text{dry}} = \frac{3}{5}\left(\frac{5-4\nu}{2-\nu}\right)K_{\text{dry}}. \qquad (18)$$

Equations 12 and 18 are usually referred to as the standard Hertz-Mindlin model or rough-spheres case (Mavko et al., 1998). Combining these two equations, the dry effective V_P/V_S gives equation 5 of Winkler (1983) when assuming a radius ratio $a/b = 1$:

$$\left(\frac{V_P}{V_S}\right)_{\text{dry}} = \sqrt{\frac{K_{\text{dry}}}{G_{\text{dry}}} + \frac{4}{3}} = \sqrt{\frac{10-7\nu}{5-4\nu}}, \qquad (19)$$

which represents the no-slip limit and hence a lower bound for the velocity ratio of a random sphere packing (Wang and Nur, 1992). The corresponding effective Poisson's ratio is given by (Walton, 1987)

$$\nu_{\text{dry}} = \frac{\nu}{2(5-3\nu)}. \qquad (20)$$

SLIP-LIMIT, ZERO-CONTACT FRICTION

In addition to the previous solution, equations 12 and 18, Walton (1987) derived dry effective bulk and shear moduli, assuming frictionless contacts (perfectly smooth spheres) where the tangential traction and contact stiffness becomes zero ($S_T = 0$) (Figure 2c). Dividing equation 3 by equation 1 when $S_T = 0$ yields (Mavko et al., 1998)

$$G_{\text{dry}} = \frac{3}{5}K_{\text{dry}}. \qquad (21)$$

The effective V_P/V_S for such a contact condition is given by (Walton, 1987)

$$\left(\frac{V_P}{V_S}\right)_{\text{dry}} = \sqrt{3}, \qquad (22)$$

which corresponds to a Poisson's ratio of
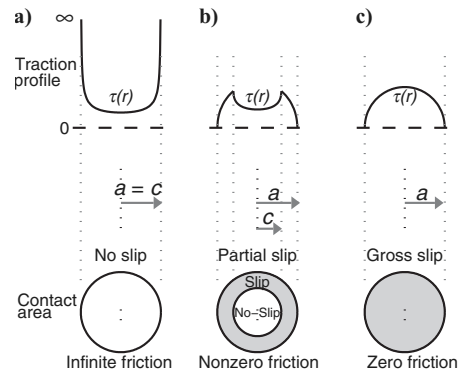
Figure 2. Schematic tangential traction or stress $\tau(r)$ distribution profiles across a contact area between two equal spheres with different boundary conditions. (a) no slip, (b) partial slip, (c) complete or gross slip. Partial slip initiates at the outer radius a (radius of zone with stick-slip motion) of a circular Hertzian contact area and progresses radially inward to c with increasing tangential force F_T, when assuming constant coefficient of friction μ in the contact area, as shown in (b).

$$\nu_{\text{dry}} = \frac{1}{4}. \tag{23}$$

PARTIAL SLIP WITH NONZERO-CONTACT FRICTION

We have reviewed expressions for effective elastic moduli of two special grain-contact conditions of a random packing of identical spheres. In this section, we will derive an expression of the effective shear modulus directly by combining Mindlin's extended tangential contact-stiffness solution assuming finite shear (or tangential) traction at the edge of the contact surface between a pair of identical spheres with the explicit effective modulus expressions derived by Digby (1981). By doing so, we attempt to tie the two special limits (Walton, 1987) by averaging two frictional grain contacts into an arbitrary effective frictional behavior of a granular pack composed of an ensemble of spheres with identical frictional contacts.

Mindlin (1949) introduced frictional contacts assuming partial slip to initiate at the outer radius a of a circular contact area under constant normal force F_N to an inner radius c with monotonically increasing tangential force F_T. Mindlin obtained a distribution of shear traction (stress) assuming a constant friction coefficient μ across the contact surface given by

$$\tau(r) = \begin{cases} \dfrac{3\mu F_N}{2\pi a^2} \sqrt{1 - \dfrac{r^2}{a^2}}, & \text{for } c \leq r \leq a \\ \dfrac{3\mu F_N}{2\pi a^2} \left[\sqrt{1 - \dfrac{r^2}{a^2}} - \dfrac{c}{a} \sqrt{1 - \dfrac{r^2}{c^2}} \right], & \text{for } r \leq c \end{cases} \tag{24}$$

where c is the radius of the central no-slip zone shown in Figure 2b. Furthermore, he showed that the tangential force F_T is obtained by integrating the traction profile over the contact area

$$F_T = \int_0^{2\pi} \int_0^a \tau(r) r \, dr \, d\theta, \tag{25}$$

where r and θ are polar coordinates. This results in equation 101 of Mindlin (1949):

$$c = a \left(1 - \frac{F_T}{\mu F_N} \right)^{\frac{1}{3}}, \tag{26}$$

which gives the circular no-slip zone with radius c as function of contact forces F_T, F_N and the coefficient of static friction μ, whereas a now represents the radius of the contact zone with stick-slip motion (Figure 2b). As F_T approaches μF_N, c approaches zero, and complete sliding occurs (Figure 2c), with a constant tangential force equal to μF_N. Furthermore, Mindlin (1949) assumed that the surface

displacement δ_T within the no-slip zone is uniform everywhere, giving a tangential force-displacement relation as

$$F_T = \mu F_N \left[1 - \left(1 - \frac{16 G a \delta_T}{3(2 - \nu)\mu F_N} \right)^{\frac{3}{2}} \right]. \tag{27}$$

Differentiating equation 27 with respect to the displacement $(\partial F_T/\partial \delta_T)$ yields equation 103 of Mindlin (1949):

$$S_T = \frac{8 G a}{2 - \nu} \left(1 - \frac{F_T}{\mu F_N} \right)^{\frac{1}{3}}. \tag{28}$$

The tangential contact stiffness can now vary nonlinearly with the applied tangential force. Stoll (1989) and Norris and Johnson (1997) extended the tangential contact stiffness given by Mindlin (1949) (equation 28) by accounting for different loading and unloading paths through assuming, after applying a normal force F_{N_0}, that both F_N and F_T are increased at an arbitrary relative rate. Much of their work uses rules established by Mindlin and Deresiewicz (1953) in an exhaustive article of the mechanics near the contact region of two elastic spheres.

We continue with the result and assumptions of Mindlin (1949) by defining $f(\mu) = (1 - F_T/\mu F_N)^{\frac{1}{3}}$ as the Mindlin friction term which reflects the ratio between the stick-slip radii (equation 26) of the grain-contact area (Figure 2b). Inserting expressions of the contact radius a and normal and tangential stiffnesses (equations 10, 2, and 28) into equation 3, the effective shear modulus of a random sphere packing with frictional contacts is

$$G_{\text{dry}} = \frac{3}{5} \left[1 + \frac{3(1 - \nu)}{2 - \nu} f(\mu) \right] K_{\text{dry}}. \tag{29}$$

The ratio $G_{\text{dry}}/K_{\text{dry}}$ monotonically increases with growing stick-slip ratios ($f(\mu)$) and is independent of the confining stress. This elastic-moduli ratio ($G_{\text{dry}}/K_{\text{dry}}$) behavior is similar to that of Magnanimo et al. (2008), although those authors allow variable coordination numbers in their paper.

As will be shown later, the two special limits assuming either complete slip ($f(\mu) \equiv 0, c = 0$) or no slip ($f(\mu) \equiv 1, c = a$) inside the contact area between two spheres are smoothly connected as the Mindlin friction term increases. Furthermore, the dry effective velocity ratio can be expressed as

$$\left(\frac{V_P}{V_S} \right)_{\text{dry}} = \sqrt{\left(\frac{3}{5} \left[1 + \frac{3(1 - \nu)}{2 - \nu} f(\mu) \right] \right)^{-1} + \frac{4}{3}}, \tag{30}$$

whereas the dry effective Poisson's ratio is

$$\nu_{\text{dry}} = \frac{5 - 2\left[1 + \dfrac{3(1 - \nu)}{2 - \nu} f(\mu) \right]}{10 + 2\left[1 + \dfrac{3(1 - \nu)}{2 - \nu} f(\mu) \right]}. \tag{31}$$

In the special case of zero friction representing complete sliding $f(\mu) = 0$ (F_T equal to μF_N), the effective V_P/V_S equals $\sqrt{3}$, corresponding to an effective Poisson's ratio equal to $1/4$, as shown in the previous section, equations 22 and 23 (Walton, 1987). For the limit of infinite friction representing no slip $f(\mu) = 1$ ($F_T/\mu F_N = 0$), we obtain equations 19 and 20.

MODEL VERSUS EXPERIMENTAL DATA

To enable a reasonable comparison between our analytical model and the experimental glass-bead data of Zimmer (2003), we use solid properties for the glass beads reported by Zimmer (2003) and by Sain et al. (2008). The silica glass has matrix density of 2.46 g/cm^3, shear modulus of 29.0 GPa, and a Poisson's ratio of 0.2, which corresponds to a matrix bulk modulus of 38.7 GPa. These values are close to those reported by Spinner (1956), Domenico (1977), Cundall et al. (1989), and Holt et al. (2007). The effective-media theory expressions, equations 1 and 3, assume a random packing of identical spheres with a fixed porosity of 36%. Walton (1987) assumes no new contacts to be made or lost during compression. A random dense packing with 36% porosity corresponds to an average coordination number C_p of 10 to 11, according to Bernal and Mason (1960), which is comparable to the value of nine given by Brandt (1955) and the trend complied by Murphy (1982). The latter trend is estimated with the following function given by Zimmer (2003):

$$C_p = 24e^{(-2.547\phi)} - 0.373. \quad (32)$$

This agrees with the theoretical value of eight to 10 contacts per grain for regular spherical packs of comparable porosity obtained from the extensive work of Graton and Fraser (1935).

On the other hand, Makse et al. (1999) and Duffaut and Landrø (2007) propose a dependence of the coordination number on stress to compensate for modulus or velocity discrepancies between theory and experiments. Granular dynamics simulations of Makse et al. (1999) showed an increase in the average coordination number from six to about seven over a stress range of 0 to 20 MPa, whereas Duffaut and Landrø (2007) estimated for the same stress range a larger increase from six to 15 from dry core measurements. Marvin (1939) observed for the same stress range an average coordination number of about 8.5 from lead-shot compression tests. For lower confining pressure (<1 MPa), Cundall et al. (1989) and Agnolin and Roux (2008) observed from numerical simulations of isotropic assemblies of glass spheres a larger variation in average coordination number with pressure than porosity, some as low as 4.5 to 5.0.

We continue with Walton's assumption (Walton, 1987) and choose a constant coordination number of nine obtained from equation 32 in our modeling. Figure 3a shows the modeled effective shear modulus (equation 29) with increasing confining stress for a discrete set of values of the Mindlin friction term ($f(\mu)$). Figure 3b illustrates the increase in modeled P-wave and S-wave velocity for the same stress range and $f(\mu)$ values.

The dry velocities of the grain pack are given as

$$V_{P_{dry}} = \sqrt{\frac{K_{dry} + \frac{4}{3}G_{dry}}{(1 - \phi)\rho_{ma}}} \quad (33)$$

$$V_{S_{dry}} = \sqrt{\frac{G_{dry}}{(1 - \phi)\rho_{ma}}}, \quad (34)$$

where $V_{P_{dry}}$ and $V_{S_{dry}}$ represent the P-wave and S-wave velocity, respectively, and ρ_{ma} is the matrix density. Correspondingly, shear modulus and dry velocities measured in a consolidation experiment with glass beads by Zimmer (2003) are shown as black circles. Hydrostatic loading from 0.1 to 20 MPa (load cycles 7 and 8) with the largest size of glass beads (called GB Big in Zimmer, 2003) reduces

porosity from 37.6% to 36.2%. There is an observable gradual increasing deviation between both the shear modulus and velocities measured in the glass-beads experiment when compared to the perfect slip model of Walton (1987).

Likewise, a comparison is shown in Figure 4a and b between model and experimental measurements obtained from an almost identical consolidation test of Zimmer (2003) on Santa Cruz aggregate sand (SC Big). This is a quarried beach sand made of sieved fractions of grain sizes between 0.295 and 0.350 mm. The sorting characteristics, mean grain size, coefficient of uniformity, and curvature are the same as those of the glass-bead sample, but the sphericity and roundness characteristics are very different (Figure 2 in Zimmer et al., 2007). The porosity of the Santa Cruz sand sample drops from 39.5% to 37.2% for two load cycles from 0.1 to 20 MPa (cycles 8 and 9), which is slightly higher compared with that of the glass beads.

In addition, the mineral composition is different when comparing solid grains. The Santa Cruz sand sample is composed of multimineral sand grains, whereas the glass beads are 100% silica glass (Zimmer, 2003; Zimmer et al., 2007). The effective solid grain moduli of the Santa Cruz sand that we use for model comparison are estimated by averaging upper and lower Hashin-Shtrikman bounds for multiphase grains given by Berryman (1995). Volumes of solid fractions are taken from Zimmer et al. (2007), and mineral moduli and density values are from Mavko et al. (1998). The effective bulk and shear modulus of the solid sand grains are approximately 39.5 GPa and
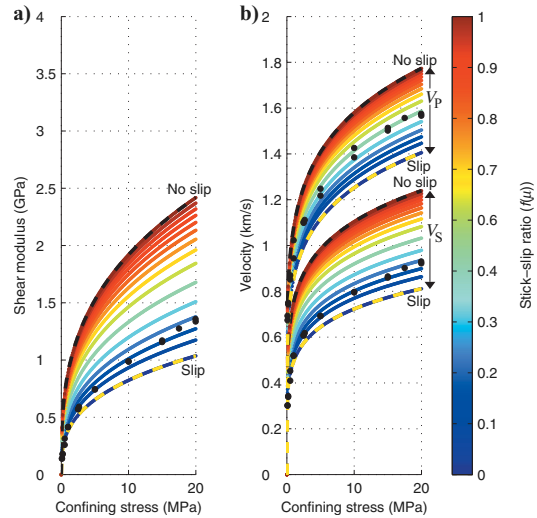

Figure 3. Contact model predictions of (a) effective shear modulus and (b) dry velocities versus hydrostatic confining stress for a discrete set of values of the Mindlin friction term ($f(\mu) = c/a$) when assuming silica glass-matrix properties of $\rho_{ma} = 2.46$ g/cm^3, $G = 29.0$ GPa, and $\nu = 0.20$. The two special limits of Walton (1987), slip and no slip, are shown as dashed lines for both shear modulus and velocities. A rising effective contact friction results in gradually higher shear modulus and hence faster P-wave and S-wave velocities. Correspondingly, shear modulus and dry-velocity measurements from the consolidation test on glass beads (called GB Big in Zimmer, 2003) are shown as black circular symbols for two hydrostatic load cycles (cycles 7 and 8) from 0.1 to 20 MPa.

31.4 GPa, respectively, which corresponds to a Poisson's ratio close to 0.19 and a matrix density of 2.64 g/cm³.

LINEAR VERSUS NONLINEAR FRICTION MODELS

We propose using Mindlin's tangential stiffness solution (Mindlin, 1949), including interparticle contact friction, in combination with Digby's expressions of effective modulus (Digby, 1981) when estimating the shear stiffness of a random pack of identical spheres. This results in a nonlinear relationship that ties Walton's two special cases (Walton, 1987), infinite friction (no slip) and zero grain-contact friction (slip), by allowing partial slip across the contact area between pairs of spheres in a grain pack. We see our approach as analogous to the effective-medium theory associated with granular media, in which two frictional grain contacts were averaged into an arbitrary effective frictional behavior of an ensemble of spheres with many identical frictional contacts.

Jenkins et al. (2005) introduced a linear weight factor α representing the strength of the tranverse stiffness of the grain-to-grain contact tying together the same end-member solutions. Figure 5a shows a comparison of the two models for the dry effective velocity ratio (V_P/V_S) and Poisson's ratio for a solid-grain Poisson's ratio of 0.2.
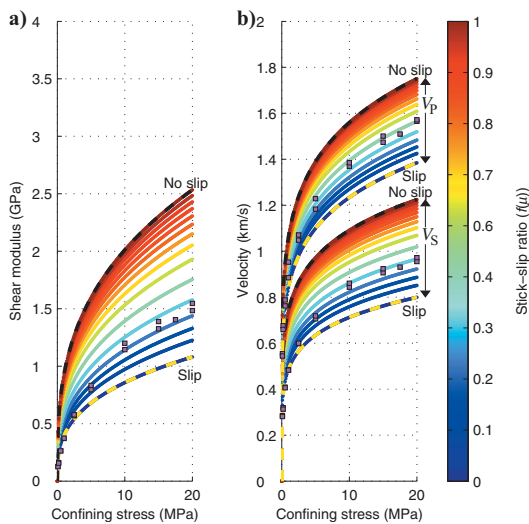

Figure 4. Comparison of contact model predictions of (a) effective shear modulus and (b) dry velocities versus hydrostatic confining stress for a discrete set of values of the Mindlin friction term ($f(\mu)$ = c/a) to the corresponding measurements of load cycles 8 and 9 from the dry Santa Cruz sand (square magenta symbols) of Zimmer (2003). We assume sand-matrix properties of ρ_{ma} = 2.64 g/cm³, G = 31.4 GPa, and ν = 0.19. As in Figure 3, Walton's (Walton, 1987) special limits, slip and no slip, are shown as dashed lines, and color-coded curves predict the magnitude of the shear modulus and P-wave and S-wave velocities with increasing effective contact friction in a stress range from 0.1 to 20 MPa. The sorting characteristics, mean grain size, coefficient of uniformity, and curvature are identical to those of the glass-bead sample (GB Big), but the sphericity and roundness characteristics are very different, and porosity is slightly higher for the sand sample.

The deviation between the effective elastic constants predicted by the models for a given ratio $F_T/\mu F_N$ is caused by areal differences of the no-slip zone, as shown in Figure 5b. Hence, higher velocity ratio or Poisson's ratio values are therefore expected for the Jenkins model because it always predicts a lower stick-slip ratio between the special limits when compared to our model.

Assuming a linear relationship, $\alpha = (1 - F_T/\mu F_N)$, equation 31 becomes

$$\nu_{dry} = \frac{(2 - \nu) - 2\alpha(1 - \nu)}{4(2 - \nu) + 2\alpha(1 - \nu)}, \qquad (35)$$

which is identical to that of Jenkins et al. (2005). This is not based on Mindlin's loading and boundary conditions but is an adjustment of the cube root of $f(\mu)$ (equation 28) to unity. Hence, the no-slip contact area diminishes, causing a reduction in the stick-slip ratio, as shown in Figure 5b. Figure 6a shows the dry effective V_P/V_S and Poisson's ratio as a function of the ratio $F_T/\mu F_N$ with increasing exponent value from zero to one. An exponent equal to zero corresponds to a no-slip situation $f(\mu) = 1$ (radius $c = a$, Figure 2a) for all $F_T/\mu F_N$ ratios, whereas an exponent equal to one results in Jenkins' linear relationship, shown as the dashed line in Figure 6a. Figure 6b highlights the stick-slip ratio as a function of the ratio $F_T/\mu F_N$ with increasing exponent value from zero to one.

Consolidation experiments performed on dry unconsolidated granular samples show a clear reduction of porosity as confining stress increases. However, the rate of porosity reduction diminishes
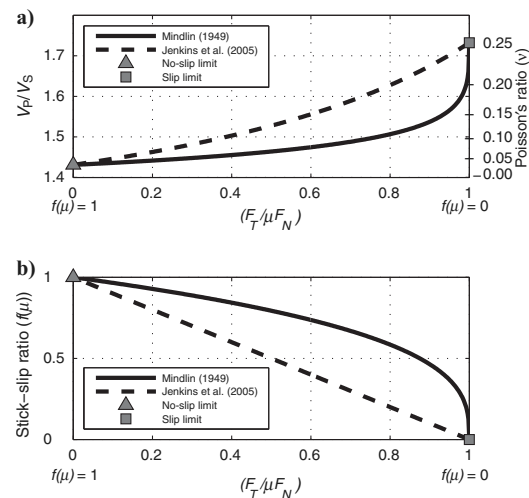

Figure 5. (a) Comparison of the dry effective V_P/V_S and Poisson's ratio versus $F_T/\mu F_N$ of Jenkins et al.'s (2005) model to our model (solid line), including Mindlin's (1949) tangential stiffness with intergrain contact friction. Both models assume a solid-grain Poisson's ratio of 0.2. Jenkins et al.'s (2005) model consistently predicts a higher V_P/V_S and Poisson's ratio except at the end points, when compared to our model (equations 30 and 31). The reason for this deviation is shown in (b), where the Jenkins linear model, for a given $F_T/\mu F_N$, consistently gives a stick-slip ratio ($f(\mu)$) less than the nonlinear Mindlin friction term ($f(\mu)$). The two special bounds of the V_P/V_S or ν_{dry} for a random sphere packing are displayed as a square and a triangle, representing perfect slip and no slip, respectively.

with increasing confining stress (Chuhan et al., 2002; Karner et al., 2003; Zimmer, 2003). With this observation in mind, we prefer the nonlinear stick-slip ratio ($f(\mu)$) given by Mindlin (1949) over that of Jenkins et al. (2005) simply because the rate of grain rearrangement or movement in a granular pack undergoing compression seems to diminish with increasing confining stress. This is due to the increase in the bulk or effective internal frictional resistance of the grain pack as neighboring particles jam and become locked (Yong and Warkentin, 1966; Byerlee, 1978; Anthony and Marone, 2005). Thus, both static and dynamic stiffness and velocities will gradually increase as the corresponding velocity ratio or Poisson's ratio decreases (Hardin and Richart, 1963; Hamilton, 1972; Zimmer, 2003; Fjær, 2009).

Bachrach and Avseth (2008) and Dutta et al. (2009) suggest calibration procedures for an effective granular media by mixing slip and no-slip grain contacts by use of Jenkins' model (Jenkins et al., 2005) to better fit core and log velocity measurements aquired on unconsolidated sediments. Correspondingly, our equation 29 requires either estimates of the Mindlin friction term ($f(\mu)$) to enable predictions of shear modulus and velocities or, alternatively, to invert for $f(\mu)$ from elastic moduli. This can be achieved through equations 29–31, given laboratory or well-log measurements as functions of confining stress. Appendix A outlines different ways to estimate the Mindlin friction term from various elastic and petrophysical measurements.

DISCUSSION

Our model predicts nonlinear behavior in elastic moduli (i.e., K_{dry}; G_{dry}) of a granular assembly of elastic spheres undergoing compaction by allowing partial slip across the contact area between grains. Figure 3a and b shows modeled shear modulus (equation 29) and velocities for growing stick-slip ratios ($f(\mu)$), starting at the perfectly smooth sphere-contact condition (slip) and ending at the no-slip limit. The mineral moduli and petrophysical parameters stated previously for the glass beads are used in the modeling. Each colored curve simulates a constant effective or apparent friction of a random pack of identical spheres over a stress cycle from 0.1 to 20 MPa. A comparison of shear modulus and velocity measurements on a glassbead sample (black circles, Figure 3a and b) made by Zimmer (2003) with the slip model of Walton (1987) appears to match fairly well for confining stress below 5 MPa. At higher stresses, we observe gradually increasing deviation between the glass-bead measurements and Walton's perfect slip model. Apparently, shear modulus and velocity measurements of this sample seem to show a higher stress dependency than predicted by the perfect slip model. This observation is reported by Domenico (1977), Norris and Johnson (1997), and Holt et al. (2007), among others.

We argue that the increasing deviation observed between experimental data of Zimmer (2003) and our model seen in Figure 3a and b can be related to a rising effective internal frictional resistance or shear strength of the glass-bead sample as confining stress increases. Both moduli and velocity measurements of this sample gradually cross the first few color-coded isofrictional grain-contact curves predicted with our model (equation 29). This indicates that the sample may possess a unique effective frictional behavior in the first few stages of the compression test, before the magnitude of the elastic measurements stabilizes or levels out toward the end of the loading cycle. Hence, both shear modulus and velocities appear to be more stress sensitive over the specific stress range than those of our model,

which assumes constant porosity, coordination number, and grain-contact friction.

It is observed that the P-wave velocity of the glass-bead sample follows a different frictional curve, with a higher stick-slip value, than does the shear-wave velocity. This is directly related to an underestimation of the dry effective bulk modulus of the glass-bead sample when using equation 12, which implies that the sample has a dry effective Poisson's ratio greater than Walton's (Walton, 1987) theoretical upper limit of 0.25 (V_P/V_S greater than $\sqrt{3}$). Without further explanation of the bulk-modulus discrepancy, there are some potential sources of error related to loading path, plastic grain deformation, strain anisotropy, and non-Hertzian contact conditions. Pride and Berryman (2009) relate the discrepancy in bulk stiffness between granular experimental measurements and model predictions to "jamming" of loose grains in a pack that creates new stress-bearing contacts. Hence, the elastic stiffness of the grain pack increases.

A further support of a stress-dependent effective internal frictional-resistance mechanism may be seen when comparing dynamic shear modulus and shear-velocity measurements of the Santa Cruz aggregate sand (square magenta symbols, Figure 4a and b) to those of our model when using sand-material properties, as stated previously. This comparison reveals that the stick-slip ratio ($f(\mu)$) of the Santa Cruz sand is about 50% greater than that of the glass-bead sample. We advocate that this is directly related to the angularity of
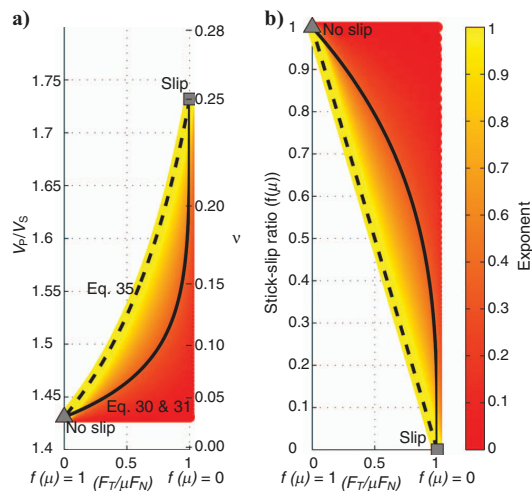

Figure 6. (a) Dry effective V_P/V_S and Poisson's ratio versus $F_T/\mu F_N$ for an increasing magnitude of the exponent of equation 28. Jenkins et al.'s (2005) model is displayed with a dashed line, whereas our model using tangential stiffness with frictional grain contacts described by Mindlin (1949) is shown as a solid line. Both models use a solid-grain Poisson's ratio of 0.2. The two special cases described by Walton (1987) are shown as a square (slip) and a triangle (no slip). Part (b) highlights how the stick-slip ratio ($f(\mu)$) varies as function of $F_T/\mu F_N$ with increasing exponent value from zero to one. Jenkins et al.'s (2005) stick-slip ratio varies linearly with increasing $F_T/\mu F_N$, whereas our model is based on a nonlinear relationship. Jenkins et al.'s (2005) model always predicts a lower stick-slip ratio compared to our model for a given $F_T/\mu F_N$ except at end points. This explains the deviation between the predicted V_P/V_S and Poisson's ratio of the two models.

the sand grains (see Figure 2 of Zimmer et al., 2007). A pack of angular grains possesses a larger effective internal frictional resistance than one composed of perfectly smooth uniform spheres. Hence, both dynamic shear modulus and shear velocity in the sand are therefore larger than those of the glass beads and the model representing perfectly smooth spheres (Hardin and Richart, 1963; Hamilton, 1972).

Note that the sorting characteristics of the Santa Cruz sand are identical to those of the glass-bead sample (Zimmer, 2003; Zimmer et al., 2007). The lower P-wave velocity observed in the sand as compared with that of the glass-bead sample is partly explained through slightly higher porosity in the sand (about a porosity unit higher). It is interesting to note that the P-wave velocity of the sand consistently lies below that of the glass beads across the stress cycle, whereas a crossover is observed for the S-wave velocities of the two samples. It is also worth mentioning that the stick-slip ratios observed for both P-wave and S-wave velocities in the sand are of more comparable magnitude than that of the glass beads.

Other possible sources contributing to the observed elastic-modulus or velocity deviations are differences in initial grain-fabric geometry, stress state, and loading paths between experiments and model. In addition, errors related to coordination number and grain-mineral moduli will affect the magnitude of the effective modulus and velocities of the grain pack and cause a vertical shift, up or down, of the isofrictional curves shown in Figures 3 and 4. The estimated grain-mineral moduli of the Santa Cruz sand is about 5% to 7% greater than those of the glass beads. Hence, the shear-modulus predictions of the sand are shifted vertically upward, and the corresponding curves for the P-wave and S-wave velocities are pushed slightly downward. The latter shift is related mainly to the higher matrix density of the sand. The frictional curves derived with the model parameters assumed in this work indicate that moduli and velocities of both samples are located toward small stick-slip ($f(\mu)$) ratios far from the no-slip limit. A comparison of experimental stress-velocity data of glass beads and loose sand with contact model predictions found in publications (Norris and Johnson, 1997; Zimmer, 2003; Zimmer et al., 2007; Bachrach and Avseth, 2008) agrees with our observation. On the other hand, Holt's (Holt et al., 2007) stress-velocity data of glass beads obtained from a hydrostatic loading test indicate steeper gradients of both P-wave and S-wave velocities between Walton's (Walton, 1987) slip and no-slip limit over a stress range of about 5 to 15 MPa. It is important to bear in mind that these comparisons are also sensitive to the choice of coordination numbers and grain-mineral moduli. Furthermore, we observe higher stress sensitivity in parts of the loading cycle for the shear modulus and shear velocity of the Santa Cruz sand because these are crossing the glass-bead measurements. This crossover occurs even though the porosity of the sand is slightly higher (about 3%) than that of the glass-bead sample. If a porosity correction is applied to the shear measurements, for instance by use of a Reuss model (Zimmer, 2003), the distance relative to those of the glass beads will increase because the porosity is reduced.

Our model is based on Walton's (Walton, 1987) average strain assumption (equation 13), in which each grain contact in an assembly of spheres deflects according to an overall mean strain field applied to the entire pack. It is important to note, however, that the average strain assumption has been questioned by, e.g., Makse et al. (1999), Agnolin and Roux (2008), Magnanimo et al. (2008), and Cundall et al. (1989). Cundall et al. (1989) reveal that the prediction of the bulk modulus is sufficiently accurate but that of the effective shear modu-

lus can be overestimated by as much as a factor of three. Furthermore, Cundall et al. (1989), Makse et al. (1999), and Agnolin and Roux (2008) state that the average strain assumption fails for lower confining pressures (<0.2 MPa) when shear stress is applied due to displacement fluctuations in the presence of packing disorder and force chains. On the other hand, Holt et al. (2007) found a good fit between the stress-strain curve (equation 13) of Walton (1987) with static stress-volumetric strain measurements obtained from glass beads undergoing hydrostatic loading in a triaxial cell. Our comparison of measured volumetric strain data of the entire stress range from 0.1 to 20 MPa (load cycle 7) to volumetric strain calculations using silica glass properties in equation 13 results in an 11.5% lower strain value than that of the glass-bead sample of Zimmer (2003).

In the regime of lower confining stress, below 5 MPa, we interpret the good match between experimental measurements of sand and glass-bead data with the model composed of perfectly smooth spheres to be due to a loose grain packing in which stick-slip motion may occur for small strain amplitudes, typically for seismic waves (less than 10^{-6}). Hence, wave energy is lost in friction, causing strain-dependent attenuation Q^{-1}. Such stick-slip motion may be explained by time-dependent bond formations at asperity junctions, surfaces of cracks, or grain-to-grain contacts during passage of a seismic wave (Walsh, 1966; Gordon and Davis, 1968; Hamilton, 1972; Brunson, 1991). However, friction is a nonlinear process because there is a threshold stress or strain amplitude below which no motion occurs, reducing the impact of frictional attenuation mechanism on seismic waves as the confining stress and static shear strength increase.

Winkler et al. (1979) and Winkler (1983) reject such a nonlinear behavior and friction mechanism for small strain amplitudes typical of seismic waves (less than 10^{-6}) because the tangential force (F_T) will be negligible compared to the frictional force (μF_N) in equation 28. Johnston et al. (1979), however, found that friction of thin cracks and grain boundaries is the dominant attenuation mechanism for consolidated rocks under most stress conditions of the earth. It is fair to add that Winkler et al. (1979) and Johnston et al. (1979) used different experimental setups in their analyses, but both used Berea sandstone of about 22% porosity, which is characterized as a consolidated material with quartz cement (Yin, 1992; Prasad and Manghnani, 1997). Prasad and Meissner (1992) concluded from measurements and modeling of velocities and quality factors (Q) that frictional loss mechanisms in unconsolidated coarse-grained sands must also be considered for amplitude strains less than 10^{-6}.

Tittmann et al. (1981) presented data on the strain-amplitude dependence of shear-wave attenuation (Q_S^{-1}) from two sandstones measured in the 400-Hz frequency range. Their attention focused on interface grain bonding between Berea and Boise sandstones which are similar in composition, porosity, and permeability but differ greatly in degree of competence (see Tittmann et al., 1981, for details). The Berea sandstone is cemented primarily with clays and therefore is relatively weak and friable when compared to the Boise sandstone with its strong, silica-bonded grains. From Figure 1 of Tittmann et al. (1981), Q_S^{-1} measured in the Berea sandstone shows a stronger dependence on strain amplitudes below 10^{-6} than those measured in the Boise sandstone. Hence, it is observed that the onset of the strain-amplitude dependence of the Boise sandstone is shifted toward higher strains. This is also observed, although it is more subtle, when comparing extensional attenuation Q_E^{-1} measurements versus strain amplitude in the Massillon and Berea sandstone of Winkler and Nur (1982). Greater strain-amplitude dependence is ob-

served between strains of 10^{-6} and 10^{-7} for the less cemented or consolidated Massillon sandstone when compared to the Berea sandstone.

In addition, an increasing confining pressure or stress translates the attenuation curves toward lower Q^{-1} values and shifts the onset of strain-amplitude dependence toward higher strain values (Tittmann et al., 1981; Winkler and Nur, 1982). Attenuation is frequency dependent, and therefore the friction loss may have less impact within the seismic frequency range when compared to that obtained, e.g., in the work of Tittmann et al. (1981).

CONCLUSION

An explicit expression for the effective dry shear modulus of a random packing of identical spheres is derived using Mindlin's non-linear tangential contact stiffness. We replace the linear interpolation between complete-slip and no-slip grain contacts by combining Mindlin's nonlinear friction term $f(\mu)$ with an expression of the dry effective shear modulus. This leads to a significant and rapid increase of the shear modulus as the compressional- to shear-wave velocity ratio and Poisson's ratio decrease when compared with a linear model, especially for small effective internal frictional resistance for an ensemble of identical spheres.

Comparison of elastic properties, i.e., our dynamic shear-modulus predictions, with experimental data on loose glass bead and sand samples appears to match reasonably well at low confining stress (less than 5 MPa), but greater deviation is observed with increasing confining stress where both experimental data sets gradually cross the first few isofrictional grain-contact curves predicted by our model. The sand sample, composed of grains of the same size as the glass beads but with greater angularity, has higher dynamic shear modulus and shear velocity, which is best explained by grain interlocking.

We argue that the increasing effective internal frictional resistance of the experimental data samples controls both the frictional attenuation mechanism in loose grain packs under low confining stress for strain amplitudes typical of seismic waves (less than 10^{-6}) and the higher stress-velocity sensitivity. Circumstantial evidence of this is found in publications describing both laboratory attenuation analysis and consolidation experiments on granular materials with different degrees of competence or static shear strength.

Other factors contributing to the observed elastic-modulus and velocity deviation are differences in initial grain-fabric geometry, grain-to-grain contact conditions, stress state, and loading paths between experiments and model predictions. In addition, errors related to coordination number and mineral moduli of the grain material will impact the magnitude of the modeled effective modulus and velocities of the sphere pack.

ACKNOWLEDGMENTS

APPENDIX A

ESTIMATION OF THE MINDLIN FRICTION TERM

Estimates of the Mindlin friction term ($f(\mu)$) or stick-slip ratio can be achieved from core or log data in various ways by using different elastic and petrophysical parameters. When dry effective bulk modulus (K_{dry}) and shear modulus (G_{dry}) measurements are available along with the solid-grain Poisson's ratio (ν), $f(\mu)$ is given as

$$f(\mu) = \frac{1}{3}\left(\frac{2-\nu}{1-\nu}\right)\left(\frac{5}{3}\frac{G_{dry}}{K_{dry}} - 1\right). \qquad \text{(A-1)}$$

The Mindlin friction term as a function of the dry effective V_P/V_S and solid-grain Poisson's ratio is given as

$$f(\mu) = \frac{1}{3}\left(\frac{2-\nu}{1-\nu}\right)\left(\frac{5}{3}\left[\left(\frac{V_P}{V_S}\right)^2_{dry} - \frac{4}{3}\right]^{-1} - 1\right), \qquad \text{(A-2)}$$

whereas as a function of the dry effective Poisson's ratio (ν_{dry}) and solid-grain Poisson's ratio, $f(\mu)$ is

$$f(\mu) = \frac{1}{2}\left(\frac{2-\nu}{1-\nu}\right)\left(\frac{1-4\nu_{dry}}{1+\nu_{dry}}\right). \qquad \text{(A-3)}$$

An alternative approach to estimate values of $f(\mu)$ is from normal stiffness S_N and tangential stiffness S_T obtained from linear inversion of equations 1 and 3. This is given as

$$\begin{bmatrix} S_N \\ S_T \end{bmatrix} = \begin{bmatrix} \dfrac{(1-\phi)C_p}{20\pi R} & \dfrac{3(1-\phi)C_p}{40\pi R} \\ \dfrac{(1-\phi)C_p}{12\pi R} & 0 \end{bmatrix}^{-1} \begin{bmatrix} G_{dry} \\ K_{dry} \end{bmatrix}. \qquad \text{(A-4)}$$

Laboratory or well-log measurements of dry effective bulk modulus, shear modulus, and porosity ϕ as functions of confining stress, in addition to coordination number C_p and grain radius R, are required to solve for the individual contact stiffnesses. Given S_N and S_T in addition to the solid-grain Poisson's ratio, the Mindlin friction can be expressed as

$$f(\mu) = \frac{1}{2}\left(\frac{2-\nu}{1-\nu}\right)\frac{S_T}{S_N}. \qquad \text{(A-5)}$$

The stick-slip ratio expressions ($f(\mu)$) are all functions of the Poisson's ratio of the grain material.

REFERENCES

Agnolin, I., and J. N. Roux, 2008, On the elastic moduli of three-dimensional assemblies of spheres: Characterization and modeling of fluctuations in the particle displacement and rotation: International Journal of Solids and Structures, 45, 1101–1123.
Anthony, J. L., and C. Marone, 2005, Influence of particle characteristics on granular friction: Journal of Geophysical Research, 110, 1–14.
Avseth, P., G. Mavko, J. Dvorkin, and T. Mukerji, 2001, Rock physics and seismic properties of sands and shales as a function of burial depth: 71st Annual International Meeting, SEG, Expanded Abstracts, 1780–1783.
Bachrach, R., and P. Avseth, 2008, Rock physics modeling of unconsolidated sands: Accounting for nonuniform contacts and heterogeneous stress

fields in the effective media approximation with applications to hydrocarbon exploration: Geophysics, **73**, no. 6, E197–E209.

Bachrach, R., J. Dvorkin, and A. M. Nur, 2000, Seismic velocities and Poisson's ratio of shallow unconsolidated sands: Geophysics, **65**, 559–564.

Bernal, J. D., and J. Mason, 1960, Packing of spheres: Co-ordination of randomly packed spheres: Nature, **188**, 910–911.

Berryman, J. G., 1995, Mixture theories for rock properties, *in* T. J. Ahrens, ed., A handbook of physical constants: American Geophysical Union, 205–228.

Brandt, H., 1955, A study of the speed of sound in porous granular media: Journal of Applied Mechanics, **22**, 479–486.

Brunson, B. A., 1991, Shear wave attenuation in unconsolidated laboratory sediments, *in* J. M. Hovem, M. D. Richardson, and R. D. Stoll, eds., Shear waves in marine sediments: Kluwer Academic Publishers, 141–147.

Byerlee, J., 1978, Friction of rocks: Pure and Applied Geophysics, **116**, 615–626.

Chuhan, F. A., A. Kjeldstad, K. Bjørlykke, and K. Høeg, 2002, Porosity loss in sand by grain crushing — Experimental evidence and relevance to reservoir quality: Marine and Petroleum Geology, **19**, 39–53.

Cundall, P. A., J. T. Jenkins, and I. Ishibashi, 1989, Evolution of elastic moduli in a deforming granular material, *in* J. Biarez and R. Gourvès, eds., Powders and grains: Balkema Publishers, 319–322.

Digby, P. J., 1981, The effective elastic moduli of porous granular rocks: Journal of Applied Mechanics, **48**, 803–808.

Domenico, S. N., 1977, Elastic properties of unconsolidated porous sand reservoirs: Geophysics, **42**, 1339–1368.

Duffaut, K., and M. Landrø, 2007, V_P/V_S ratio versus differential stress and rock consolidation — A comparison between rock models and time-lapse AVO data: Geophysics, **72**, no. 5, C81–C94.

Dutta, T., G. Mavko, T. Mukerji, and T. Lane, 2009, Compaction trends for shale and clean sandstone in shallow sediments, Gulf of Mexico: The Leading Edge, **28**, 590–596.

Fjær, E., 2009, Static and dynamic moduli of a weak sandstone: Geophysics, **74**, no. 2, WA103–WA112.

Gaither, A., 1953, A study of porosity and grain relationships in experimental sands: Journal of Sedimentary Research, **23**, 180–195.

Gordon, R. B., and L. A. Davis, 1968, Velocity and attenuation of seismic waves in imperfectly elastic rock: Journal of Geophysical Research, **73**, 3917–3935.

Graton, L. C., and H. J. Fraser, 1935, Systematic packing of spheres: With particular relation to porosity and permeability: Journal of Geology, **43**, 785–909.

Hamilton, E. L., 1972, Compressional-wave attenuation in marine sediments: Geophysics, **37**, 620–646.

Han, D.-H., 1986, Effects of porosity and clay content on acoustic properties of sandstones and unconsolidated sediments: Ph.D. thesis, Stanford University.

Hardin, O., and F. Richart, 1963, Elastic wave velocities in granular soils: Journal of the Soil Mechanics and Foundations Division, American Society of Civil Engineers, **89**, 33–65.

Hertz, H., 1882, Über die Beruhrüng fester elastischer Körper: Journal fur die reine und angewandte Mathematik, **92**, 156–171.

Holt, R. M., L. Li, and J. F. Stenebråten, 2007, Compaction behavior of unbonded granular media: Discrete particle vs. experimental vs. analytical modelling, *in* Proceedings of the First Canada-U.S. Rock Mechanics Symposium, 393–401.

Jenkins, J., D. Johnson, L. La Ragione, and H. Makse, 2005, Fluctuations and the effective moduli of an isotropic, random aggregate of identical, frictionless spheres: Journal of the Mechanics and Physics of Solids, **53**, 197–225.

Johnston, D. H., M. N. Toksöz, and A. Timur, 1979, Attenuation of seismic waves in dry and saturated rocks: II. Mechanisms: Geophysics, **44**, 691–711.

Karner, S. L., F. M. Chester, A. K. Kronenberg, and J. S. Chester, 2003, Subcritical compaction and yielding of granular quartz sand: Tectonophysics, **377**, 357–381.

Magara, K., 1980, Comparison of porosity-depth relationships of shale and sandstone: Journal of Petroleum Geology, **3**, 175–185.

Magnanimo, V., L. La Ragione, J. T. Jenkins, P. Wang, and H. A. Makse, 2008, Characterizing the shear and bulk moduli of an idealized granular material: Europhysics Letters, **81**, 34006–34011.

Makse, H. A., N. Gland, D. L. Johnson, and L. M. Schwartz, 1999, Why effective medium theory fails in granular materials: Physical Review Letters, **83**, 5070–5073.

Marvin, J. W., 1939, The shape of compressed lead shot and its relation to cell shape: American Journal of Botany, **26**, 280–288.

Mavko, G., T. Mukerji, and J. Dvorkin, 1998, The rock physics handbook: Cambridge Unversity Press.

Mindlin, R. D., 1949, Compliance of elastic bodies in contact: Journal of Applied Mechanics, **16**, 259–268.

Mindlin, R. D., and H. Deresiewicz, 1953, Elastic spheres in contact under varying oblique forces: Journal of Applied Mechanics, **20**, 327–344.

Murphy, W. F., 1982, Effects of microstructure and pore fluids on the acoustic properties of granular sedimentary materials: Ph.D. thesis, Stanford University.

Norris, A. N., and D. L. Johnson, 1997, Nonlinear elasticity of granular media: Journal of Applied Mechanics, **64**, 39–49.

Prasad, M., and M. H. Manghnani, 1997, Effects of pore and differential pressure on compressional wave velocity and quality factor in Berea and Michigan sandstones: Geophysics, **62**, 1163–1176.

Prasad, M., and R. Meissner, 1992, Attenuation mechanisms in sands: Laboratory versus theoretical (Biot) data: Geophysics, **57**, 710–719.

Pride, S. R., and J. G. Berryman, 2009, Goddard rattler-jamming mechanism for quantifying pressure dependence of elastic moduli of grain packs: Acta Mechanica, **205**, 185–196.

Ramm, M., and K. Bjørlykke, 1994, Porosity/depth trends in reservoir sandstones: Assessing the quantitative effects of varying pore-pressure, temperature history and mineralogy, Norwegian Shelf data: Clay Minerals, **29**, 475–490.

Sain, R., T. Mukerji, and G. Mavko, 2008, Granular dynamics simulation for estimating elastic properties of loose unconsolidated frictional packs: 78th Annual International Meeting, SEG, Expanded Abstracts, 1825–1829.

Spencer, J. W. Jr., M. E. Cates, and D. D. Thompson, 1994, Frame moduli of unconsolidated sands and sandstones: Geophysics, **59**, 1352–1361.

Spinner, S., 1956, Elastic moduli of glasses at elevated temperatures by a dynamic method: Journal of the American Ceramic Society, **39**, 113–118.

Stoll, R. D., 1989, Stress-induced anisotropy in sediment acoustics: Journal of the Acoustical Society of America, **85**, 702–708.

Tittmann, B. R., M. Abdel-Gawad, C. Salvado, J. Bulau, L. Ahlberg, and T. W. Spencer, 1981, A brief note on the effect of interface bonding on seismic dissipation, *in* Proceedings of the 12th Lunar and Planetary Science Conference, 1737–1745.

Walsh, J. B., 1966, Seismic wave attenuation in rock due to friction: Journal of Geophysical Research, **71**, 2591–2599.

Walton, K., 1987, The effective elastic moduli of a random packing of spheres: Journal of the Mechanics and Physics of Solids, **35**, 213–226.

Wang, Z., and A. Nur, 1992, Elastic wave velocities in porous media: A theoretical recipe, *in* Z. Wang, and A. Nur, eds., Seismic and acoustic velocities in reservoir rocks, v. 2: Theoretical and model studies: SEG Geophysics Reprint Series No. 10, 1–35.

Winkler, K., A. Nur, and M. Gladwin, 1979, Friction and seismic attenuation in rocks: Nature, **277**, 528–531.

Winkler, K. W., 1983, Contact stiffness in granular porous materials: Comparison between theory and experiment: Geophysical Research Letters, **10**, 1073–1076.

Winkler, K. W., and A. Nur, 1982, Seismic attenuation — Effects of pore fluids and frictional sliding: Geophysics, **47**, 1–15.

Yin, H., 1992, Acoustic velocity and attenuation of rocks: Isotropy, intrinsic anisotropy, and stress induced anisotropy: Ph.D. thesis, Stanford University.

Yong, R. N., and B. P. Warkentin, 1966, Introduction to soil behavior: Macmillan.

Zimmer, M., 2003, Seismic velocities in unconsolidated sands: Measurements of pressure, sorting and compaction effects: Ph.D. thesis, Stanford University.

Zimmer, M., M. Prasad, and G. Mavko, 2002, Pressure and porosity influences on V_P-V_S ratio in unconsolidated sands: The Leading Edge, **21**, 178–183.

Zimmer, M., M. Prasad, G. Mavko, and A. Nur, 2007, Seismic velocities of unconsolidated sands: Part 1 — Pressure trends from 0.1 to 20 MPa: Geophysics, **72**, no. 1, E1–E13.

Chapter 4

Modeling stress- and friction-dependent elastic anisotropy in granular media

Kenneth Duffaut[1,2], Martin Landrø[1], Roger Sollie[2,3] and Ørjan Pedersen[2]

[1]*Faculty of Engineering Science and Technology,*
Department of Petroleum Engineering and Applied Geophysics,
Norwegian University of Science and Technology, NTNU, Trondheim,
Norway.

[2]*Statoil Research Centre, Trondheim, Norway.*

[3]*Faculty of Natural Science and Technology,*
Department of Physics,
Norwegian University of Science and Technology, NTNU, Trondheim,
Norway.

Abstract

A random dense packing composed of identical elastic isotropic spheres becomes transversely isotropic under uniaxial strain loading conditions and five elastic moduli are needed to describe the effective medium. Hence, the elastic constants are larger in the direction of the applied stress than that of the perpendicular direction. Several published contact models based on small strain in addition to various loading and grain contact assumptions attempt to predict stress-induced elastic anisotropy. We propose a generalized version of a well accepted contact model by incorporating an arbitrary frictional contact behavior ranging between two special contact boundary conditions representing infinite and near zero friction. New expressions for the five elastic moduli and Thomsen parameters as a function of Mindlin's extended tangential contact stiffness are derived, describing an effective medium based on frictional contacts. Our model predicts a decreasing stress-dependent elastic anisotropy with increasing interparticle contact friction. Anisotropy also depends on the net stress ratio $(K_0^{'})$ through the Mindlin friction term $(f(\mu))$ and the Poisson's ratio of the solid sphere material. Instantaneous elastic anisotropy is predicted by the model as the grain assembly is exposed to uniaxial compression, but it is independent of the applied vertical net stress. The stress-dependent elastic anisotropy is always negative when the applied stress is along the axis of symmetry in the vertical direction. Comparison of P-wave velocity anisotropy predictions assuming variable interparticle contact friction with experimental data on an unconsolidated sand under uniaxial strain loading, appear to fit well and lie between the P-wave velocity anisotropy boundaries representing infinite and near-zero contact friction. The modeling results imply that unconsolidated sands or sandstones under uniaxial strain loading occurring at shallow depths may appear with quite a large stress-induced elastic anisotropy ($>20\%$) which can complicate seismic imaging and amplitude interpretation.

4.1   Introduction

When granular media such as sand or sandstone are exposed to e.g. non-hydrostatic consolidation, stress-dependent elastic anisotropy is likely to develop (Nur and Simmons, 1969; Thomsen, 1986; Yin, 1992; Ruiz, 2003; Sayers, 2005b; Chen et al., 2006; Holt et al., 2007; Sherlock et al., 2007). As an otherwise isotropic granular material undergoes e.g. uniaxial stress loading (vertical net stress > horizontal net stress) elastic anisotropy often develops with the

larger elastic moduli in the direction of the applied stress compared to those in the perpendicular directions. This is referred to as stress-induced or stress-dependent elastic anisotropy. The stress-dependent elastic anisotropy is different from intrinsic anisotropy caused by microstructure within e.g. clay and shales (White et al., 1983; Hornby, 1994; Wang, 2002; Sayers, 2005a; Brevik et al., 2007) in that it will not persist when the stress state changes. Different theoretical approaches exist for modeling stress-induced elastic anisotropy. Some authors tries to mimic rocks composed of microfractures or cracks that close when exposed to non-hydrostatic compression causing directional dependent elastic properties (Walsh, 1965; Nur, 1971; Hudson, 1981; Sayers, 1988; Schwartz et al., 1994; Rathore et al., 1995; Furre, 1997; Shapiro, 2003). The classic contact theory combines assumptions for some special grain contact boundary conditions, infinite or near zero friction, together with various anisotropic stress paths to predict the stress-induced elastic anisotropy (Walton, 1987; Stoll, 1989; Schwartz et al., 1994; Johnson et al., 1998; Sayers, 2002; Bandyopadhyay, 2009).

We briefly review the main results of Walton's uniaxial strain model (Walton, 1987) for the special cases of infinite friction and near zero friction between grains in contact. In addition, we rewrite Walton's elastic moduli expressions as a function of normal and tangential contact stiffnesses given by Digby (1981) in a similar way as Stoll (1989) and Johnson et al. (1998), and give explicit expressions for elastic anisotropy and moduli ratios (e.g. Poisson's ratio) for a transversely isotropic medium with a vertical axis of symmetry (VTI). We derive a generalized model based on Walton (1987) theory connecting the two special contact boundary conditions by incorporating frictional contacts. Explicit expressions for the five new elastic moduli as a function of Mindlin's extended tangential contact stiffness (Mindlin, 1949) are given, describing an effective medium based on frictional grain contacts. Furthermore, these are combined to derive explicit expressions for the Thomsen anisotropy parameters (Thomsen, 1986) that are further used to derive explicit expressions of the shear strength parameters of a granular medium. Finally, we compare our modeled P-wave moduli, P-wave anisotropy and shear strength estimates for a spherical assembly with data from a uniaxial compression test on sand (Ruiz, 2003).

4.2 Dry effective moduli of a random packing of identical spheres undergoing uniaxial compression

Walton (1987) derived explicit expressions for the dry effective elastic moduli for a granular material composed of a random dense packing (porosity $\sim$36%) of equally sized spheres undergoing either hydrostatic confining strain or uniaxial strain. For both loading paths he described the effective medium when the sphere contacts are assumed to be infinitely rough (infinite friction) and perfectly smooth (low finite friction). In the case of uniaxial compression applied in the vertical direction the granular medium becomes transversely isotropic with the axis of symmetry (VTI media) aligned with the vertical strain ($e_3 \neq 0$, $e_1 = e_2 = 0$). In the two following subsections we briefly review the main results of Walton's uniaxial strain model (Walton, 1987) for the special cases of infinite friction and near zero friction between grains in contact. In addition, we rewrite Walton's elastic moduli expressions as a function of normal and tangential contact stiffnesses given by Digby (1981) in a similar way as Stoll (1989) and Johnson et al. (1998), and give explicit expressions for elastic anisotropy, moduli ratios and Poisson's ratios of a VTI medium. We will discuss later how the two limits are connected for a growing interparticle contact friction.

4.2.1 Stress induced elastic anisotropy assuming infinite contact friction (No-slip limit)

Exposing a randomly packed assembly of spheres with infinitely rough grain contacts to a uniaxial strain loading, the effective medium theory of Walton (1987) captures the stress-ratio induced elastic anisotropy in terms of the five independent elastic stiffnesses given as

$$
\begin{aligned}
C_{11}^{\text{dry}} &= 3\alpha + 6\beta, \\
C_{13}^{\text{dry}} &= 2\alpha - 4\beta, \\
C_{33}^{\text{dry}} &= 8\alpha + 8\beta, \\
C_{44}^{\text{dry}} &= 2\alpha + 5\beta, \\
C_{66}^{\text{dry}} &= \alpha + 4\beta,
\end{aligned}
\tag{4.1}
$$

where modified versions of Walton's α and β coefficients can be expressed as (Holt et al., 2007)

$$
\alpha = \frac{(1-\phi)C_p G (e_3)^{\frac{1}{2}}}{16\pi (1-\nu)},
\tag{4.2}
$$

$$\beta = \frac{(1 - \phi)C_p G (e_3)^{\frac{1}{2}}}{16\pi (2 - \nu)}, \tag{4.3}$$

and ν and G are the Poisson's ratio and shear modulus of the solid grains respectively, ϕ is the porosity, and C_p is the average number of contacts per grain. e_3 is the strain in the vertical direction given by (Holt et al., 2007)

$$e_3 = \left[\frac{3\pi(1 - \nu)(2 - \nu)\sigma_3'}{(1 - \phi)C_p G(3 - 2\nu)} \right]^{\frac{2}{3}}, \tag{4.4}$$

where the net vertical stress (overburden stress minus pore pressure) is given by σ_3'. The relation of the vertical strain-horizontal net stress (σ_1') can be expressed as

$$e_3 = \left[\frac{12\pi(1 - \nu)(2 - \nu)\sigma_1'}{(1 - \phi)C_p G\nu} \right]^{\frac{2}{3}}. \tag{4.5}$$

Walton's expression for C_{44}^{dry} in Walton (1987) is incorrect and the corrected expression is given in equation 4.1 above and is pointed out previously by Holt et al. (2007) and Bandyopadhyay (2009).

Inserting equations 4.2 and 4.3 into e.g. the expression for C_{33}^{dry} given in equation 4.1 yields

$$C_{33}^{\text{dry}} = \frac{(1 - \phi)C_p}{16\pi} \left(\frac{8G}{1 - \nu} + \frac{8G}{2 - \nu} \right) (e_3)^{\frac{1}{2}}. \tag{4.6}$$

Walton's starting point are two identical elastic spheres of radius R that are in contact under the action of a normal force F_N where the Hertz theory (Hertz, 1882) provides a relationship between the circular contact area with radius a and the normal displacement δ_N given as

$$a \approx \sqrt{\delta_N R}, \tag{4.7}$$

where he assumes that δ_N is much less R (small strains). Since the sphere assembly is under uniaxial strain loading the vertical or axial strain, e_3, is given as

$$e_3 = \frac{\delta_N}{R}. \tag{4.8}$$

Combining equations 4.7 and 4.8 the vertical strain is directly related to the circular contact radius a

$$(e_3)^{\frac{1}{2}} = \frac{a}{R}. \tag{4.9}$$

Replacing the strain term of equation 4.6 with that of equation 4.9, C_{33}^{dry} is given as

$$C_{33}^{\text{dry}} = \frac{(1-\phi)C_p}{16\pi R}\left(\frac{8Ga}{1-\nu} + \frac{8Ga}{2-\nu}\right).$$ (4.10)

Rewriting C_{33}^{dry} as function of Digby's (Digby, 1981) normal and tangential contact stiffnesses

$$S_N = \frac{4Ga}{1-\nu}, \quad S_T = \frac{8Gb}{2-\nu},$$ (4.11)

for infinite contact friction (circular bonding radius $b=a$) yields

$$C_{33}^{\text{dry}} = \frac{(1-\phi)C_p}{16\pi R}\left(2S_N + S_T\right).$$ (4.12)

Correspondingly, the remaining four elastic stiffnesses of the effective medium under uniaxial compression given in equation 4.1 are derived similarly and given as

$$\begin{aligned}
C_{11}^{\text{dry}} &= \tfrac{3(1-\phi)C_p}{64\pi R}\left(S_N + S_T\right), \\[4pt]
C_{13}^{\text{dry}} &= \tfrac{(1-\phi)C_p}{32\pi R}\left(S_N - S_T\right), \\[4pt]
C_{44}^{\text{dry}} &= \tfrac{(1-\phi)C_p}{128\pi R}\left(4S_N + 5S_T\right), \\[4pt]
C_{66}^{\text{dry}} &= \tfrac{(1-\phi)C_p}{64\pi R}\left(S_N + 2S_T\right).
\end{aligned}$$ (4.13)

Combining the elastic moduli of equations 4.12 and 4.13 the nondimensional Thomsen parameters (Thomsen, 1986) ϵ, γ and δ are

$$\begin{aligned}
\epsilon &= \frac{C_{11}^{\text{dry}} - C_{33}^{\text{dry}}}{2C_{33}^{\text{dry}}} = -\frac{12-7\nu}{16(3-2\nu)}, \\[6pt]
\gamma &= \frac{C_{66}^{\text{dry}} - C_{44}^{\text{dry}}}{2C_{44}^{\text{dry}}} = -\frac{3-2\nu}{2(9-7\nu)}, \\[6pt]
\delta &= \frac{\left(C_{13}^{\text{dry}} + C_{44}^{\text{dry}}\right)^2 - \left(C_{33}^{\text{dry}} - C_{44}^{\text{dry}}\right)^2}{2C_{33}^{\text{dry}}\left(C_{33}^{\text{dry}} - C_{44}^{\text{dry}}\right)} = \frac{(9-5\nu)^2 - 9(5-3\nu)^2}{48(3-2\nu)(5-3\nu)},
\end{aligned}$$ (4.14)

when assuming infinite grain contact friction. Note that we use the weak anisotropy approximation of the δ parameter given by Thomsen (1986) to enable direct comparison with other published work. The dry effective elastic moduli ratio along the axis of symmetry is

$$\left(\frac{C_{33}}{C_{44}}\right)_{\text{dry}} = \frac{8\left(3-2\nu\right)}{\left(9-7\nu\right)},$$ (4.15)

which corresponds to a vertical effective Poisson's ratio given as

$$\nu_0^{\mathrm{dry}} = \frac{\left(\frac{C_{33}}{C_{44}}\right)_{\mathrm{dry}} - 2}{2\left[\left(\frac{C_{33}}{C_{44}}\right)_{\mathrm{dry}} - 1\right]} = \frac{3 + \nu}{15 - 7\nu}. \tag{4.16}$$

Equations 4.15 and 4.16 are different from those derived by Wang and Nur (1992) since they used the expression for C_{44}^{dry} from Walton (1987). The effective elastic moduli ratio perpendicular to the axis of symmetry is

$$\left(\frac{C_{11}}{C_{66}}\right)_{\mathrm{dry}} = \frac{3\,(4 - 3\nu)}{(6 - 5\nu)}, \tag{4.17}$$

while the corresponding dry effective Poisson's ratio is

$$\nu_{\mathrm{hor}}^{\mathrm{dry}} = \frac{\left(\frac{C_{11}}{C_{66}}\right)_{\mathrm{dry}} - 2}{2\left[\left(\frac{C_{11}}{C_{66}}\right)_{\mathrm{dry}} - 1\right]} = \frac{\nu}{2\,(6 - 4\nu)}. \tag{4.18}$$

The subscript "hor" means that the Poisson's ratio is determined from the ratio of the elastic moduli in the horizontal direction normal to the axis of symmetry. All of these effective elastic moduli are valid under the assumption of a horizontal net stress to vertical net stress ratio (K_0') obtained through dividing equation 4.4 by equation 4.5 (Holt et al., 2007)

$$K_0' = \frac{\sigma_1'}{\sigma_3'} = \frac{\nu}{4\,(3 - 2\nu)}. \tag{4.19}$$

4.2.2 Stress induced elastic anisotropy assuming finite contact friction (Slip limit)

In addition, assuming the same loading conditions as that of equation 4.1, Walton (1987) derived similar expressions for the elastic stiffnesses of an effective medium with low frictional grain contacts (perfectly smooth spheres) by setting β to zero. Hence,

$$\begin{aligned}
C_{11}^{\mathrm{dry}} &= 3\alpha, \\
C_{13}^{\mathrm{dry}} &= 2\alpha, \\
C_{33}^{\mathrm{dry}} &= 8\alpha, \\
C_{44}^{\mathrm{dry}} &= 2\alpha, \\
C_{66}^{\mathrm{dry}} &= \alpha,
\end{aligned} \tag{4.20}$$

where α is defined in equation 4.2. The strain, e_3, along the vertical axis of symmetry is now given as (Holt et al., 2007)

$$e_3 = \left[\frac{3\pi(1-\nu)\sigma_3'}{(1-\phi)C_p G} \right]^{\frac{2}{3}}, \tag{4.21}$$

while the vertical strain-horizontal net stress relation is

$$e_3 = \left[\frac{12\pi(1-\nu)\sigma_1'}{(1-\phi)C_p G} \right]^{\frac{2}{3}}. \tag{4.22}$$

Equation 4.20 is equivalent to setting the bonding radius, (Digby, 1981), b, to zero. The tangential contact stiffness then becomes zero ($S_T = 0$) in equations 4.12 and 4.13. Hence, the five elastic stiffnesses in the case of perfectly smooth spheres are

$$C_{11}^{\mathrm{dry}} = \frac{3(1-\phi)C_p}{64\pi R} S_N,$$

$$C_{13}^{\mathrm{dry}} = \frac{(1-\phi)C_p}{32\pi R} S_N,$$

$$C_{33}^{\mathrm{dry}} = \frac{(1-\phi)C_p}{16\pi R} 2S_N, \tag{4.23}$$

$$C_{44}^{\mathrm{dry}} = \frac{(1-\phi)C_p}{128\pi R} 4S_N,$$

$$C_{66}^{\mathrm{dry}} = \frac{(1-\phi)C_p}{64\pi R} S_N.$$

Again, combining the elastic moduli of equation 4.23, the Thomsen parameters (Thomsen, 1986) for the slip limit are constant (Duffaut et al., 2008; Bandyopadhyay, 2009)

$$\epsilon = -\tfrac{5}{16},$$

$$\gamma = -\tfrac{1}{4}, \tag{4.24}$$

$$\delta = -\tfrac{5}{24}.$$

The dry effective elastic moduli ratio along the axis of symmetry is

$$\left(\frac{C_{33}}{C_{44}} \right)_{\mathrm{dry}} = 4, \tag{4.25}$$

which corresponds to an effective Poisson's ratio of

$$\nu_0^{\mathrm{dry}} = \frac{\left(\frac{C_{33}}{C_{44}} \right)_{\mathrm{dry}} - 2}{2\left[\left(\frac{C_{33}}{C_{44}} \right)_{\mathrm{dry}} - 1 \right]} = \frac{1}{3}. \tag{4.26}$$

Correspondingly, the effective elastic moduli ratio perpendicular to the axis of symmetry is

$$\left(\frac{C_{11}}{C_{66}}\right)_{\text{dry}} = 3 \qquad (4.27)$$

which gives an effective Poisson's ratio of

$$\nu_{\text{hor}}^{\text{dry}} = \frac{\left(\frac{C_{11}}{C_{66}}\right)_{\text{dry}} - 2}{2\left[\left(\frac{C_{11}}{C_{66}}\right)_{\text{dry}} - 1\right]} = \frac{1}{4}. \qquad (4.28)$$

All of these effective elastic moduli in the slip limit are valid under the assumption of a K_0'-value obtained through dividing equation 4.21 by equation 4.22 (Holt et al., 2007)

$$K_0' = \frac{1}{4}. \qquad (4.29)$$

4.3 Partial slip with growing contact friction

We have reviewed expressions for effective elastic moduli of two special grain contact conditions of a random packing of identical spheres exposed to uniaxial compression along the axis of symmetry. In this section we use the same approach as that of Duffaut et al. (2010) by incorporating Mindlin's extended tangential contact compliance solution (Mindlin, 1949), assuming finite shear (or tangential) traction at the contact edge between a pair of spheres, to derive expressions of the effective elastic moduli of a medium under uniaxial strain loading. By doing so, we attempt to tie the two special limits given by Walton (1987) through averaging two frictional grain contacts into an arbitrary effective frictional behavior of a granular pack composed of an ensemble of spheres with identical frictional contacts.

Mindlin (1949) introduced frictional contacts assuming partial slip is initiated at the outer radius a of a circular contact area under constant normal force (F_N) to an inner radius c with monotonically increasing tangential force (F_T). Mindlin obtained a distribution of shear traction (stress) assuming a constant friction coefficient (μ) across the contact surface. By integrating the traction profile over the contact area Mindlin (1949) showed that

$$\frac{c}{a} = \left(1 - \frac{F_T}{\mu F_N}\right)^{\frac{1}{3}}, \qquad (4.30)$$

which gives the circular no-slip zone with radius c as function of contact forces F_T, F_N and the coefficient of static friction (μ). a represents now the radius of

the contact zone with stick-slip motion. As F_T approaches μF_N, c approaches zero and complete sliding occurs, with a constant tangential force equal to μF_N. Differentiating the tangential force-displacement relation Mindlin (1949) showed that the tangential contact stiffness is

$$S_T^f = \frac{8Gc}{2-\nu} = \frac{8Ga}{2-\nu}\left(1 - \frac{F_T}{\mu F_N}\right)^{\frac{1}{3}}. \tag{4.31}$$

The tangential contact stiffness can now vary non-linearly with the applied tangential force. Duffaut et al. (2010) defined $f(\mu){=}(1\text{-}F_T/\mu F_N)^{\frac{1}{3}}$ as the Mindlin friction term which reflects the ratio between the stick-slip radii (equation 4.30) of the grain contact area. The tangential contact stiffness can now be expressed as

$$S_T^f = \frac{8Ga}{2-\nu}f(\mu) = S_T f(\mu). \tag{4.32}$$

Replacing the tangential stiffness given by equation 4.11 with that of equation 4.32) in equations 4.12 and 4.13, the effective elastic moduli of a random sphere packing with frictional contacts are

$$C_{11}^{\mathrm{dry}} = \tfrac{3(1-\phi)C_p}{64\pi R}\left[S_N + S_T f(\mu)\right],$$

$$C_{13}^{\mathrm{dry}} = \tfrac{(1-\phi)C_p}{32\pi R}\left[S_N - S_T f(\mu)\right],$$

$$C_{33}^{\mathrm{dry}} = \tfrac{(1-\phi)C_p}{16\pi R}\left[2S_N + S_T f(\mu)\right], \tag{4.33}$$

$$C_{44}^{\mathrm{dry}} = \tfrac{(1-\phi)C_p}{128\pi R}\left[4S_N + 5S_T f(\mu)\right],$$

$$C_{66}^{\mathrm{dry}} = \tfrac{(1-\phi)C_p}{64\pi R}\left[S_N + 2S_T f(\mu)\right].$$

The two special limits assuming either slip ($f(\mu) \equiv 0$, $c{=}0$) or no slip ($f(\mu) \equiv 1$, $c = a$) inside the contact area between two spheres are smoothly connected as the Mindlin friction term increases. Furthermore, combining these elastic moduli expressions of equation 4.33, the Thomsen parameters become

$$\epsilon = -\frac{\left(5+2\frac{(1-\nu)}{(2-\nu)}f(\mu)\right)}{16\left(1+\frac{(1-\nu)}{(2-\nu)}f(\mu)\right)},$$

$$\gamma = -\frac{\left(1+\frac{(1-\nu)}{(2-\nu)}f(\mu)\right)}{2\left(2+5\frac{(1-\nu)}{(2-\nu)}f(\mu)\right)}, \tag{4.34}$$

$$\delta = -\frac{9\left(2+\frac{(1-\nu)}{(2-\nu)}f(\mu)\right)^2-\left(4+\frac{(1-\nu)}{(2-\nu)}f(\mu)\right)^2}{48\left(1+\frac{(1-\nu)}{(2-\nu)}f(\mu)\right)\left(2+\frac{(1-\nu)}{(2-\nu)}f(\mu)\right)}.$$

In the special case of complete sliding $f(\mu){=}0$ (F_T equal to μF_N), the Thomsen parameters becomes those of equation 4.24. For the limit of infinite friction representing no-slip $f(\mu){=}1$ ($F_T/\mu F_N = 0$), we obtain equation 4.14.

The dry effective elastic moduli ratio along the axis of symmetry is

$$\left(\frac{C_{33}}{C_{44}}\right)_{\text{dry}} = \frac{8\left(1 + \frac{(1-\nu)}{(2-\nu)}f(\mu)\right)}{\left(2 + 5\frac{(1-\nu)}{(2-\nu)}f(\mu)\right)}, \tag{4.35}$$

which corresponds to a effective Poisson's ratio

$$\nu_0^{\text{dry}} = \frac{\left(\frac{C_{33}}{C_{44}}\right)_{\text{dry}} - 2}{2\left[\left(\frac{C_{33}}{C_{44}}\right)_{\text{dry}} - 1\right]}. \tag{4.36}$$

The effective elastic moduli ratio perpendicular to the axis of symmetry is

$$\left(\frac{C_{11}}{C_{66}}\right)_{\text{dry}} = \frac{3\left(1 + 2\frac{(1-\nu)}{(2-\nu)}f(\mu)\right)}{\left(1 + 4\frac{(1-\nu)}{(2-\nu)}f(\mu)\right)}, \tag{4.37}$$

while the corresponding dry effective Poisson's ratio is

$$\nu_{\text{hor}}^{\text{dry}} = \frac{\left(\frac{C_{11}}{C_{66}}\right)_{\text{dry}} - 2}{2\left[\left(\frac{C_{11}}{C_{66}}\right)_{\text{dry}} - 1\right]}. \tag{4.38}$$

In the two special limits assuming either slip ($f(\mu) \equiv 0$, c=0) or no slip ($f(\mu) \equiv 1$, $c = a$), equations 4.35 through to 4.38 correspond to those equations given in the two previous subsections. All of these effective elastic moduli and ratios in equations 4.33 through 4.38 are valid under the assumptions of a horizontal net stress to vertical net stress ratio ranging between $0 \leq K_0' \leq 1/4$ and $f(\mu)$ between zero and one.

4.4   Estimating the shear strength of granular media from velocity anisotropy and net stress-ratio

In the previous section we derived explicit expressions for the five elastic moduli as a function of the Mindlin friction term ($f(\mu)$), equation 4.30) connecting the two special boundary conditions of Walton (1987) which represent no slip

and slip for uniaxial loading conditions. The Mindlin friction term, allowing partial slip across the contact area between pairs of spheres, attempts to incorporate the effect of growing interparticle contact friction within the sphere pack. Assuming the capacity of the pack of spheres resistance to shear stresses, or shear strength, originate from frictional resistance at interparticle contacts we will derive explicit expressions of mobilized friction and mobilized friction angle from velocity anisotropy and the net stress ratio (K_0'). The maximum or peak friction angle of the sphere pack is later determined from the mobilized friction angle. The coefficient of static friction can be obtained by rearranging the Mindlin friction term. Thus, from equation 4.30, assuming $f(\mu)$ equal c/a

$$\mu = \frac{-\frac{F_T}{F_N}}{\left[(f(\mu))^3 - 1\right]}, \qquad (4.39)$$

where the tangential-normal force ratio (F_T/F_N) can be expressed in terms of shear and normal stresses by multiplying by the actual contact area A such that

$$\frac{AF_T}{AF_N} = \frac{\tau}{\sigma_3'}, \qquad (4.40)$$

where we assume the same contact area for the applied tangential and normal force. Using the Mohr-Coulomb envelope (Janbu, 1985; Budhu, 2007) the stress ratio can be written as

$$\frac{\tau}{\sigma_3'} = \frac{\sigma_3' - \sigma_1'}{2\sigma_3'} = \frac{\sigma_3' - K_0'\sigma_3'}{2\sigma_3'} = \frac{1 - K_0'}{2}. \qquad (4.41)$$

Inserting equation 4.41 into equation 4.39, we redefine μ as the mobilized coefficient of friction at a given stress state

$$\mu_{\mathrm{mob}} = \frac{-\left(1 - K_0'\right)}{2\left[(f(\mu_{\mathrm{mob}}))^3 - 1\right]}. \qquad (4.42)$$

In the no slip limit, $f(\mu_{\mathrm{mob}})$ equals one which leads to infinite contact friction while for the slip limit $f(\mu_{\mathrm{mob}})$ is zero and K_0' equals $\frac{1}{4}$ resulting in a finite contact friction of 3/8 or 0.375. Given the value of the Mindlin friction term $(f(\mu))$ the mobilized coefficient of friction can determined at a given equilibrium state of stress for a K_0' ranging between zero and 1/4. Rewriting equation 4.34, $f(\mu_{\mathrm{mob}})$ can be expressed as function of any of the Thomsen parameters

as

$$f(\mu_{\mathrm{mob}}) = -\frac{(2-\nu)}{(1-\nu)}\frac{(5+16\epsilon)}{(2+16\epsilon)},$$

$$f(\mu_{\mathrm{mob}}) = -\frac{(2-\nu)}{(1-\nu)}\frac{(1+4\gamma)}{(1+10\gamma)}, \tag{4.43}$$

$$f(\mu_{\mathrm{mob}}) = -\frac{(2-\nu)}{(1-\nu)}\left[\frac{(7+36\delta)\pm\sqrt{(7+36\delta)^2-8(1+6\delta)(5+24\delta)}}{4(1+6\delta)}\right].$$

The Mindlin friction term ($f(\mu_{\mathrm{mob}})$) expressed as function of δ is a second-degree equation with two solutions. Inserting a δ equal to -5/24, corresponding to the slip limit (equation 4.24) yields, $f(\mu_{\mathrm{mob}}) \equiv 0$, when choosing the solution with the minus sign. The mobilized friction angle (ρ) at a given stress state is (Janbu, 1985)

$$\rho = \tan^{-1}\left(\mu_{\mathrm{mob}}\right), \tag{4.44}$$

wherein ρ for the two special contact boundary conditions equals 90° at the no-slip limit and approximately 21° at the slip limit. Finally, the relation between the mobilized friction angle and the peak friction angle (ϕ_{peak}) is (Janbu, 1985)

$$\phi_{\mathrm{peak}} = \tan^{-1}\left(\frac{\tan\left(\rho\right)}{f_{\mathrm{shear}}}\right), \tag{4.45}$$

wherein f_{shear} is the degree of shear mobilization with values ranging between 0.6 and 0.7 (Janbu, 1985). At failure, f_{shear} equals one. Hence, ϕ_{peak} equals ρ.

4.5 Model versus experimental data

Figure 4.1 shows a comparison of the horizontal-vertical net stress relation given by Walton's model (Walton, 1987) for two special grain contact conditions, infinite and near-zero friction, against experimental data of Ruiz (2003) on Santa Cruz sand (called SCS in Ruiz (2003)) exposed to uniaxial strain loading. This is a quarried beach sand with porosity of 45%, grain density of 2.606 g/cm^3, and a mean grain size of 0.25 mm (Ruiz, 2003). The loading path of the experimental data is close to linear and falls well inside the upper and lower boundaries defined by Walton's model. Assuming a representative Poisson's ratio of 0.19 for the solid sand grains (Duffaut et al., 2010), the K_0'-value of the loading path is calculated using equation 4.19 for infinite contact friction. These linear loading paths shown in Figure 4.1 transform into constant K_0'-values as shown in Figure 4.2. The upper and lower boundaries displayed as yellow and black lines resepectively are calculated from equations 4.29 and 4.19 when assuming a solid grain Poisson's ratio as given previously.
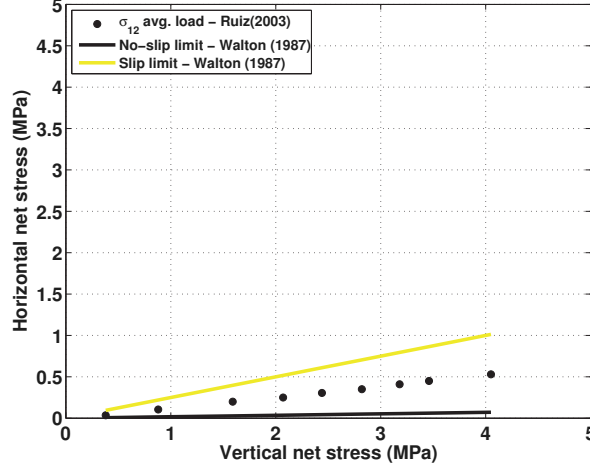
Figure 4.1: Horizontal net stress ($\sigma_1^{'}$) versus vertical net stress ($\sigma_3^{'}$) relation assuming uniaxial strain loading for the two special cases of Walton (1987), slip (equation 4.29) and no slip (equation 4.19). These are shown as yellow and black lines respectively. A solid grain Poisson's ratio of 0.19 (Duffaut et al., 2010) is used to model the $K_0^{'}$ value in the no slip limit. Experimental stress measurements of Ruiz (2003) on dry Santa Cruz sand undergoing comparable uniaxial strain loading tests are shown as black solid circular symbols for one vertical load cycle between approximately 0.4 to 4 MPa. The horizontal net stress displayed for the sand data represents an average of the two horizontal net stresses ($\sigma_1^{'}$) and ($\sigma_2^{'}$).

The corresponding average $K_0^{'}$-value of the Santa Cruz sand is approximatly 0.12.

The corresponding stress-induced anisotropic P-wave velocities assuming a VTI medium, are

$$V_{p33}^{\mathrm{dry}} = V_{p0}^{\mathrm{dry}} = \sqrt{\frac{C_{33}^{\mathrm{dry}}}{(1-\phi)\rho_{ma}}}, \tag{4.46}$$

$$V_{p11}^{\mathrm{dry}} = V_{p_{hor}}^{\mathrm{dry}} = \sqrt{\frac{C_{11}^{\mathrm{dry}}}{(1-\phi)\rho_{ma}}}, \tag{4.47}$$

where V_{p33}^{dry} and V_{p11}^{dry} are the vertical and horizontal P-wave velocities respectively, and ρ_{ma} is the solid grain density. Figure 4.3 shows a comparison between modeled vertical and horizontal P-wave velocities of the slip (yellow lines) and no-slip (black lines) limits of Walton (1987) assuming sand grain density of 2.606 g/cm^3 (Ruiz, 2003), shear modulus, G, of 31.4 GPa, and a Poisson's ratio of 0.19 (Duffaut et al., 2010), with the corresponding dry verti-
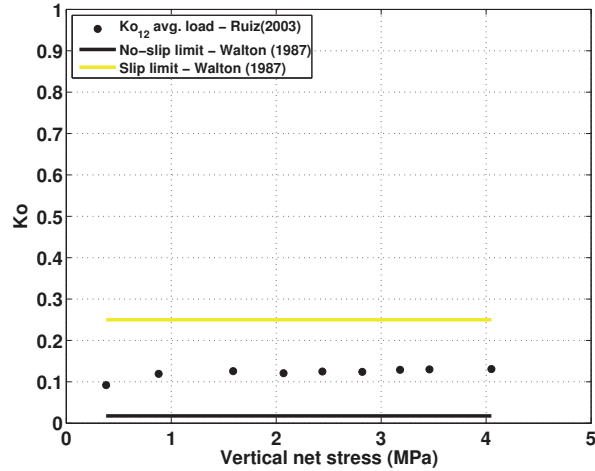
Figure 4.2: Horizontal-vertical net stress ratio $(K_0^{'})$ versus vertical net stress $(\sigma_3^{'})$ assuming uniaxial strain loading. A comparison of Walton's model, for the same two special grain contact limits as shown in Figure 4.1, with the experimental stress measurements of Ruiz (2003) on dry Santa Cruz sand. Horizontal-vertical net stress ratio displayed for the sand data represents an average of the two horizontal net stresses $(\sigma_1^{'})$ and $(\sigma_2^{'})$.

cal and horizontal P-wave velocity measurements from a uniaxial consolidation test performed by Ruiz (2003) on Santa Cruz sand. All the P-wave velocity predictions made with Walton's model for the slip and no slip limits are too high with respect to the experimental velocity measurements of the Santa Cruz sand. This velocity deviation is most probably explained by the higher porosity of the sand sample (nine porosity units) when compared with that assumed for Walton's contact model. The effective-medium theory of Walton (1987), equations 4.12, 4.13 and 4.23, assumes a random dense packing of identical spheres with a fixed porosity of $\approx 36\%$. Walton (1987) assumed no new contacts are made or lost during compression. A random dense packing with $\approx 36\%$ porosity corresponds to an average coordination number (C_p) of about nine (Brandt, 1955; Murphy III, 1982; Zimmer, 2003). These numbers are used in our P-wave velocity modeling as shown in Figure 4.3. A comparison of the stress- and friction-dependent P-wave anisotropy parameter $(\epsilon$, equation 4.34) is shown in Figure 4.4 with increasing vertical net stress for a discrete set of values of the Mindlin friction term $(f(\mu))$, with the corresponding ϵ-values calculated from the uniaxial compression test on Santa Cruz sand (Ruiz, 2003). A more or less constant $K_0^{'}$-value of the experimental consolidation test falls well inside the upper and lower boundaries defined by Walton's model in the
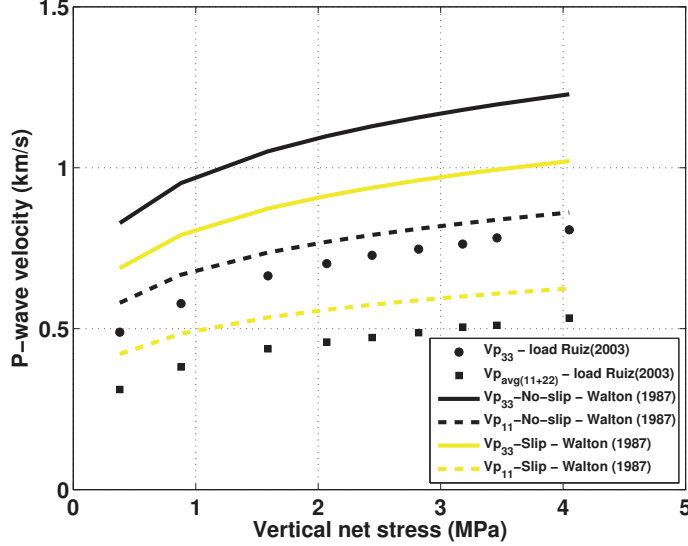
Figure 4.3: Dry vertical ($V_{p_{33}}$) and horizontal velocities ($V_{p_{11}}$) versus vertical net stress modeled for the two special contact conditions (Walton, 1987), slip ($f(\mu) \equiv 0$, yellow lines) and no-slip ($f(\mu) \equiv 1$, black lines) when assuming solid sand grain properties of $\rho_{ma} = 2.606$ g/cm^3, G = 31.4 GPa and $\nu = 0.19$ (Duffaut et al., 2010). A change in the effective contact friction from slip to no-slip results in faster P-wave velocities in both vertical and horizontal directions. Correspondingly, dry vertical and horizontal P-wave velocity measurements from a uniaxial strain loading test on Santa Cruz sand (SCS in Ruiz (2003)) are shown as black circle and square symbols respectively, for one load cycle from 0.4 to 4 MPa.

stress space (Figure 4.2). The ϵ-values obtained for the sand are nicely located inside the theoretical P-wave anisotropic limits predicted for the slip and no-slip boundary conditions of Walton (1987) given by equations 4.24 and 4.14. The anisotropy derived from the P-wave velocity measurements in the sand are nearly constant and slightly larger than -0.3. It is worth to note that our model, equation 4.34, predicts a reduction of the P-wave anisotropy as the effective contact friction increases. Furthermore, Figures 4.5 through 4.8 show comparison of model-predictions of shear-strength related parameters defined previously, the Mindlin friction term ($f(\mu_{\mathrm{mob}})$), mobilized friction (μ_{mob}), mobilized friction angle (ρ), and maximum or peak friction angle (ϕ_{peak}) of a random dense packing of equal spheres when assuming a solid grain Poisson's ratio of 0.19 (Duffaut et al., 2010; Ruiz, 2003; Zimmer, 2003) with experimental data on Santa Cruz sand. It is satisfactory to note that all four parameter estimates, $f(\mu_{\mathrm{mob}})$, μ_{mob}, ρ and ϕ_{peak} obtained from multi-directional P-wave
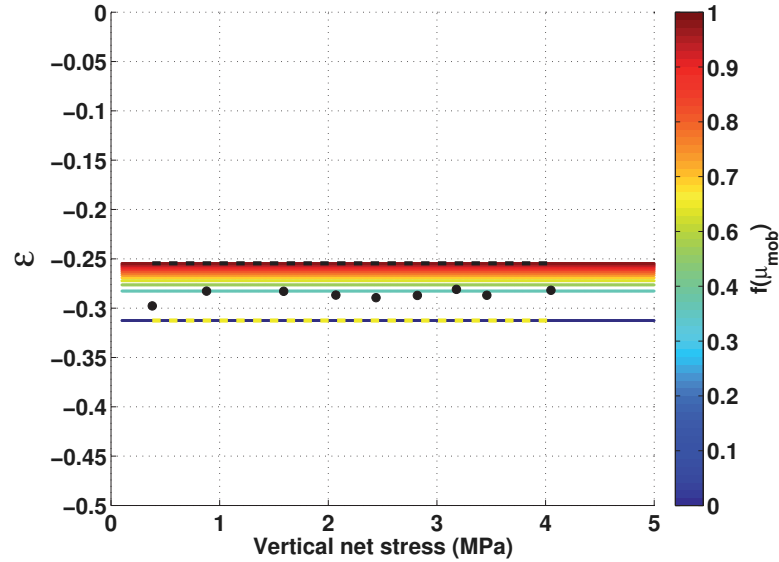
Figure 4.4: Dry P-wave velocity anisotropy (ϵ, equation 4.34) versus applied vertical net stress (σ_3') for a discrete set of values of the Mindlin friction term assuming a Poisson's ratio of 0.19 (Duffaut et al., 2010; Ruiz, 2003; Zimmer, 2003). The two special limits of Walton (1987), slip (yellow) and no-slip (black), are shown as dashed lines. A rising effective contact friction results in gradually decreasing P-wave anisotropy. The ϵ-values calculated from multi-directional P-wave velocity measurements from a uniaxial compression test on dry Santa Cruz sand (SCS in Ruiz (2003)) are shown as black circular symbols, for one load cycle from ≈ 0.4 to 4 MPa.

velocity measurements and Poisson's ratio of the grain material via equation 4.34, are larger than those predicted for a sphere assembly with low contact friction, i.e. the slip limit, (Walton, 1987). Except for the Mindlin friction term ($f(\mu_{\mathrm{mob}})$) the remaining three parameters show minor variation with increasing vertical net stress. The peak friction angle as shown in Figure 4.8 for the Santa Cruz sand is close to that given by Ruiz (2003) ($\approx 31°$).
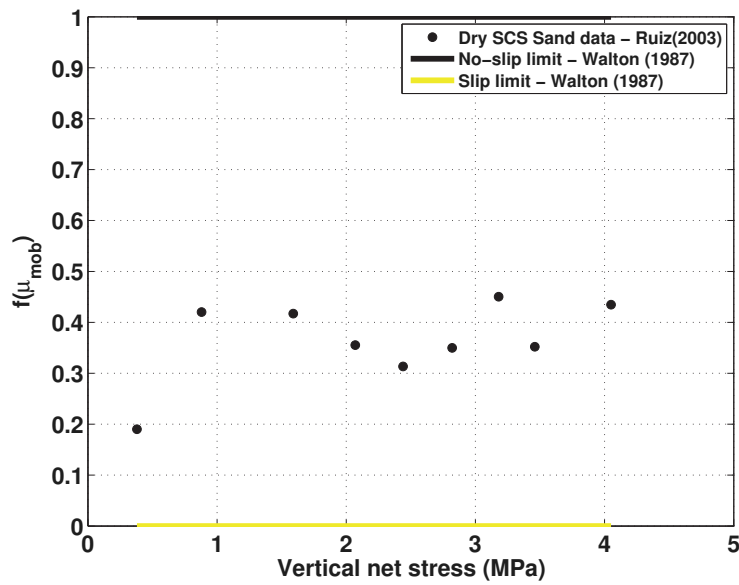
Figure 4.5: Mindlin's friction term versus applied vertical net stress (σ'_3) estimated from the ϵ values obtained for the Santa Cruz sand using equation 4.43 assuming a solid grain Poisson's ratio of 0.19 (Duffaut et al., 2010; Ruiz, 2003; Zimmer, 2003). The two special limits of Walton (1987), slip and no-slip, are shown as yellow and black lines for one load cycle from $\approx$ 0.4 to 4 MPa.
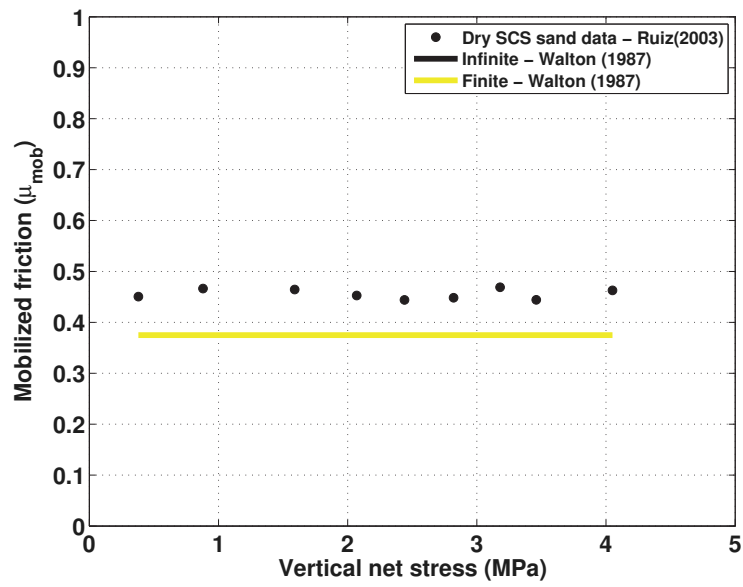
Figure 4.6: Mobilized contact friction versus applied vertical net stress (σ_3') estimated through $f(\mu_{\mathrm{mob}})$ and K_0'-values obtained for the Santa Cruz sand using equation 4.42 when assuming a Poisson's ratio of 0.19 of the grain material. The slip limit of Walton (1987) is shown as the yellow solid lines for one load cycle from ≈ 0.4 to 4 MPa. The infinite friction is not shown in the figure simply because it is infinite.
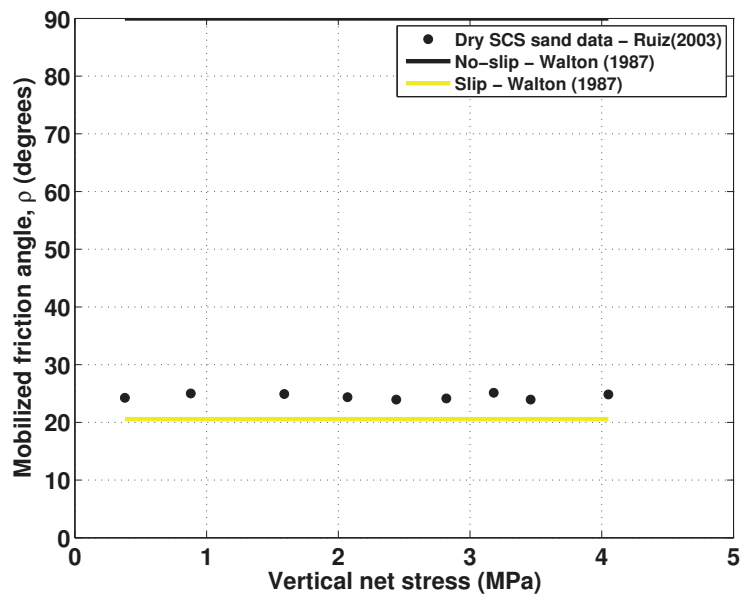
Figure 4.7: Mobilized friction angle (ρ) versus applied vertical net stress (σ_3') estimated from mobilized contact friction (μ_{mob}) of the Santa Cruz sand using equation 4.44 assuming a solid grain Poisson's ratio of 0.19. The two special limits of Walton (1987), slip and no-slip, are shown as yellow and black lines for one load cycle from ≈ 0.4 to 4 MPa.
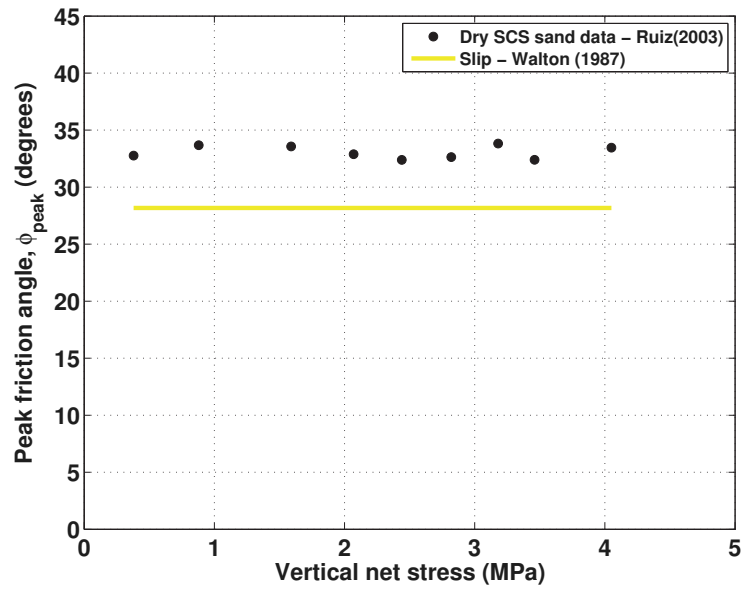
Figure 4.8: Peak friction angle (ϕ_{peak}) versus applied vertical net stress (σ_3') estimated from mobilized friction angle (ρ) of the Santa Cruz sand using equation 4.45 assuming a solid grain Poisson's ratio of 0.19 and a shear mobilsation factor (f_{shear}) of 0.7 (Janbu, 1985). The slip limit of Walton (1987) is shown as the yellow line for one load cycle from $\approx$ 0.4 to 4 MPa.

4.6 Discussion

Our model predicts non-linear behavior of the elastic moduli for a sphere assembly under uniaxial compression through incorporating frictional contacts between spheres. Under the assumption of small strain deformation ($\delta_N <<$ R) an instantaneous negative stress-induced elastic anisotropy is predicted for all Thomsen (1986) parameters where $\epsilon > \delta > \gamma$ of the sphere pack. These elastic anisotropy parameters remain constant as long as both the K_0'-loading and interparticle contact friction are constant. Increasing the intergrain contact friction would reduce the magnitude of the elastic anisotropy (less negative ϵ-values) even though this leads to a lower K_0'-value. We argue that our modeling results as shown in Figure 4.4 fit well when compared with corresponding P-wave anisotropy measurements of an unconsolidated beach sand exposed to an uniaxial strain loading reported by Ruiz (2003). The sand has a much higher porosity (Ruiz, 2003) than that of a random pack of equal spheres (36%), nine porosity units higher, which we think is the main cause of the overprediction of the modeled vertical and horizontal P-wave velocities with respect to the corresponding velocities of the Santa Cruz sand, Figure 4.3. However, a very good fit is observed when comparing the modeled and measured moduli ratios through the Thomsen ϵ parameter where the elastic anisotropy measurements fall nicely in between the slip and no-slip limits defined by (Walton, 1987). We argue that this is reasonable because the moduli ratio expressed as ϵ is less sensitive to porosity differences in rocks, or expressed differently, the elastic moduli e.g. C_{11}^{dry} and C_{33}^{dry} of a granular medium has a fairly similar relative dependence on the intrinsic porosity given that the stress loading path is more or less the same. A very good correlation is also observed between the measured K_0'-values shown in Figure 4.2 and the corresponding stress-induced P-wave velocity anisotropy measurements (Figure 4.4) on the Santa Cruz sand. A slight variation, up or down, in K_0' during loading leads to a similar variation of the P-wave velocity anisotropy (Figure 4.4). This variation supports our argument about the interplay between stress ratio (K_0') and interparticle contact friction causing elastic anisotropy. Theoretically, the P-wave anisotropy for a given set of K_0'- and $f(\mu)$-values is constant. This is reasonable since the contact theory assumes purely elastic deformation (small strains) of the sphere pack. Hence, the porosity is constant during compression implying no new contacts are made or lost within the sphere assembly. On the other hand the minor variation observed in the measured K_0' of the sand during loading is likely to be due to grain rearrangement causing slight changes of the macroscopic intergrain friction of the sample across the vertical net stress range of ≈ 0.4 to 4 MPa. We also observe consistently lower measured P-wave

anisotropy of the sand, compared to that of the slip limit, over the complete load path which is reasonable because the sand grains are far more angular than the smooth spheres assumed in the model, e.g., in Figure 2 of Zimmer et al. (2007). This suggest that loose uncemented sand or sandstones with low grain-to-grain contact friction will show larger stress-induced elastic anisotropy (larger negative Thomsen parameters) than a sand or sandstone composed of grain contacts with larger intergrain friction for a given state of stress. Greater stress-induced velocity anisotropy (VTI) would be observed if K_0' is allowed to decrease during compression keeping the horizontal net stress constant. Such a loading path is shown by e.g. Yin (1992) on Massillon and Berea sandstones with porosities of about 20%. A saturation of the grain pack for the given state of stress requires the use of an anisotropic fluid substitution model e.g. that given by Brown and Korringa (1975) or Carcione (2001). This makes ϵ and δ non-linear with respect to vertical net stress while γ is unaffected (Duffaut et al., 2008; Bandyopadhyay, 2009).

We also show predictions of shear strength parameters in the cases of near zero and infinite contact friction together with that estimated for the Santa Cruz sand through use of the Mindlin friction term given in equation 4.43. Figures 4.5 through 4.8 show comparisons of four model-predictions of parameters characterizing the shear strength of a granular medium by use of the Mindlin friction term as a function of ϵ. Similar estimates can be made by use of δ or γ as given in equation 4.43. Both estimates of mobilized (Figure 4.7) and peak friction angles (Figure 4.8) are larger for the sand when compared to those of Walton's slip limit. This is as expected since the sand grains are more angular. Comparison of our peak friction angle estimate for the sphere pack assuming low friction (slip limit) fits well with experimental peak friction angle measurements performed on glass beads (Alshibli and Roussel, 2006). They observed peak friction angles between 25° and 32°, depending up on pressure and sphere sizes, as compared to our prediction of 28°. Correspondingly, peak friction angle estimates using a static friction coefficient through Coulomb's law, given by Ruiz (2003) equals 31° while our model predictions in Figure 4.8 are between 33° and 34°.

4.7 Conclusions

A random dense packing composed of identical elastic isotropic spheres becomes transversely isotropic under uniaxial strain loading conditions and five elastic moduli are needed to describe the effective medium. Hence, the elastic moduli are larger in the direction of the applied uniaxial compression than in the perpendicular directions. Several published contact models based on var-

ious loading and grain contact assumptions attempt to predict stress-induced elastic anisotropy. We propose a generalized version of a well accepted contact model by incorporating an arbitrary frictional contact behavior ranging between two special contact boundary conditions representing infinite and near zero friction. Our approach is based on the same mean strain-field and deformation assumptions as usually applied in contact theory. New expressions for the five elastic moduli as a function of Mindlin's extended tangential contact stiffness are given, describing an effective medium with frictional grain contacts.

All elastic moduli increase as both vertical net stress and contact friction increase and larger moduli are obtained in the direction of the applied uniaxial strain, as expected. On the other hand, the elastic moduli ratios and elastic anisotropy (ϵ, γ and δ) decrease with increasing interparticle contact friction and depends on factors such as the net stress ratio (K_0'), through the Mindlin friction term ($f(\mu)$) and the Poisson's ratio of the solid grain material. The modeled stress-induced elastic anisotropy is instantaneous, independent of the applied vertical net stress, and is always negative when the uniaxial strain is applied along the axis of symmetry in the vertical direction. Our model predicts $\epsilon > \delta > \gamma$ for all grain contact conditions going from the slip limit to the no-slip limit.

Theoretical expressions are derived for both mobilized and maximum shear strength of a spherical grain pack via elastic anisotropy using any of the Thomsen parameters ϵ, γ or δ together with the net stress ratio (K_0') ranging between zero and 1/4. The maximum or peak friction angle (maximum shear strength of the sphere pack) estimated from the mobilized friction and friction angle is between 28° and 32° which coincides with the magnitude of peak friction angle measurements obtained from a published experimental investigation on glass beads data. Similarly, comparison of model-derived peak friction angle in the slip limit fits fairly well with that derived using a static friction coefficient (0.6) for soft rocks, which is representative of this beach sand. The peak friction angles estimated for the slip limit are between 33° and 34°, while that measured from the Santa Cruz sand 31°.

Dry P-wave velocity predictions ($V_{p_{33}}^{\mathrm{dry}}$ and $V_{p_{11}}^{\mathrm{dry}}$) representing infinite and near-zero contact friction appear to consistently overestimate those obtained from experimental data on unconsolidated sand. This is most likely due to higher porosity of the sand sample compared to that assumed in the modeling. However, a comparison of modeled and measured P-wave anisotropy of the sand fit nicely inside the two special contact boundary conditions, slip and no-slip, indicating a larger macroscopic intergrain friction of the sand compared to that of the slip limit for a spherical grain pack. The P-wave anisotropy of the

sand is lower (less negative value) than that of Walton's slip limit most likely because the sand is composed of grains with higher angularity. Although, the sand is exposed to a lower $K_0^{'}$ loading than that of the slip limit. It is therefore favorable to explain the stress-dependent elastic anisotropy in unconsolidated granular materials in term of a rather complex interplay between a grain interlocking mechanism and the state of stress the material is exposed to.

4.8   Acknowledgements

References

Alassi, H., R. Holt, and M. Landrø, 2010, Relating 4D seismics to reservoir geomechanical changes using a discrete element approach: Geophysical Prospecting, **58**, 657–668.

Allen, P. A. and J. R. Allen, 1990, Basin analysis: principles and applications: Wiley-Blackwell.

Alshibli, K. A. and L. E. Roussel, 2006, Experimental investigation of slipstick behaviour in granular materials: International Journal for Numerical and Analytical Methods in Geomechanics, **30**, 1391–1407.

Athy, L. F., 1930, Density, porosity, and compaction of sedimentary rocks: AAPG Bulletin, **14**, 1–24.

Avseth, P., A. Dræge, A.-J. van Wijngaarden, T. A. Johansen, and A. Jørstad, 2008, Shale rock physics and implications for avo analysis: A north sea demonstration: The Leading Edge, **27**, 788–797.

Avseth, P., T. Mukerji, and G. Mavko, 2005, Quantitative seismic interpretation; applying rock physics tools to reduce interpretation risk: Cambridge University Press.

Avseth, P. and N. Skjei, 2011, Rock physics modeling of static and dynamic reservoir properties - a heuristic approach for cemented sandstone reservoirs: The Leading Edge, **30**, 90–96.

Bandyopadhyay, K., 2009, Seismic anisotropy: Geological causes and its implications to reservoir geophysics: PhD thesis, Stanford University.

Bjørlykke, K., 1999, Principal aspects of compaction and fluid flow in mudstones: Geological Society London Special Publications, **158**, 73.

Bjørlykke, K., M. Ramm, and G. C. Saigal, 1989, Sandstone diagenesis and porosity modification during basin evolution: Geologische Rundschau, **78**, 243–268.

Boggs, S., 1995, Principles of sedimentology and stratigraphy, volume **774**: Prentice Hall New Jersey.

Brandt, H., 1955, A study of the speed of sound in porous granular media: Journal of Applied Mechanics, **22**, 479–486.

Brevik, I., G. R. Ahmadi, T. Hatteland, and M. A. Rojas, 2007, Documentation and quantification of velocity anisotropy in shales using wireline log measurements: The Leading Edge, **26**, 272–277.

Brown, R. J. S. and J. Korringa, 1975, On the dependence of the elastic properties of a porous rock on the compressibility of the pore fluid: Geophysics, **40**, 608–616.

Brudy, M. and H. Kjørholt, 2001, Stress orientation on the Norwegian continental shelf derived from borehole failures observed in high-resolution borehole imaging logs: Tectonophysics, **337**, 65–84.

Budhu, M., 2007, Soil mechanics and foundations: John Wiley & Son, Inc.

Carcione, J. M., 2001, Wave fields in real media: Wave propagation in anisotropic anelastic and porous media: Pergamon.

Chen, G., D. Yale, X. Huang, S. Xu, C. Finn, and G. Boitnott, 2006, Stress-induced velocity anisotropy of unconsolidated sand under realistic reservoir stress conditions: SEG Technical Program Expanded Abstracts, **25**, 1879–1882.

Chuhan, F. A., A. Kjeldstad, K. Bjørlykke, and K. Høeg, 2002, Porosity loss in sand by grain crushing–experimental evidence and relevance to reservoir quality: Marine and Petroleum Geology, **19**, 39–53.

Digby, P. J., 1981, The effective elastic moduli of porous granular rocks: Journal of Applied Mechanics, **48**, 803–808.

Domenico, S. N., 1977, Elastic properties of unconsolidated porous sand reservoirs: Geophysics, **42**, 1339–1368.

Duffaut, K., M. Landrø, and R. Sollie, 2010, Using Mindlin theory to model friction-dependent shear modulus in granular media: Geophysics, **75**, E143–E152.

Duffaut, K., Ø. Pedersen, and M. Landrø, 2008, Stress induced velocity anisotropy during compaction of sediments, *in* the 5th ROSE meeting, Norwegian University of Science and Technology, NTNU, Trondheim, Norway.

Fjær, E., R. M. Holt, P. Horsrud, A. M. Raaen, and R. Risnes, 2008, Petroleum Related Rock Mechanics, No. 53. Amsterdam: Developments in Petroleum Science.

Furre, A. K., 1997, Physical Modelling of Elastic Anisotropy in Porous Media: PhD thesis, Department of Petroleum Engineering and Applied Geophysics, Norwegian University of Science and Technology, NTNU, Trondheim, Norway.

Gassmann, F., 1951, Elastic waves through a packing of spheres: Geophysics, **16**, 673–685.

Graham, J., M. Alfaro, and G. Ferris, 2004, Compression and strength of dense sand at high pressures and elevated temperatures: Canadian Geotechnical

Journal, **41**, 1206–1212.

Gueguen, Y. and M. Bouteca, 1999, Mechanical Properties of Rocks: Pore Pressure and Scale Effects: Oil & Gas Science and Technology, **54**, 703–714.

Hedberg, H. D., 1936, Gravitational compaction of clays and shales: American Journal of Science, **31**, 241–287.

Hertz, H., 1882, Über die Beruhrüng fester elastischer Körper: Journal fur die reine und angewandte Mathematik, **92**, 156–171.

Holt, R. M., L. Li, and J. F. Stenebråten, 2007, Compaction behavior of unbonded granular medium: Discrete particle vs. experimental vs. analytical modelling, *in* in Proceedings of the First Canada -U.S. Rock Mechanics Symposium, 393–401.

Holt, R. M., O.-M. Nes, and E. Fjær, 2005, In-situ stress dependence of wave velocities in reservoir and overburden rocks: The Leading Edge, **24**, 1268–1274.

Horbury, A. and A. Robinson, 1993, Diagenesis and basin development: American Association of Petroleum Geologists.

Hornby, B. E., 1994, The elastic properties of shales: PhD thesis, University of Cambridge.

Hudson, J. A., 1981, Wave speeds and attenuation of elastic waves in material containing cracks: Geophysical Journal of the Royal Astronomical Society, **64**, 133–150.

Janbu, N., 1985, Soil models in offshore engineering: Géotechnique, **35**, 241–281.

Johnson, D. L., L. M. Schwartz, D. Elata, J. G. Berryman, B. Hornby, and A. N. Norris, 1998, Linear and nonlinear elasticity of granular media: stress-induced anisotropy of a random sphere pack: Journal of Applied Mechanics, **65**, 380–388.

Johnston, D. H., 1987, Physical properties of shale at temperature and pressure: Geophysics, **52**, 1391–1401.

Lander, R. H. and O. Walderhaug, 1999, Predicting porosity through simulating sandstone compaction and quartz cementation: AAPG bulletin, **83**, 433–449.

Landrø, M., 2001, Discrimination between pressure and fluid saturation changes from time-lapse seismic data: Geophysics, **66**, 836–844.

Landrø, M., P. Digranes, and L. K. Strønen, 2001, Mapping reservoir pressure and saturation changes using seismic methods - possibilities and limitations: First Break, **19**, 671–677.

Magara, K., 1980, Comparison of porosity-depth relationships of shale and sandstone: Journal of Petroleum Geology, **3**, 175–185.

Mavko, G., T. Mukerji, and J. Dvorkin, 1998, The rock physics handbook:

Cambridge University Press.

Mindlin, R. D., 1949, Compliance of elastic bodies in contact: Journal of Applied Mechanics, **16**, 259–268.

Mondol, N. H., K. Bjørlykke, J. Jahren, and K. Høeg, 2007, Experimental mechanical compaction of clay mineral aggregates - Changes in physical properties of mudstones during burial: Marine and Petroleum Geology, **24**, 289–311.

Murphy III, W. F., 1982, Effects of microstructure and pore fluids on the acoustic properties of granular sedimentary materials: PhD thesis, Stanford University.

Nur, A., 1971, Effects of stress on velocity anisotropy in rocks with cracks: Journal of Geophysical Research, **76**, 2022–2034.

Nur, A. and G. Simmons, 1969, Stress-induced velocity anisotropy in rock: an experimental study: Journal of Geophysical Research, **74**, 6667–6674.

Prasad, M., 2002, Acoustic measurements in unconsolidated sands at low effective pressure and overpressure detection: Geophysics, **67**, 405–412.

Rathore, J. S., E. Fjær, R. M. Holt, and L. Renlie, 1995, P-and S-wave anisotropy of a synthetic sandstone with controlled crack geometry: Geophysical Prospecting, **43**, 711–728.

Rieke, H. H. and G. V. Chilingar, 1974, Compaction of argillaceous sediments: Elsevier Science Ltd.

Rüger, A., 1997, P-wave reflection coefficients for transversely isotropic models with vertical and horizontal axis of symmetry: Geophysics, **62**, 713–722.

Ruiz, D. S. V., 2003, Intrinsic and Stress-induced Velocity Anisotropy in Unconsolidated Sands: PhD thesis, Stanford University.

Sayers, C. M., 1988, Stress-induced ultrasonic wave velocity anisotropy in fractured rock: Ultrasonics, **26**, 311–317.

———, 1999, Stress-dependent seismic anisotropy of shales: Geophysics, **64**, 93.

———, 2002, Stress-dependent elastic anisotropy of sandstones: Geophysical prospecting, **50**, 85–95.

———, 2005a, Seismic anisotropy of shales: Geophysical Prospecting, **53**, 667–676.

———, 2005b, Sensitivity of elastic-wave velocities to stress changes in sandstones: The Leading Edge, **24**, 1262–1266.

Schwartz, L. M., W. F. Murphy III, and J. G. Berryman, 1994, Stress-induced transverse isotropy in rocks: SEG Technical Program Expanded Abstracts, **13**, 1081–1085.

Shapiro, S. A., 2003, Elastic piezosensitivity of porous and fractured rocks: Geophysics, **68**, 482–486.

Sherlock, D., K. Nihei, S. Nakagawa, and L. Duranti, 2007, Stress-induced velocity anisotropy measurements in unconsolidated sand using a phased-array uniaxial compaction cell: SEG Technical Program Expanded Abstracts, **26**, 1550–1554.

Stoll, R. D., 1989, Stress-induced anisotropy in sediment acoustics: The Journal of the Acoustical Society of America, **85**, 702–708.

Storvoll, V., K. Bjørlykke, and N. H. Mondol, 2005, Velocity-depth trends in Mesozoic and Cenozoic sediments from the Norwegian Shelf: AAPG Bulletin, **89**, 359–381.

Terzaghi, K., 1943, Theoretical soil mechanics: John Wiley & Sons, Inc.

Thomsen, L., 1986, Weak elastic anisotropy: Geophysics, **51**, 1954–1966.

——, 1995, Elastic anisotropy due to aligned cracks in porous rock1: Geophysical Prospecting, **43**, 805–829.

Walsh, J. B., 1965, The effect of cracks on the uniaxial elastic compression of rocks: Journal of Geophysical research, **70**, 399–411.

Walton, K., 1987, The effective elastic moduli of a random packing of spheres: Journal of the Mechanics and Physics of Solids, **35**, 213–226.

Wang, Z., 2002, Seismic anisotropy in sedimentary rocks, part 2: Laboratory data: Geophysics, **67**, 1423–1440.

Wang, Z. and A. Nur, 1992, Elastic wave velocities in porous media: A theoretical recipe, *in* Wang, Z. and A. Nur, eds., Seismic and acoustic velocities in reservoir rocks, v.2: Theoretical and model studies: SEG Geophysics Reprint Series No. 10, 1–35.

Wang, Z. Z., H. Wang, and M. E. Cates, 2001, Effective elastic properties of solid clays: Geophysics, **66**, 428–440.

White, J. E., L. Martineau-Nicoletis, and C. Monash, 1983, Measured anisotropy in Pierre shale: Geophysical Prospecting, **31**, 709–725.

Wolf, K. H. and G. V. Chilingarian, 1975, Diagenesis of sandstones and compaction: Developments in Sedimentology, **18**, 69–444.

Wyllie, M. R. J., A. R. Gregory, and G. H. F. Gardner, 1958, An experimental investigation of factors affecting elastic wave velocities in porous media: Geophysics, **23**, 459.

Yin, H., 1992, Acoustic velocity and attenuation of rocks: Isotropy, intrinsic anisotropy, and stress induced anisotropy: PhD thesis, Stanford University.

Zimmer, M., 2003, Seismic velocities in unconsolidated sands: Measurements of pressure, sorting and compaction effects: PhD thesis, Stanford University.

Zimmer, M., M. Prasad, G. Mavko, and A. Nur, 2007, Seismic velocities of unconsolidated sands: Part 1-Pressure trends from 0.1 to 20 MPa: Geophysics, **72**, E1–E13.

Zimmerman, R. W., 1991, Compressibility of sandstones: Elsevier Science Ltd.

Chapter 5

Closing remarks

The change in stress sensitivity of elastic-wave velocities in sandstones of different degree of consolidation are investigated in this thesis by use of grain contact models that presuppose idealized random packing of equal spheres with various assumptions with regard to grain contact and stress loading conditions. Different granular model assumptions are applied in the different papers to relate velocity changes to the microscopic grain contact level as well as explaining differences in the stress sensitivity of compressional to shear velocity ratio (V_p/V_s) derived from real time-lapse seismic amplitude observations. It is interesting to note that the individual microstructure model assumptions actually semi-quantitatively explain ultrasonic core measurements, acoustic logs and time-lapse seismic amplitude responses. To further investigate the time-lapse seismic amplitude response of the Gullfaks Field it would be interesting to link 3D geomechanical and seismic modeling and compare these results with the real seismic observations.

From a rock physics modeling point of view it would be interesting to further explore the possibility to develop a grain contact model that enbles to capture changes in stress sensitivity of elastic-wave velocities as unconsolidated sand lithify into sandstone through the interplay of mechanical and chemical compaction. The complexity in the problem is large but the model needs to be simplified to capture the major alteration of the sediment related to compaction, cementation and recrystallization. Also modification of the idealized sphere contact models to handle grain geometries with aspect ratios less than one is also worth investigating. There exists some work on this theme. Finally, grain contact models that handle loading paths and in-situ stress conditions different from the usual hydrostatic and uniaxial loading paths can be useful towards improving our ability to interpret and understand e.g. the seismic data at hand.

The implication of the results obtained in Chapter four on stress-induced elastic-wave anisotropy in unconsolidated sands are worth following to reveal the impact it might have on seismic imaging and amplitude interpretation at shallow depths.

Appendix A

Stress and fluid sensitivity in two North Sea oil fields - comparing rock physics models with seismic observations

Stress and fluid sensitivity in two North Sea oil fields—comparing rock physics models with seismic observations

Kenneth Duffaut, Statoil
Per Avseth, Odin Petroleum
Martin Landrø, Norwegian University of Science and Technology

During 4D seismic reservoir characterization, it is important to have reliable rock physics models for both static (e.g., mineralogy, porosity, cement volume) and dynamic (e.g., saturation, pressure, temperature) reservoir parameters. Without a good understanding of reservoir geology and associated static rock physics properties, it is impossible to interpret time-variant changes in pore pressure and saturation (Andersen et al., 2009). The dry rock properties of the reservoir can be obtained from well-log data combined with geological information about mineral composition and rock texture, and Gassmann theory to estimate the effect of pore fluid changes. Normally, core measurements are undertaken to quantify stress sensitivity, but these are often affected by induced fractures caused by the coring acquisition that will enhance the stress sensitivity of the rock (Holt et al., 2005). Duffaut and Landrø (2007) showed how calibrated Hertz-Mindlin contact theory could be applied to estimate stress sensitivity on V_P/V_S ratios in two North Sea oil fields (Statfjord and Gullfaks), in order to explain observed AVO signatures during water injection and associated pore-pressure increase. It was found that loose Gullfaks sands yielded high V_P/V_S ratios (up to about 7) during water injection, whereas slightly quartz-cemented Statfjord sands yielded more moderate changes in V_P/V_S ratios (approximately 2). The differences were modeled by varying the number of grain-to-grain contacts. In this paper we further investigate the pressure sensitivity of seismic parameters in these two oil fields, applying the rock physics modeling approach presented by Avseth and Skjei (*TLE*, this issue), and we demonstrate a good match between rock physics modelling results and seismic observations in terms of V_P/V_S. The stress sensitivity of V_P/V_S decreases drastically when sands become cemented, as crack-like porosity at grain contacts are eliminated.

Well-log and seismic data observations

Duffaut and Landrø investigated 4D seismic anomalies at Gullfaks and Statfjord, respectively (Figure 1), and in particular AVO signatures around injection wells in the two fields were quantified in terms of elastic parameters. It was found that the V_P/V_S ratio in the oil reservoir of the studied Gull-
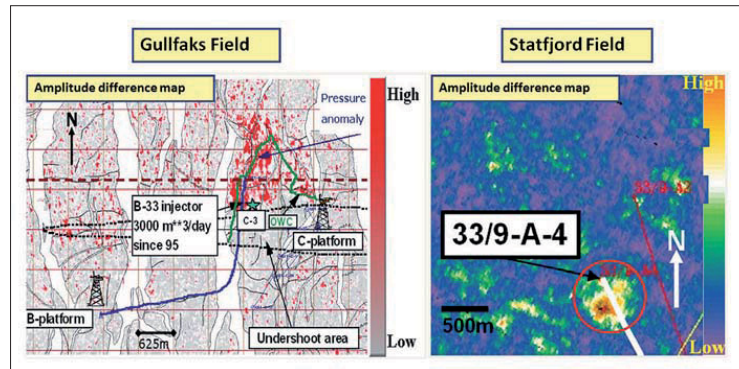

Figure 1. *Seismic amplitude difference maps for Gullfaks and Statfjord fields, in areas with water injection at two injector wells. (Duffaut and Landrø, 2007). For the Gullfaks case, the anomaly is seen both above and below the OWC (green line in map to the left). For the Statfjord case, the anomaly is a pure pressure effect, as the monitor survey was shot when injector was online, while the base survey was shot after injection, but with injector offline, implying no pressure buildup at that time.*
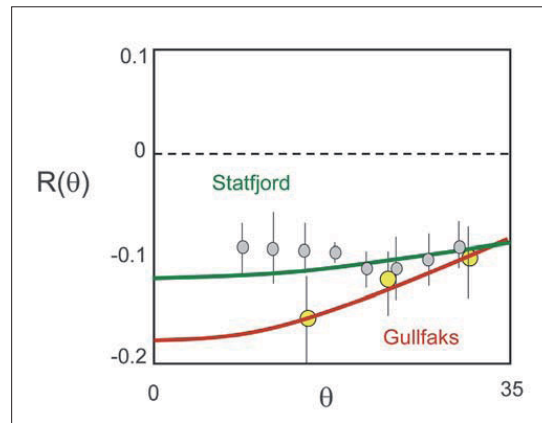

Figure 2. *AVO signatures after water injection around the water injection wells shown in the map in Figure 1. Note the dramatic change in AVO signatures in the Gullfaks case (yellow circles represent average calibrated rms values picked at the top reservoir from offset stacks of the nearby Gullfaks injector; error bars are indicated). Here, a V_P/V_S ratio in the reservoir of approximately 7 was needed to explain the significant positive AVO gradient after water injection. For the Statfjord case, a more gentle/flat AVO gradient is observed (gray circles represent average calibrated amplitude values picked from prestack angle gathers nearby Statfjord injector), and a V_P/V_S ratio of ~2 in the reservoir gives the optimal fit to the observations (adapted and modified from Duffaut and Landrø, 2007).*

faks sands increased drastically during water injection and associated pore-pressure increase. The AVO signature of the monitor case was optimally fitted with a V_p/V_s ratio of 7, in order to describe the strong positive AVO gradient during injection (Figure 2). For the Statfjord case, a much smaller AVO gradient was observed during water injection, and a V_p/V_s ratio of ~2 gave a fairly good fit to the observed AVO signature.

In this study, we investigate well-log data from two production wells from Gullfaks and Statfjord, respectively. These were selected as example wells that penetrate representative sections of the reservoir zones, yet are outside the areas affected by pore-pressure increase associated with injection. Well 1 (Gullfaks) is almost vertical (4° inclination at target level) and 1.7 km southeast of the injector shown in Figure 1. Well 2 (Statfjord) is also close to vertical (7°) and is 2.7 km southeast of the injector shown in Figure 1. The well-log data from the two wells are shown in Figure 3. The log data comprise shale volume estimated from gamma ray (V_{sh}), water saturation (S_w), P-wave velocity (V_p), S-wave velocity (V_s) and density. The zone of interest in the Gullfaks well is the Cook Formation from 1795 to 1866 m. Here, we observe a somewhat heterogeneous reservoir zone with varying oil saturation. The P-wave velocities range from ~2000 to 2200 m/s and the S-wave velocities are approximately 1000 m/s.

Figure 3. Well-log data from Gullfaks (well 1, above) and Statfjord (well 2, below) fields, including shale volume (green curve in leftmost subplots), water saturation (red curve in leftmost subplots), P-wave velocity (blue curve in middle subplots), S-wave velocity (cyan curve in middle subplots), and density (right subplot). Note the somewhat higher velocities in the Statfjord well compared to the Gullfaks well, indicating the higher degree of consolidation in the deeper Statfjord case.

Densities vary from ~2000 to 2200 kg/m³, and the average porosity in the reservoir is 0.33. Furthermore, the Gullfaks reservoir sands in this well are known to be loose or poorly consolidated. There is also a more poorly sorted, shaly sandstone interval of the Cook Formation, ranging from 1866 to 1923 m, which is water-saturated. Here, the average porosity is 0.22. The zone of interest in the Statfjord well is the Tarbert Formation from 2523 to 2562 m. Also here we observe a somewhat heterogeneous reservoir zone with fluctuating oil saturation. The P-wave velocities range from ~2500 to 3000 m/s and S-wave velocities are approximately 1200 to 1600 m/s. Densities vary quite a lot, but the cleanest reservoir zone shows densities of approximately 2100 kg/m³. The average porosity of the reservoir sandstones is found to be 0.30. Knowing that well 1 and well 2 penetrate the target zones in the two oil fields, we assume that the well-log data in these wells are representative for the reservoir properties prior to pressure changes in the areas where the AVO anomalies were
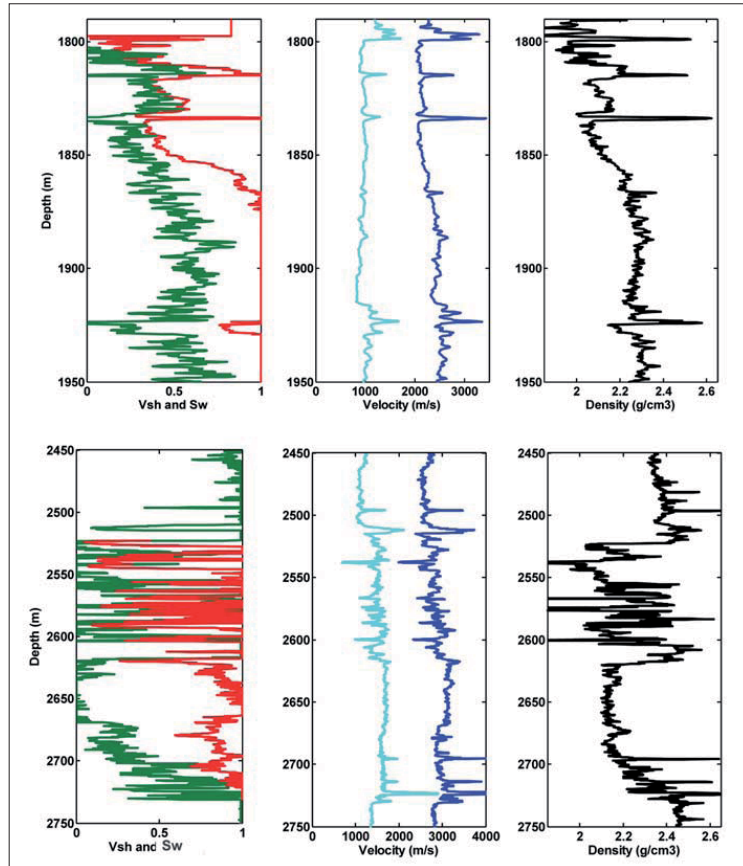
observed around the two injector wells. Hence, we will use these well-log data to estimate dry rock properties that we need in order to quantify stress and fluid sensitivity in the two injection cases.

Dry rock properties and stress sensitivity

From the well-log data above, we use Gassmann theory to estimate dry rock properties. The fluid properties for the Gullfaks Field are as follows: K_{water} = 2.54 GPa, K_{oil} = 1.41 GPa, water density = 1040 kg/m³, and oil density = 824 kg/m³. The fluid properties for the Statfjord Field are as follows: K_{water} = 2.72 GPa, K_{oil} = 0.64 GPa, water density = 1000 kg/m³, and oil density = 693 kg/m³. We assume pure quartz mineral with mineral bulk and shear moduli of 37 GPa and 44 GPa, respectively. Figure 4 (left) shows K_{dry} versus porosity for the reservoir sands in well 1 (Gullfaks) and well 2 (Statfjord) plotted together with the soft and stiff bounds defined by Avseth and Skjei. Note that the Gullfaks data are
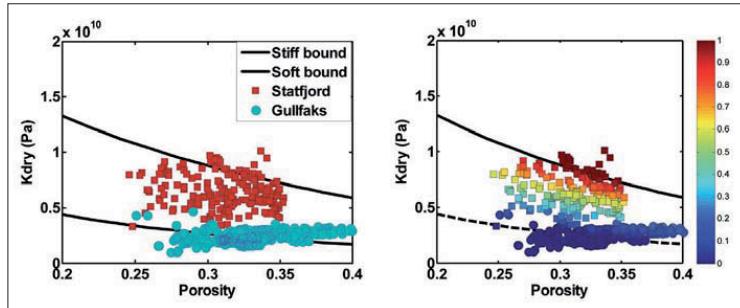
Figure 4. Dry rock incompressibility versus porosity for the Gullfaks and Statfjord reservoirs (left). Note that the Gullfaks data plot close to the pressure-sensitive soft bound and the Statfjord data plot closer to the pressure-insensitive stiff bound. A weight factor (color code in right hand subplot) can be estimated depending on the distance from a data point to the bounds, and this weight factor is used to estimate the stress sensitivity curve for each data point.
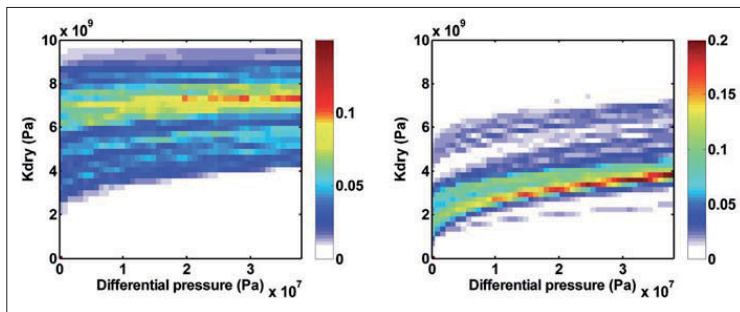

Figure 5. Probability density functions (pdfs) of stress sensitivity for the Statfjord (left) and Gullfaks (right) well-log data investigated in this study (color = probability). Note the significant larger stress sensitivity for the Gullfaks case, even though the porosities overlap in the two cases. The cementation occurring in the Statfjord Field sandstones is drastically reducing the stress sensitivity and causing much higher dry frame bulk moduli. The unconsolidated sands at the Gullfaks field are stress-sensitive due to the loose grain contacts that can be pressed together during increasing effective stress.

is assumed to have zero friction for any pressure, and stress sensitivity is associated with loose grain contacts that are pressured together in accordance with Walton smooth contact theory. Duffaut et al. (2010) demonstrated how stress sensitivity in unconsolidated sands is also affected by pressure-dependent friction that will amplify the stress sensitivity associated with increasing area of contact between grain contacts in loose sands. In the patchy cement model, however, every grain contact that is cemented will contribute to decreasing stress sensitivity.

Using the extracted weight factors, we can estimate probability density functions (pdf) of stress sensitivity for the two reservoirs, plotted as K_{dry} versus differential pressure in Figure 5 (we assume here that differential pressure equals effective pressure). We observe that the stress sensitivity is larger, in general, for the Gullfaks case, than for the Statfjord case. There are overlaps between the stress pdfs, but the higher probabilities are well separated and give us a good impression of the expected stress sensitivity in the two fields. It is also interesting to note that the uncertainties in stress sensitivity decrease with increasing differential pressure (i.e., relatively high probabilities are depicted in yellow and red in Figure 5). We can use the pdfs in Figure 5 to evaluate the expected changes in elastic and seismic properties during injection in the two fields. The initial vertical stress in the Gullfaks case is only approximately 6–8 MPa, whereas in the Statfjord case, the initial vertical stress is around 15 MPa. The pore-pressure increase is approximately 6 MPa in the Gullfaks case during injection, which means we are approaching zero differential pressure. We see that the expected K_{dry} at zero differential pressure is only 1–2 GPa, and at 6 MPa it is around 3 GPa. For the Statfjord case, where initial differential pressure is approximately 15 MPa, the pore-pressure increase is around 8 MPa, meaning that the differential pressure is approximately 7 MPa during injection. Hence, we expect a drop in dry rock incompressibility of less than 0.5 GPa. These modeling results can explain the observed AVO differences in Figure 2. The fact that the Gullfaks reservoir sands are poorly consolidated or unconsolidated, and the pore-pressure increase leads to nearly zero differential pressure, results in high V_p/V_s ratios. For the Statfjord case, the more consolidated nature of the reservoir sandstones, in combination with a larger initial differential pressure, causes little change in V_p/V_s ratios during injection. In the next section, we investigate how the

plotting close to and partly on the soft bound. This confirms that the reservoir sands in the Cook Formation of Gullfaks Field are loose or poorly consolidated. The Statfjord data, on the other hand, are plotting between the soft and the stiff bounds, even though the porosities quite overlap with the Gullfaks data. This indicates that the reservoir sandstones in the Tarbert Formation of Statfjord Field are slightly cemented (Avseth et al., 2009).

We use the approach suggested by Avseth and Skjei to estimate the weight factor of each data point representing the relative location between the soft and stiff bounds, where any point falling on or below the soft bound will have W = 0 and any point falling on or above the stiff bound will have W = 1. (Figure 4, right). Here we show results only for the dry bulk modulus, but a similar approach is done for the shear modulus. Following the arguments of Avseth and Skjei, we assume that this weight function is directly related to the degree of consolidation and cementation, which again will control the stress sensitivity according to a patchy cement model. In the model developed by Avseth and Skjei, the soft bound

stress-sensitivity functions derived by Avseth and Skjei will affect acoustic impedance versus V_p/V_s, in so-called dynamic rock physics template plots.

Rock physics template analysis of reservoir changes

The nonlinear regression formulas extracted by Avseth and Skjei have been applied to the Gullfaks and Statfjord cases. We assume that the target sand in Gullfaks Field has zero cement, or is completely unconsolidated, as demonstrated in Figure 4. The average porosity in the Cook Formation sands encountered by the Gullfaks well in this study is 0.33 for the oil zone and 0.22 for the more poorly sorted water zone. For the Statfjord case, the Tarbert Formation sands have an average porosity of 0.3 both for the oil and water zones. The cement volume in the Statfjord case has been estimated to be approximately 3–4% using the technique of Avseth et al. (2009). This is close to the estimates from thin-section and SEM of 1–3% reported by Bjørlykke et al. (1992). Using only porosity and cement volume as input parameters, we are able to predict the pressure sensitivity for the Gullfaks and Statfjord cases. Figure 6 shows that unconsolidated sands will have much larger stress sensitivity than cemented sandstones, especially in terms of V_p/V_s. For unconsolidated sands saturated with oil or water, the V_p/V_s ratio can go to infinitely high values when differential pressure approaches zero. This makes sense, since loose sands at zero differential pressure will go into suspension phase without shear rigidity.

Figure 7 shows the regression model trends compared with the well-log data described in this study. In general, there is a nice match between the well-log data and the regression model results. Recall that the only input parameters for
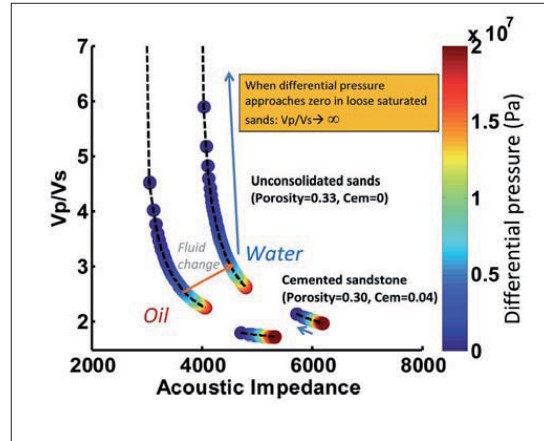

Figure 6. Pressure-sensitivity modeling using regression formulas extracted by Avseth and Skjei for unconsolidated sands and cemented sandstones filled with oil and brine. The simulation shows differential pressure varying from 20 to 0 MPa. Note the larger pressure sensitivity for the unconsolidated sands than for the cemented sandstones. Inputs to the regression formulas include porosity, cement volume, and effective pressure (we assume effective pressure = differential pressure). The injection processes described by Duffaut et al. (2007) for Gullfaks and Statfjord are indicated with arrows. For the Gullfaks case, we have oil replaced by water and pore-pressure increase during injection, from the base to the monitor. Here we expect a dramatic increase in V_p/V_s as differential pressure approaches zero. For the Statfjord case, the base and monitor 4D are both water-saturated, but monitor data were recorded when an injector was online and pore pressure increasing accordingly. Here, we expect a small increase in V_p/V_s in the vicinity of 2.
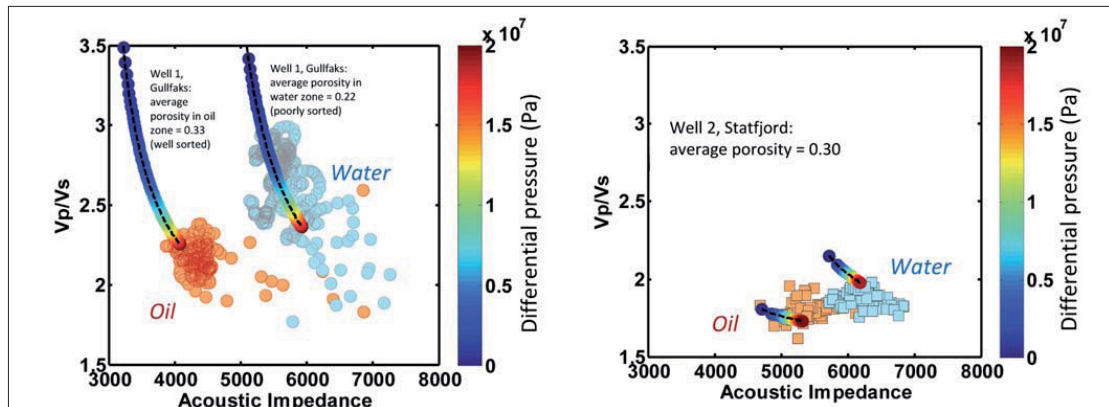

Figure 7. Stress-sensitivity curves derived from regression formulas by Avseth and Skjei plotted as acoustic impedance versus V_p/V_s compared with well-log data from Gullfaks (left) and Statfjord (right) fields, respectively. We have assumed 0% cement for Gullfaks and 4% cement for Statfjord. The well-log data are representative of in-situ conditions prior to pressure changes associated with injection/production. The effective vertical stresses are 6–8 MPa at Gullfaks and approximately 15 MPa at Statfjord. In general, there is a good match between models and data. We slightly overpredict V_p/V_s ratios for loose oil sands at Gullfaks. Some of the sands may have initial cement (<1%). The assumption of zero friction for loose sands may also give V_p/V_s ratios that are too high, as friction may increase with pressure (Duffaut et al., 2010). Also, the monomineralogic assumption (quartz) may be unrealistic. The water zone in the Gullfaks well is found to be rather shaly, yet we obtain a good match with the model. The water-saturated sandstones in the Statfjord case may be slightly more cemented than the oil zone. As shown in Figure 6, the stress sensitivity is expected to be much larger for the loose Gullfaks sands than for the cemented Statfjord sandstones.

the dry rock properties here are porosity, cement volume, and differential pressure, and these are combined with Gassmann theory to predict the saturated seismic properties. The values for in-situ differential pressures (6 MPa for Gullfaks and 15 MPa for Statfjord) are fairly near the data clouds for both oil and water cases. The V_p/V_s ratios are predicted to be somewhat higher for the loose Gullfaks sands than what is observed in the well-log data. This could be due to the fact that the model is derived from contact theory where we assume zero friction in loose sands. Adding some pressure-dependent friction in the original model could have given an even better fit here. It could also be that some of the Gullfaks sands have tiny amounts of cement that affect the V_p/V_s ratios (Bjørlykke et al., 1992, report estimates of 0 to 0.7%). For the shalier and poorly sorted water-filled sands, we observe a good match even though the modeling assumes pure quartz. For the cemented Statfjord sandstones, we observe an excellent match for the oil-saturated case, but V_p/V_s values are predicted somewhat higher in the water-saturated sandstones. It could be that the cement volume in the water-filled sandstones is slightly higher than for the oil-filled sandstones, as we assumed 4% for the whole Tarbert Formation.

Regarding predicted dynamic changes during injection, we observe that the regression formulas predict relatively large increase in V_p/V_s ratios with decreasing differential pressure for the sands in the Gullfaks area, and that we can easily get V_p/V_s ratios of 7 or higher when differential pressure approach zero. For the cemented Statfjord sandstones filled with water, a pore-pressure increase of 8 MPa will result in a V_p/V_s of approximately 2. These observations match well with the V_p/V_s values derived from AVO analysis by Duffaut and Landrø (2007), as shown in Figure 2.

Conclusions

We have quantified the combined stress and fluid sensitivity during injection in two North Sea sandstone reservoirs. Using rock physics models based on contact theory, we have documented the effect of consolidation and cement volume on V_p/V_s ratios in these two cases, and our results agree well with previously published AVO studies from the two fields. The results in this study validate the rock physics modeling

approach for patchy cemented sandstones where we assume stress sensitivity is maintained through microcracks at loose grain contacts, as presented by Avseth and Skjei. In general, we will expect stress sensitivity to decrease with burial depth due to consolidation and cementation. Pressure-dependent friction may increase the stress sensitivity of unconsolidated grain contacts, but in this study we have assumed zero friction for loose sands. Future research will further investigate the role of friction, nonuniform grain contacts and heterogeneous stress patterns on fluid and stress sensitivity of reservoir sandstones. Ultimately, the modeling approach presented in this study can be integrated with seismic inversion and reservoir mapping from 4D seismic for sandstone reservoirs. **TLE**

References

Andersen, C. F., V. Grosfeld, A-J. van Wijngaarden, and A. N. Haaland, 2009, Interactive interpretation of 4D prestack inversion data using rock physics templates, dual classification, and real-time visualization: The Leading Edge, **28**, 898–906.

Avseth, P., A. Jørstad, A-J. Wijngaarden, and G. Mavko, 2009, Rock physics estimation of cement volume, sorting, and net-to-gross in North Sea sandstones: The Leading Edge, **28**, 98–108.

Bjørlykke, K., T. Nedkvitne, M. Ramm, and G. Saigal, 1992, Diagenetic processes in the Brent Group (Middle Jurassic) reservoirs of the North Sea: an overview: Geological Society, London, Special Publications, **61**, 263–287.

Duffaut, K. and M. Landrø, 2007, V_p/V_s ratio versus differential stress and rock consolidation—A comparison between rock models and time-lapse AVO data: Geophysics, **72**, no. 5, C81–C94.

Duffaut, K., M. Landrø, and R. Sollie, 2010, Using Mindlin theory to model friction dependent shear modulus in granular media: Geophysics, **75**, no. 3, E143–E152.

Holt, R., O-M. Nes, and E. Fjær, 2005, In-situ stress dependence of wave velocities in reservoir and overburden rocks The Leading Edge, **24**, 1268–1274.

Corresponding author: kdu@statoil.com